TRANSITION METAL DOPING OF SEMICONDUCTOR QUANTUM DOTS FOR ENHANCED HOT ELECTRON GENERATION UNDER VISIBLE EXCITATION

A Dissertation

by

DAVID G. PAROBEK

Submitted to the Office of Graduate and Professional Studies of
Texas A&M University
in partial fulfillment of the requirements for the degree of

DOCTOR OF PHILOSOPHY

Chair Committee: Dong Hee Son
Committee Members: James D. Batteas
Matthew Sheldon
Jamie Grunlan
Head of Department: Simon W. North

August 2020

Major Subject: Chemistry

ABSTRACT

Hot charge carrier generation and extraction from semiconducting and metal nanoparticle materials have been heavily researched from their potential to preform chemistry that regular electrons are not capable of. One major hurdle that inhibits the practical use of hot electrons is the need for high energy photons or high photon fluxes for their generation in most semiconductors, which is not readily available through solar radiation. Noble metal nanoparticles are able to generate hot electrons under visible radiation but due to the low relative energy of the hot electrons their use for jumping over energetic barriers and photocatalysis is limited.

Colloidal semiconductor nanocrystals have been at the forefront of nanoscience research from the wide range of interesting properties that are imparted on them from quantum confinement effects that result in new physical processes when compared to their bulk counterparts. The promising optical properties of these materials with high quantum yields and photostability has made them useful in biological, photovoltaic, photocatalytic, and optoelectronic applications. In 3-dimensional confined quantum dots, the excitonic wavefunction can extend throughout the volume of the structure yielding greater sensitivity to the addition of dopants, further increasing the ability to manipulate the optical properties.

Doping Mn in II-VI quantum dots has been of interest from the many optical and magnetic properties that it imparts on the host structure. The $^4T_1 - {}^6A_1$ transition has a low probability to occur from its small cross section due to its spin forbidden nature, relying on energy transfer from the host structure. The forbidden nature of this transition results in long millisecond photoluminescence lifetimes. The long lifetime of the Mn excited state is able to facilitate hot electron generation under low intensity *cw* excitation via two photon upconversion. This process occurs as follows: the first photon creates an exciton that has energy transfer to the Mn followed

by another exciton being formed which the Mn undergoes back energy transfer excited state electron 2 eV further into the conduction band. The hot electrons generated in this have the ability to outcompete regular electrons in photocatalysis, the ability to be photoemitted from the quantum dot, and pass through an insulating barrier. While these results show the capability of hot electrons, the hot electron generation efficiency is still low which creates the need to explore new material systems that have higher inherent quantum yields to better facilitate this process.

To circumvent this issue, cesium lead halide perovskite nanocrystals, which have photoluminescence quantum yields near unity, were explored as new material system for hot electron generation. The synthetic background for Mn doping in $CsPbCl_3$ and $CsPbBr_3$ was developed which will allow for the verification and study of the hot electron generation for this material. A new photoinduced anion exchange method was also developed which can allow for greater tunability of the perovskite optical properties. To further push the boundaries and capabilities of hot electrons, the photocatalytic reduction of CO_2 was studied using a hybrid quantum dot/metal catalyst system that showed the long-range electron transfer to the catalyst from the quantum dot via hot electrons.

ACKNOWLEDGMENTS

I would like to thank my research advisor, Dr. Son, for allowing me to join his group and do research in his lab. His excitement for science and research are the reasons why I wanted to join his group and I am happy that I did. I learned a great deal about how to be a scientist and the importance of doing careful work while always double-checking results. I enjoyed being able to walk in your office to discuss results and brainstorm ideas. I also appreciate that you would push me to work hard and accomplish things that I did not think were possible. If it were not for that then I do not think I would be the scientist that I am now.

I would also like to thank my undergraduate advisor Tara Meyer for giving me the advice to go to graduate school and also telling me to suck it up when I thought my undergraduate courses were hard. It helped to push me to work harder so I could succeed. I would like to thank my undergraduate research advisor Haitao Liu for letting me do research in his lab and giving me the opportunity to be a part of a lot of research projects. This truly gave me a strong foundation in research and I think it greatly contributed to the scientist I am today so I will always be grateful. I would like to thank Michelle Ward for providing me with the opportunities to work as an undergraduate TA and for giving me the chance to design labs. I would also like to thank Jill Millstone for giving me advice about graduate schools and always being willing to answer all the questions I had about what to do after graduation. I was fortunate to be surrounded by so many people that were willing to support me and provide me with a great environment to learn.

I would like to especially thank my mentor Yitong Dong for being patient and teaching me a great deal. We spent many days working late, but it was always enjoyable since we were usually bsing the whole time. If it was not for all your help, then I would not have been able to accomplish a lot of what I did. I would also like to thank Daniel Rossi for always being a good sport about

when I would make jokes about him being from Philadelphia. It was enjoyable to have someone to go back and forth with. You and Yitong were good role models for setting the standard for our group which pushed me to work harder. I would like to thank my group members Oscar, Tian, Doyun, Joe, and Xueting for always providing an open helpful environment as well as putting up with my grumpiness. I also appreciate Eric and Connor for being patient with me while I have been teaching them. They are hard workers and I have no doubt they will be able to keep pushing the hot electron research forward. I was fortunate to be part of a tight knit group.

I also wanted to thank the staff of the chemistry department. Sandy I am grateful for you always being available and around to fix all the problems that happen. I want to thank Jennifer Belcik for ordering all of our chemicals and equipment and dealing with the vendors when something was not right. I would also like to thank Timothy Pehl for fixing our equipment and giving answering all my questions about electrical stuff. I would like to thank Will Seward for teaching me about machining and for taking all my half baked blueprints and turning them into masterpieces. I wanted to thank Bill Merka for helping design and making the glassware for my projects. It makes research a lot easier when working with experts and I appreciate all of your help.

Lastly, I would like to thank my family and friends. Graduate school was difficult but having close friends makes it easier to get through tough times. I especially want to thank my mom and dad for giving me the chance to go to college and graduate school. You have made me the person I am today and if it was not for your support through every step then I do not think I would have made it this far.

CONTRIBUTORS AND FUNDING SOURCES

Contributors

This work was supported by the dissertation committee consisting of Professor Dong Hee Son, Professor James D. Batteas and Professor Matthew Sheldon of the Department of Chemistry and Professor Jamie Grunlan of the Department of Materials Science and Engineering.

The SEM/EDX measurements were conducted by Dr. Winson Kuo of the materials characterization facility at TAMU. The XRD measurements were made by Dr. Nattamai Bhuvanesh from the Department of Chemistry. The single particle measurement in Chapter III was conducted by Ho Jin of the Department of Chemistry.

All other work conducted on the dissertation was completed by the student independently.

Funding Sources

This work was made possible from NSF GRFP (DGE-1252521), NSF (CBET-1264840, CBET-1804412), IBS-R025-D1, and the Robert A. Welch Foundation (A-1639, A-1886, A-1880)

Its contents are solely the responsibility of the authors and do not necessarily represent the official views of the NSF and Robert A. Welch Foundation.

NOMENCLATURE

ODE	1-Octadecene
OAm	Oleylamine
OA	Oleic acid
ITO	Indium tin oxide
MPA	3-Mercaptopropionic acid
XRD	X-ray diffraction
TEM	Transmission electron microscopy
EDS	Energy dispersive X-ray spectroscopy
cw	continuous wave
ICP-MS	Inductively coupled plasma mass spectroscopy
QD	Quantum Dot
NC	Nanocrystal
SEM	Scanning electron microscope
EPR	Electron paramagnetic resonance
MNP	Metal nanoparticle
SCE	Saturated calomel electrode
$CsPbX_3$	Cesium lead halide
PLQY	Photoluminescence quantum yield

TABLE OF CONTENTS

Page

LIST OF FIGURES

LIST OF TABLES

LIST OF SCHEMES

CHAPTER I

INTRODUCTION

Hot electron generation has been widely studied in MNP and semiconductor systems as the excess energy in hot electrons can drive catalysis and photovoltaics that normal electrons cannot. A limiting factor in the design of semiconductor solar cells is that the excess energy from electrons excited with energy above the materials bandgap is converted into heat before the electrons are extracted. If this excess energy could be utilized before the electrons relaxed, then the power conversion efficiency in a single junction solar cell could increase from 33% to 66%.[1] This has led to many ultrafast optical studies to identify hot electron relaxation pathways to develop efficient extraction methods.[2-4] For photocatalytic applications, a hurdle for using hot electrons from semiconductor QDs is that either high intensity or high energy light is required, which is not readily available via solar radiation. To circumvent this problem, plasmonic MNP/semiconductor heterostructures were designed, capable of generating hot electrons without intense light sources. These hot electrons generated are able to overcome barriers that normal electrons would not be able to, which was shown in TiO_2/Au heterostructures and gold tipped CdS nanorods.[5, 6] The hot electrons are also able to promote photocatalytic reactions that could not typically occur under normal conditions. In gold MNPs, H_2 dissociation on its surface can occur from the hot electron transfer to the antibonding state of the H_2.[7] These systems are limited though by the fermi level position of the MNP being ~ 4 eV below vacuum with their hot electrons only having excess energy of 100 meV. This limits the use of the hot electrons generated with MNP since they would still lack the energy to reduce chemically expensive species.

Transition metal doped semiconductor QDs have shown themselves as a promising material that can generate hot electrons under low intensity *cw* visible excitation. Mn doping in II-

VI QDs results in energy transfer from the exciton of the host to the Mn dopant putting it in an excited state. Due to the spin forbidden nature of this transition, the lifetime of the Mn in its excited state can last for several milliseconds. This allows for another exciton to form in the host creating the chance for back energy transfer from the Mn excited state to the conduction band electron, resulting in a hot electron. The conduction band of CdS QDs is located 3 eV below the vacuum level, placing the location of the hot electrons generated around 1 eV with a small distribution possibly being above the vacuum level. In multiple experiments it was shown that Mn-doped QDs were able to outperform undoped QDs under similar reaction conditions. An example of this is when Mn-doped CdSSe/ZnS QDs catalytic ability were compared to their undoped counterpart under photoexcitation. Even though the hot electron generation process requires double the number of photons for their generation, the increase in available energy offset this with the doped QDs having a much higher efficiency of H_2 generation. The doped QDs were also capable of penetrating a 7 nm insulating barrier as well as being emitted from the QD under vacuum. This shows some of the capabilities that hot electrons have and further demonstrates their potential applicability in chemical reaction that require a large reduction potential.

While the past experiments have shown the capability of hot electrons, the efficiency of generating them is still low (< 1%). Two possible ways to improve this efficiency would be to add another dopant into the system to enhance the probability of back energy transfer or to explore new host systems for Mn doping. All inorganic $CsPbX_3$ perovskite NCs have become a popular new type of NC from their easy synthesis and their inherently high PLQYs (> 80%). Their labile crystal structure allows for the ability to tune the bandgap of the host throughout the visible spectrum by exchanging the halide ion. It is even possible to perform cation exchange to switch

out the A site or B site cation. These possibilities provide a new system that can easily be modified while still having optical properties that rival that of the II-VI QD system.

While the exploration of new platforms for hot electron generation materials is crucial, it is necessary to still explore proof of concept reactions to learn the capabilities of hot electrons. The direct reduction of CO_2 is ~1.5 V vs NHE greater than the reduction potential of H^+ which makes this process highly improbable to occur from a semiconductor without the aid of a cocatalyst. The use of a molecular catalyst coupled with a QD photosensitizer has shown to greatly enhance selectivity and reduction capabilities. The molecular catalyst must be linked to the QD to have efficient electron transfer which increases the complexity of the system since the ligand must be tailored specifically. From the high energy of hot electrons, it could be possible to directly reduce CO_2 to CO as well as being capable of having long range electron transfer to a metal catalyst, removing the need for a linker molecule.

This dissertation is organized as follows. Chapter III will introduce Mn doping in $CsPbCl_3$ perovskite and highlight the synthesis and structural characterization of the doped NC. This synthetic method is the starting point for doping Mn in $CsPbX_3$ perovskite NCs. In Chapter IV a variation of the synthesis in Chapter III is presented to dope Mn in $CsPbBr_3$ NCs. It was initially thought Mn could not be doped into $CsPbBr_3$ but through first creating a monolayer intermediate species coordinated with Mn we were able to synthesize Mn doped $CsPbBr_3$ nanocubes and nanoplatelets. In Chapter V photoinduced anion exchange of the $CsPbX_3$ is described as a new method to exchange the halide in the NC by using a halogenated solvent and photoexcitation. This method provides fine control since the reaction only occurs under photoexcitation. In Chapter VI, the use of the Mn doped QDs for the photocatalytic reduction of CO_2 to CO is displayed as an application of the Mn doped QD. In the experiment the QD is also paired with a metal catalyst to

determine if this will increase the efficiency of the system for generating CO. The dissertation will conclude with Chapter VII summarizing the experiments as well as discussing some of the next steps for future works with the perovskite and II-VI QD.

CHAPTER II

BACKGROUND AND LITERATURE OVERVIEW

2.1 Hot Electrons in Semiconductors and Noble Metals

Hot electrons in semiconductors and noble metal nanoparticles have been studied heavily over the past few decades from the potential benefits they have over band edge electrons in photovoltaic and photocatalytic applications. In semiconductor materials, one of the main goals has been to extend the hot electron lifetime long enough to harvest it before relaxation. It was theoretically predicted that if hot electrons, generated from photons with more energy than the band gap, could be captured before they lose their energy through phonon modes then the efficiency of a solar cell could be increased from 33% to 66%.[1] This remains a challenge still today due to the fast cooling process that is typically only 100s of femtoseconds.

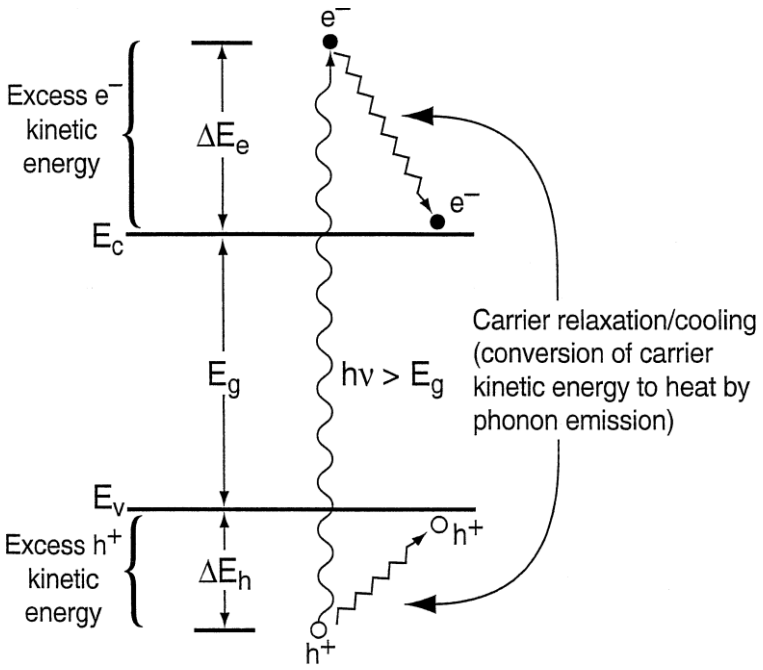

Figure 1. Representation of hot carrier cooling in a semiconductor. E_v is the valence band, E_c is the conduction band, E_g is the band gap, hν is photon energy, ΔE_e is the excess electron kinetic energy, and ΔE_h is the excess hole kinetic energy. Reprinted with permission from Nozik, A. J. *Annu. Rev. Phys. Chem.* **2001**. *52*, 193–231. Copyright 2001 Annual Reviews.

Figure 1 gives a schematic representation of the hot carrier generation and cooling process. Initially a photon (hν) with energy greater than E_g is absorbed which creates an electron and hole population that have excess kinetic energy. These populations reach thermal equilibrium through carrier-carrier scattering which leaves them with a thermal distribution with a temperature greater than that of the lattice. The hot carrier populations then equilibrate with the lattice temperature through the loss of their energy to the longitudinal optical phonons.[8] The relaxation of the hot carrier populations will depend on the quantity generated as well as the available phonons in the lattice. The hole population will relax faster than the electron population due to its larger effective mass as well as the greater density of states in the valence band. It was originally hypothesized that a "phonon bottleneck" could occur in confined materials from the larger spacing between the quantized energy levels where phonons have insufficient energy to bridge the gap.

While the "phonon bottleneck" was predicted for quantum confined structures it was never actually observed due to additional cooling pathways created from the coupling of the electron and hole. The relaxation of the hot electron in a CdSe QD was observed to be 300 fs with the potential pathways being through electron-electron or electron-hole Auger relaxation.[3, 9] A way to work around this was created by synthesizing CdSe/ZnS/ZnSe/CdSe QD with different shells that were capable of decoupling the electron and hole with hot electron lifetimes of 1 ns.[4] The effective coupling of the QD with an electron acceptor can also facilitate the extraction of the hot electrons which was shown with a PbS-TiO_2 heterostructure having 50 fs electron transfer times.[10] Perovskite nanocrystals have shown great promise for long lived hot electron lifetimes (100s of ps) from the large polarons that form under excitation due to the rotations of the A site cation in the lattice.[11] These results show the progress made for the ability to extract hot electrons from

semiconductor materials and the potential they can have to boost photovoltaic and photocatalytic applications.

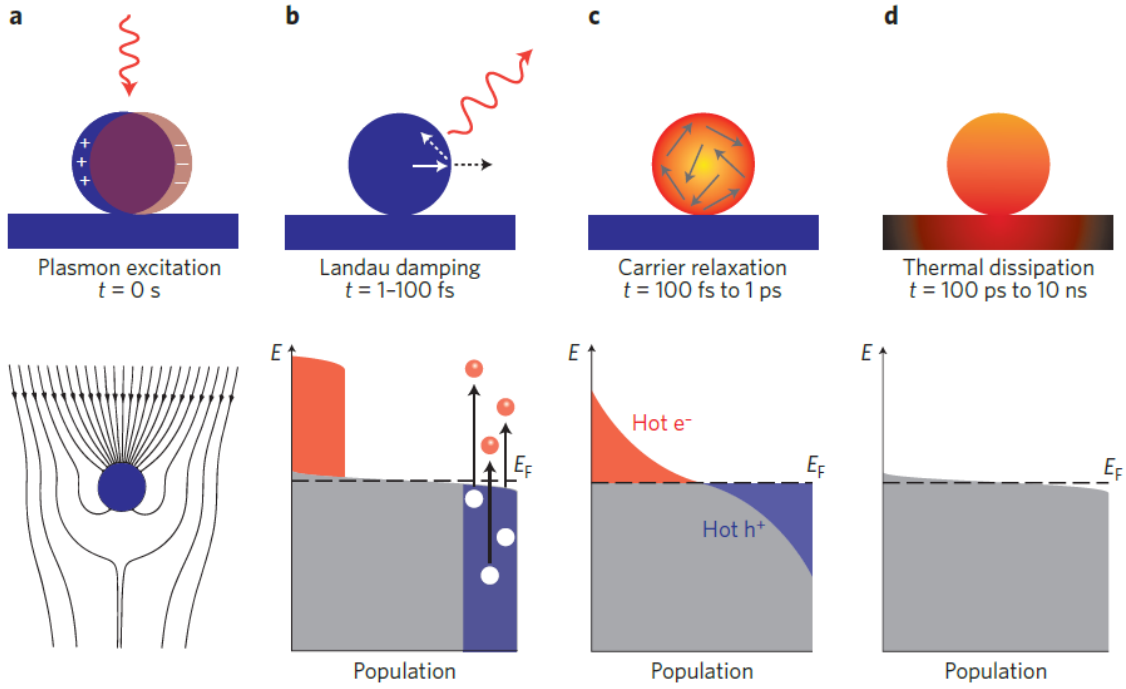

Figure 2. Hot electron generation process in MNP. (a) Photoexcitation of the localized plasmonic mode of the MNP (b) The absorbed light can either be emitted as a photon or transferred into an electron and hole pair through a process known as Landau damping. (c) The initial hot carrier population undergoes carrier-carrier scattering that results in the hot Fermi-Dirac distribution. (d) The carriers undergo thermal dissipation through the lattice and with the surrounding area generating heat. Reprinted with permission from Brongersma, M. L.; et al. *Nat. Nanotech.* **2015,** *10*, 25. Copyright 2015 Springer Nature.

While the generation of hot electrons are promising it can be limited by the energy requirements necessary for their generation since it can require either pulsed laser excitation or high energy UV photons. This limitation in semiconductors is not seen in MNP which can generate hot electrons with visible light excitation. The hot electron generation process in MNP has some slight differences compared to the semiconductor case (Figure 2). Upon excitation the plasmon can be quenched either by emitting a photon or through Landau Damping which results in the

creation of an electron-hole pair on the order of 1 to 100 fs. Then the electron-hole pair will redistribute their energy through carrier-carrier scattering creating a Fermi-Dirac distribution in about 100 fs to 1 ps. The electrons will interact with phonon modes and equilibrate with the lattice which can be described by a Two Temperature Model accounting for the electron temperature and lattice temperature. The final step is for the heat transfer to the surrounding area which occurs from 100 ps to 10 ns.[12] The hot electron generation in MNP has found its uses in photocatalytic H_2 splitting,[13] cancer treatments from photothermalization,[14] and electron transfer over high energetic barriers into semiconductors.[6]

2.2.1 $CsPbX_3$ Perovskite Nanocrystals

$CsPbX_3$ perovskite NCs have been at the forefront of colloidal semiconductor nanocrystal research since their inception in 2015.[15] They have gathered a large amount of attention due to their superb optical properties with PLQY greater than 90% after synthesis and some reports of unity PLQY with post synthesis modification.[16] They also exhibit very labile structures which allow for anion[17, 18] and cation exchange,[19] creating new optical properties in the host NC. There have also been multiple reports with methods to create anisotropic structures of the perovskite NCs being either 1D[20] and 2D[21, 22] confined as well as a reported method for 0D confined QD.[23] The fast development of optimized synthetic methods for the perovskite NCs has led to many photophysical studies to determine the properties of this new material for their eventual use in photovoltaic or optoelectronic applications.

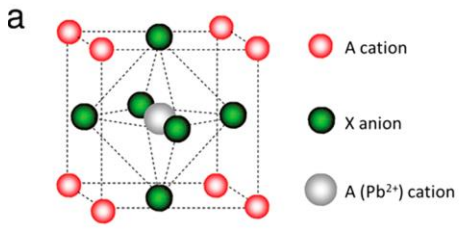

Figure 3. Representation of the crystal structure of perovskite. Reprinted with permission from Jena, A. K.; et al. *Chem. Rev.*, **2019,** *119*, 3036-3103. Copyright 2019 American Chemical Society.

The term perovskite was typically used to describe metal oxide materials that have uses in ferroelectrics or piezoelectric applications. It describes the position of the constituent ABX_3 atoms in the unit cell. The A^+ cation is located at the cube corner where the B^{2+} cation is at the body center and the X^- is at the face center. This forms the octahedral shell of anions around the B site cation with the A site cation located in the voids (Figure 3).[24] The crystal structure of the perovskite can be predicted based on the radius of the constituent atoms by calculating the Goldschmidt tolerance factor which should be between 0.8 and 1 for a 3-D cubic structure.[25] There were very few example of semiconducting perovskite materials until metal halides started to find their use in solar cell applications.

One of the first successful displays of a perovskite in solar applications was using a methylammonium lead iodide/chloride ($CH_3NH_3PbI_{3-x}Cl_x$) thin film with efficiencies at 10.9% back in 2012.[26] This number has risen to over 23% recently which is why there has been such a push and increase in activity involving research with halide perovskites.[27] These high efficiencies arise from the large carrier mobilities in the perovskite and due to the band structure of the material hinders recombination from defect states. A large hurdle to overcome though with this material is the instability it has towards water and polar solvents which can result in the dissolution of the crystal structure. This has led to the inclusion of mixed cation and anion structures within the perovskite[24] and to the eventual synthesis of the $CsPbX_3$ perovskite NCs.

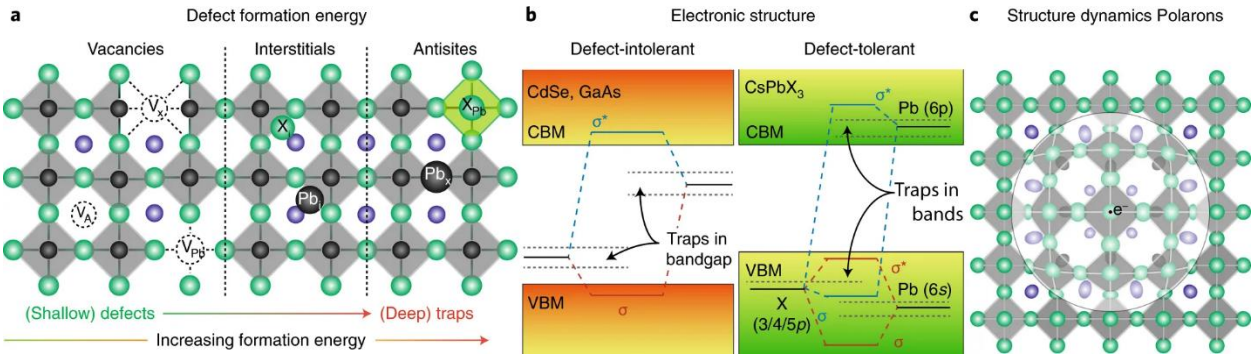

Figure 4. (a) Representation of increasing formation energy for varying defects in the perovskite lattice. (b) Example of differences in midgap states for covalent defect intolerant (left) and ionic defect tolerant (right) nanocrystals. (c) Illustration of formation of polaron formation in the perovskite nanocrystals for screening defects. Reprinted with permission from Quinten A. A.; et al, *Nat. Mater.* **2018** *17*, 394–405. Copyright 2018 Springer Nature.

The larger formation energy of the $CsPbX_3$ NCs allows for the greater stability compared to the $CH_3NH_3PbX_3$ NCs which has allowed for the study of their optical properties for potential use in photovoltaic applications. The high inherent PLQY exhibited by $CsPbX_3$ perovskite NCs gives them great promise and sets them apart from II-VI QDs which have very low PLQY without surface treatment. The origin of the high PLQY in the perovskite NCs comes from their unique band structure and the high formation energy of defects (Figure 4). The band structure of the perovskite is unique from its lack of interaction between the bonding and antibonding orbitals. The valence band consists of the Pb *s* and Br *p* orbitals while the conduction band is made up of the Pb *p* orbitals.[28] The *p* orbitals of the Br are below the valence band maximum from the strong *s-p* interaction between the Pb and Br while the empty Pb *p* orbitals are located above the conduction band minimum. Br and Cs type vacancies have the lowest defect formation energy, compared to interstitial or antisite defects, making them the predominate defect. Defects associated with vacancies are typically shallow traps which do cause nonradiative carrier trapping. From the location of the Br orbitals in the valence band this results in the lack of midgap trap states. This

can account for the inherently high PLQY but there are still contributions from defects that result in less than unity PLQY which has resulted in post synthesis modification to achieve these values.

There have been many reports of synthetic methods or post synthesis modifications that can yield near unity PLQY for $CsPbX_3$ perovskite NCs. One of the first successful methods was developed by Koscher et al. who utilized sodium thiocyanate to remove undercoordinated Pb that was on the surface of the NC. This method worked for both fresh and aged NC samples achieving unity PLQY and monoexponential lifetimes in both cases but was limited to $CsPbBr_3$.[16] Liu et al. developed a synthetic method using TOP-PbI_2 to generate $CsPbI_3$ that exhibited enhanced stability and unity PLQY.[29] Another method developed by Dutta et al. was able to create unity PLQY for Cl, Br and I containing halide perovskite by using an equimolar amount of Pb and Cs precursor and injecting oleylammonium halide salt at temperatures greater than 200 °C.[30] These are just a few examples of methodologies that are able to produce $CsPbX_3$ perovskite NCs with PLQYs approaching unity, enhancing their use in photovoltaic applications.

The structural tunability of the perovskite, allowing for the easy replacement of its halide anions, is another interesting feature of this material since it allows for a post synthesis method to vary its PL wavelength across the visible spectrum. This has led to many studies developing methods and trying to understand the mechanism of this process. The first anion exchange methods were developed not long after the initial perovskite synthesis was published. They involved using oleylammonium halide precursors among other halide containing salts to exchange between Cl, Br, and I.[17, 18] The study of the mechanism for this process was done by Koscher et al. who used a microfluidic setup to monitor the PL of the exchange of $CsPbX_3$ NCs. They described two different mechanism of exchange for Cl to Br and Br to I. In the first case with the smaller Cl anions they claimed the exchange was diffusion limited resulting in clusters of Cl forming in the lattice as the

exchange occurred while from Br to I it is surface limited resulting in a homogeneous exchange.[31] Zhang et al. just recently published a work monitoring the exchange of $CsPbBr_3$ nanoplatelets via optical microscopy allowing them to map different areas. Their results showed that there is an initial surface reaction that is followed by solid state diffusion limiting the speed of the process.[32] From the difficulties of making quantum confined NCs this was the only method that allowed for the tunability of the PL across the visible spectrum.

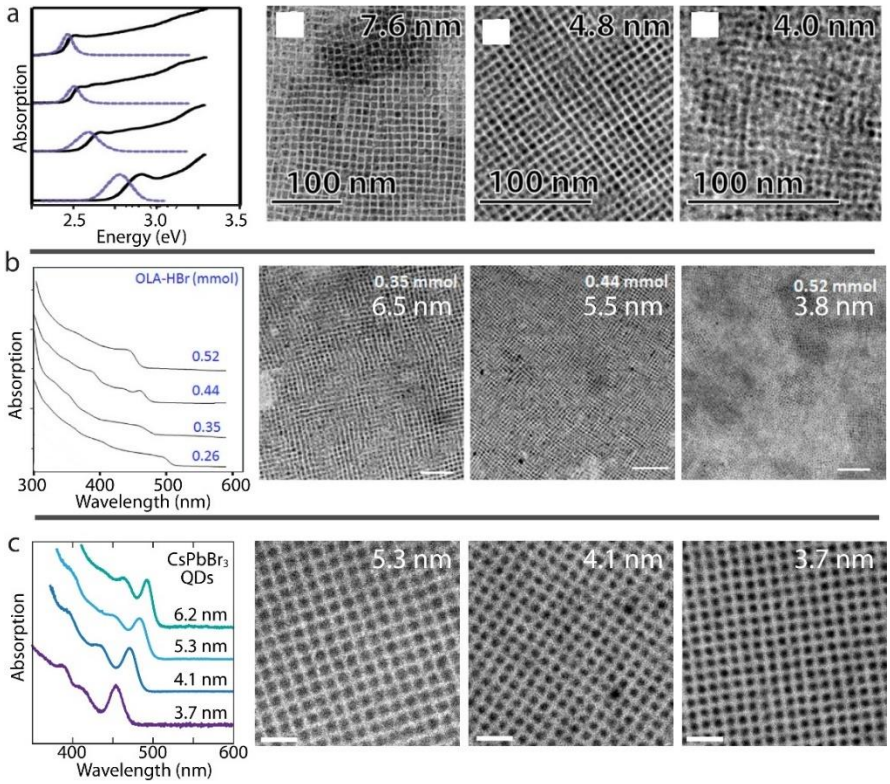

Figure 5. Absorption and TEM of $CsPbBr_3$ NCs made by (a) varying the ratio of oleic acid and oleylamine. Reprinted with permission from Almeida, G.; et al. *ACS Nano* **2018**, *12*, 2, 1704-1711. Copyright 2018 American Chemical Society (b) varying the amount of oleylammonium bromide salt. Reprinted with permission from Dutta, A.; et al. *ACS Energy Lett.* **2018**, *3*, 2, 329-334 Copyright 2018 American Chemical Society (c) controlling the size via thermodynamic equilibrium. Reprinted with permission from Dong, Y.; et al. *Nano Lett.* **2018,** *18*, 6, 3716-3722 Copyright 2018 American Chemical Society.

The synthesis of highly monodisperse quantum confined samples of the perovskite was a difficult challenge from the fast nature of the reaction once the cesium was injected. This resulted in groups using lower reaction temperatures to obtain smaller sizes, but the sample distribution was not homogeneous.[33] Others had attempted to change the ratio of ligands in the reaction system claiming this will reduce the amount of ripening which causes the large size distribution (Figure 5).[34, 35] It was not until a different approach was taken which did not focus on the kinetics of the reaction but altered the thermodynamic equilibrium in the system. Dong et al. was able to achieve highly monodisperse and quantum confined $CsPbX_3$ QDs by providing an excess of halide in the system which would result in the smaller size of the nanocrystal formed (Figure 5).[23] The capability for synthesizing optically pure and quantum confined $CsPbX_3$ opens the door to discover the unique photophysical properties of these materials.

2.2.2 Review of Mn-doping in $CsPbX_3$ Perovskite Nanocrystals*

Manipulating the electronic structure of semiconducting materials through the inclusion of dopant ions is a valuable field of study from the new properties imparted on the material[36-40]. Modern day electronics heavily rely on the development of either p- or n- type doped semiconductors from their uses in diodes and transistors. From the advent of semiconductor nanocrystals in the early 90's it did not take long before doping methods were developed to study the effects of impurities on the host structure in a quantum confined system. Mn doping in II-VI quantum dots has been under development since the 90's and since then has had many decades for

* Reprinted with permission from Dong, Yitong.; Parobek, David.; Son, Dong Hee. Review: Controlling Quantum Confinement and Magnetic Doping of Cesium Lead Halide Perovskite Nanocrystals" *J. Kor. Cer. Soc.*, **2018**. *55(6), 515-516.* Copyright 2018 Korean Ceramic Society.

the synthetic methods to be well understood and used as a model system for doping other families of semiconductor nanocrystals[41-47].

Mn doped semiconductor nanocrystal display unique optical and magnetic properties, typically replacing an atom with the same charge causing it to isovalently dope the host structure. Mn doped nanocrystals usually display a broad photoluminescence peak around 2 eV which is sensitized by the host structure via energy transfer[48]. The characteristic orange Mn emission originates from the spin forbidden $^4T_1$ to $^6A_1$ d-d transition resulting in its long lifetime ranging from μs to ms time scales. The d5 nature of the Mn also gives it interesting magnetic properties making it possible to synthesize dilute magnetic semiconductors exhibiting giant Zeeman splitting[49].

All inorganic $CsPbX_3$ perovskite have made their way to the forefront of colloidal semiconductors with their superb optical properties resulting in an explosion of research as a promising new optoelectronic material. The host perovskite structure displays high quantum yields with a robust nature towards midgap trap states making them an ideal structure for incorporation of dopants to take advantage of these properties. Since the initial synthesis of the inorganic perovskite nanocrystals multiple reports have already shown the incorporation of many different impurity ions (Mn^{2+}, Bi^{3+}, Al^{3+}, Cd^{2+}, Zn^{2+}, $Au^{3+/1+}$, Ln^{3+}, Yb^{3+}) with varying properties to the host structure[19, 50-58]. This section will primarily focus on the synthesis of Mn doping $CsPbX_3$ perovskite with discussion on the different doping methods, the study of doping Mn in $CsPbBr_3$, as well as some of the applications of Mn doped NCs to improve the stability and capabilities of photovoltaics. There are earlier perspectives on doping Mn and other metals into the Pb B site providing an overview of some of the initial works that provide useful information.[59, 60]

The first successful synthesis of Mn doped perovskite was a hot injection method for $CsPbCl_3$ perovskite nanocrystals[50, 51]. The synthesis followed a similar protocol to what was developed by Kovalenko with the addition of $MnCl_2$ to the reaction mixture. The use of other Mn salts ($Mn(ac)_2$, $Mn(acac)_2$, and $Mn(oleate)_2$) had proven ineffective doping precursors where $MnCl_2$ already possessed coordination to the Cl anion helping its incorporation into the lattice[51]. The resulting product was Mn doped $CsPbCl_3$ nanocubes with minimal changes in the host structure (Figure 6a). The particles exhibited strong Mn PL at 600 nm while also showing enhanced exciton emission shown in figure 6b, which will be discussed later. From the monoexponential lifetime decay (Figure 6c) and the consistent PL peak position from single particle spectra it was believed that the Mn was homogeneously doped throughout the perovskite nanocube. A major difficulty in characterizing the doping concentration in the perovskite nanocrystals was the lack of an efficient cleaning method. Polar solvents result in the destruction of the nanocrystal so cleaning methods from II-VI system cannot be applied. This resulted in the use of a gel permeation chromatography (GPC) cleaning method developed by Shen *et al* to thoroughly clean the nanocrystal and show the decrease in Mn doping concentration with each successive run through the column[61]. The presence of contaminants even after running the sample through the column twice shows the difficulties and importance of properly cleaning the particle.

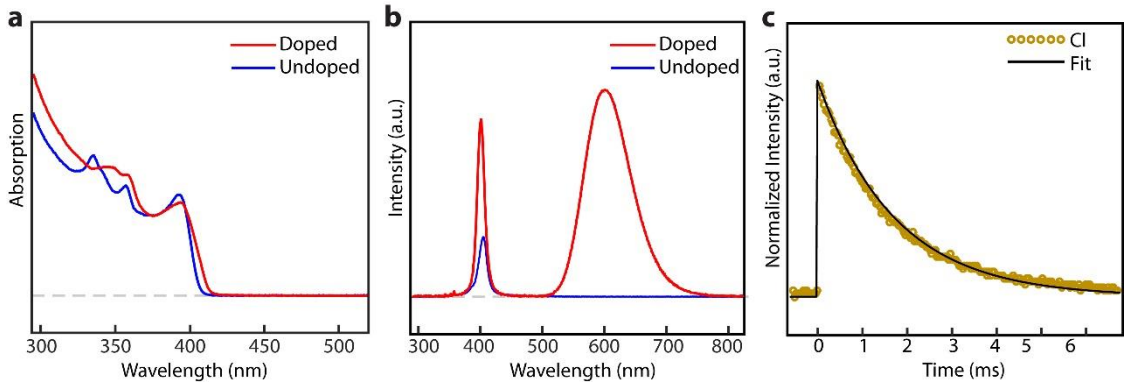

Figure 6. (a) and (b) Absorption and PL spectra of Mn doped $CsPbCl_3$ nanocrystals with their undoped control samples. (c) Time dependence PL decay of Mn phosphorescence. Reprinted with permission from Parobek, D.; et al. *Nano Lett.* 2016, 16, 12, 7376-7380. Copyright 2016 American Chemical Society.

The hot injection synthesis protocol has been further optimized and enhanced to increase the doping concentration of the Mn in the nanocrystal as well as enhance the efficiency of the dopant entering the structure. Liu *et al* systematically increased the amount of Mn precursor being used increasing the Pb:Mn ratio from 1:1.5 in previous reported literature the whole way to 1:10 obtaining particles that had 46% Mn content as well as reaching quantum yields up to 56% (Figure 7a,b)[62]. They also varied the temperature of the reaction from 170 °C to 210 °C showing that the Mn content increased with temperature. Adhikari *et al* took another approach to efficiently dope Mn into the particle by incorporating oleylammonium chloride into the reaction mixture showing the increasing Mn PL intensity with increasing amounts of oleylammonium chloride (Figure 7c-e)[63]. They found that for just 5% of Mn to Pb in the reaction mixture strong Mn emission with minimal exciton emission was obtained whereas without the oleylammonium chloride even at 100% of Mn to Pb there was still a considerable contribution of the exciton present with the Mn emission. They attribute the efficient Mn doping to the greater concentration of nanocrystals forming thus creating a higher probability for Mn to enter the lattice. This method greatly reduces

the amount of excess Mn precursor needed to use in the synthesis making the purification much simpler.

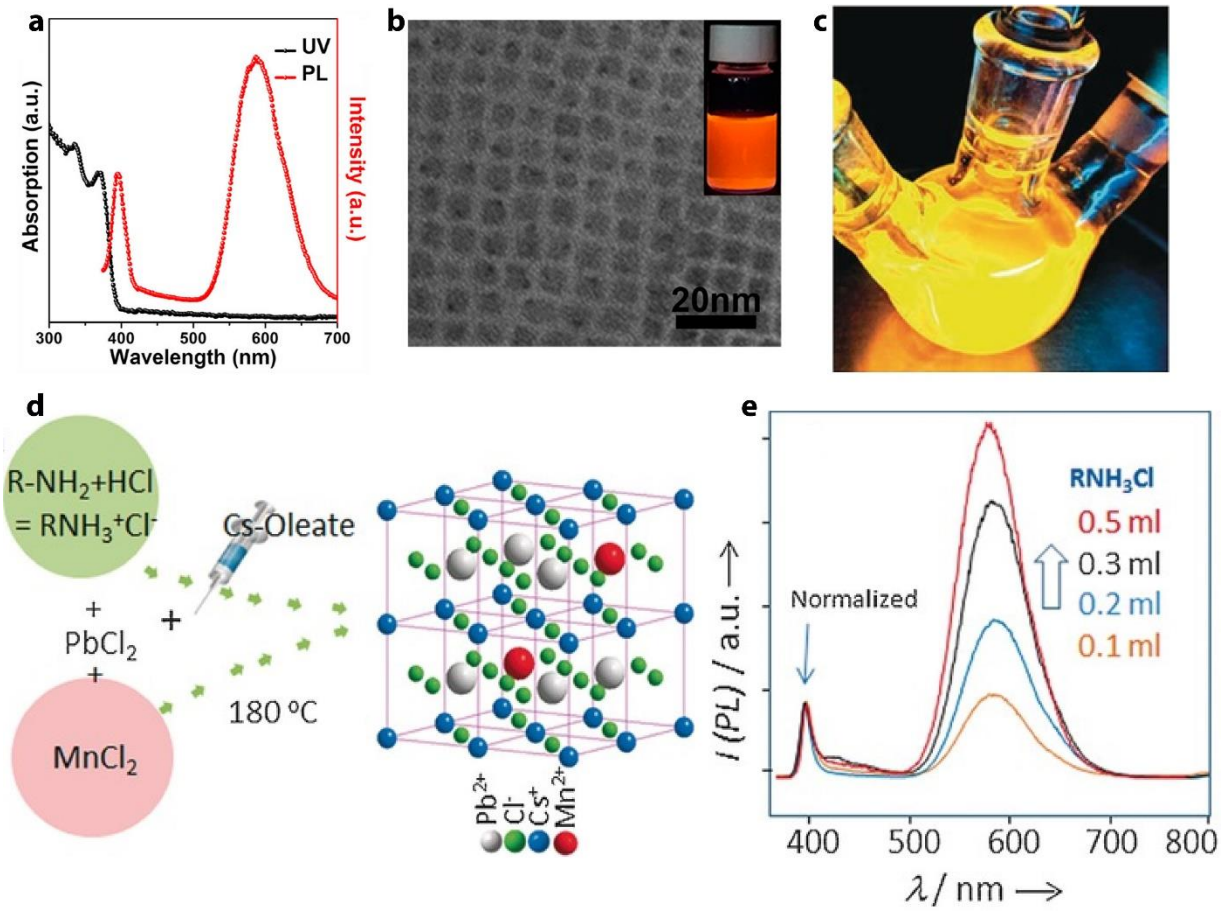

Figure 7. (a) Absorption and PL spectra of $CsPbCl_3$ sample with high Mn doping concentration (~ 46 %). (b) TEM images of $CsPbCl_3$ NCs with high Mn doping concentration. Reprinted with permission from Liu, H.; et al. *ACS Nano* **2017**, *11*, 2, 2239-2247. Copyright 2017 American Chemical Society (c) Photograph of Mn doped $CsPbCl_3$ NCs under UV excitation. (d) Method involving ammonium chloride mixture to dope Mn in $CsPbCl_3$ NCs. (e) the PL spectra of $CsPbCl_3$ NCs made with increasing amount of ammonium chloride mixture. Reprinted with permission from Das Adhikari, S.; et al. *Ang. Chem. Int. Ed.* **2017.** *56*, 30, 8746-8750. Copyright 2017 Wiley-VCH Verlag GmbH & Co. KGaA, Weinheim

The synthesis of the Mn doped $CsPbCl_3$ has not been limited to hot injection methods or the generation of nanocubes. Meijerink showed two different examples of room temperature methods for doping the nanocrystals with non-halide Mn precursors[64, 65]. In their first work they used metal

acetate salts which were converted to metal oleate complexes in the presence of ligands. Then upon the addition of HCl the carboxylate groups were protonated increasing the amount of monomer initiating the formation of the nanocubes. The acid also created a Cl^- rich surface supplying binding sites for the Mn. They later coated the particle with a $CsPbCl_3$ shell passivating the Mn ligand field resulting with an increase in the PLQY and Mn lifetime. In their other method they synthesized $CsPbCl_3$ nanocrystals with a Mn stearate precursor that resulted in the nanocubes being undoped but upon the addition of $SiCl_4$ the particles began to exhibit Mn emission. They reasoned that the $SiCl_4$ hydrolyzed into HCl in the presence of water displacing the Mn stearate leftover in the solution causing the doping of the nanocrystal while also having a silica shell around the particle. This not only provided an alternative pathway to dope the particles but also includes the formation of a silica shell that increased the stability of the nanocrystals.

There have also been several reports showing methods for synthesizing $CsPbCl_3$ nanoplatelets, providing the opportunity to study a Mn doped perovskite exhibiting quantum confinement. In the first work Mir *et al* used a room temperature antisolvent method to generate doped nanoplatelets of $CsPbCl_3$ having a thickness of 2.2 nm with a length of 32 nm and width of 9 nm[66]. They were also able to control the doping range from 0.2% to 2% displayed by the decrease in resolution of the EPR spectra from low concentration to high as well as the increasing of the Mn emission as the concentration increased. Adhikari *et al* provided another method of generating nanoplatelets through first synthesizing Mn doped monolayer $CsPbCl_3$ that could be converted to nanoplatelets upon the addition of Cs-oleate with heating of the solution[67]. They generated nanoplatelets with 5 nm of thickness and varying edge length from 120 nm to 20 nm depending on the amount of Cs and Mn in the reaction system. The nanoplatelet size was affected by the amount of Mn incorporated into the nanocrystal since, compared to Pb it is energetically less

favorable, suppressing the growth of the nanoplatelet. In only a short period of time there has been much progress in developing and understanding different ways to dope $CsPbCl_3$ nanocubes and nanoplatelets further pushing the opportunity of studying the properties of these materials and utilizing them in a wide range of photovoltaic and magneto-optical applications.

While many of the synthetic methods have focused on the development of Mn doped $CsPbCl_3$ NCs there have been few attempts to incorporate Mn into a $CsPbBr_3$ lattice. $CsPbBr_3$ would be the ideal host structure for Mn doping from its greater absorption cross section in the visible spectrum as well as its intrinsically higher PLQY. Liu *et al* hypothesized that the direct synthesis of $CsPbBr_3$ with $MnBr_2$ was energetically unfavorable from the large difference in bond energy between the Pb-Br (249 kJ/mol) and Mn-Br (314 kJ/mol) compared to Pb-Cl (301 kJ/mol) and Mn-Cl (338 kJ/mol)[50]. This results in the $MnBr_2$ being unable to dissociate into Mn^{2+} prohibiting its incorporated into the nanocrystal lattice. There were multiple works attempting anion exchange from $CsPbCl_3$ to $CsPbBr_3$ resulting in a large decrease in the Mn emission as more Br^- entered the structure[68]. Others attempted cation exchange with the Pb in $CsPbBr_3$ using $MnCl_2$ but this also resulted in anion exchange with Mn emission only appearing after Cl^- was the dominant anion present[69]. Zou *et al* showed that they had doped Mn into $CsPbBr_3$ and that it increased the stability of the particle but there was no Mn emission present[70]. Some explanations for the lack of Mn emission in Br containing perovskite is not due to the difficulty from synthesis but the back-energy transfer from the Mn to the exciton effectively quenching its PL, similar to what is seen in II-VI QDs[71, 72].

This theory was disputed by Gamelin and coworkers who developed a method to perform anion exchange of Mn doped $CsPbCl_3$ perovskite with TMS-Br as the precursor while retaining the Mn emission when it is exchanged to $CsPbBr_3$.[73] They note that the Mn emission is still present

even at high Br content but the EPR signal is gone (Figure 8a,b). From this result they suggest that due to the disappearance of the EPR signal but retention of the Mn emission the Mn ions are clustering in the structure as more Br is exchanged with Cl. This causes an exchange effect in the lattice between Mn which accounts for the lack of EPR signal. To argue against the theory of thermally assisted back energy transfer they conduct low temperature PL measurements that show the presence of excitonic emission even at room temperature. This is different from previous studies using Mn doped CdSe since at low temperatures the thermally assisted back energy transfer should not occur and instead unidirectional energy transfer to Mn should dominate.

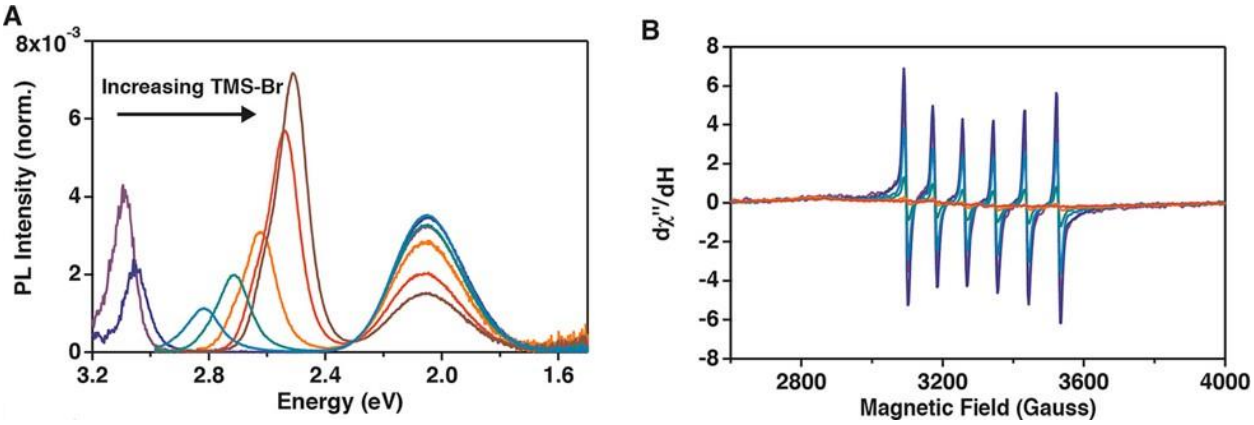

Figure 8. (a) PL spectra of Mn-doped $CsPbCl_3$ NCs in EPR tube during anion exchange. (b) X-band EPR spectra collected during the course of anion exchange. Reprinted with permission from De Siena, C. M.; et al. *Chem. Mater.* **2019**, *31*, 18, 7711-7722. Copyright 2019 American Chemical Society.

The first synthesis to successfully result in Mn doped $CsPbBr_3$ with Mn emission utilized a hot injection method with the addition of HBr[52]. The synthesis relied on the creation of the monolayer perovskite ($L_2[Pb_xMn_{1-x}Br_4]$) as an intermediate, which have been synthesized by others in a microcrystal to bulk size scale(references here), that acted as a way to coordinate Pb and Mn eventually leading to its inclusion in the nanocubes (Figure 9a). The Mn emission was directly correlated to the amount of HBr used in the synthesis correlating between the monolayer and nanocubes that were created. The monolayer species had an absorption maximum at 395 nm

with sensitized Mn emission at 620 nm with a 120 μs lifetime verified through photoluminescence excitation measurement. The monolayer species was also characterized by a series of small angle diffraction peaks appearing in the x-ray diffraction with equal spacing of 2.2° correlating to 4.1 nm spacing between stacked layers separated by the ligand. The synthesized nanocubes displayed Mn emission centered at 590 nm with PLQY ranging from 1 to 30% and lifetime decays from 24 μs to 271 μs with increasing amounts of HBr (Figure 9b-d). There was also a blueshift in the absorption spectra with the increasing amount of HBr. We believed the blueshift in the spectra was not from quantum confinement as the size of the particle did not change from 0 μL to 100 μL of HBr but instead from the increase in Mn entering the lattice. Previous works showed through cation exchange of Zn that the absorption spectra of the $CsPbBr_3$ blueshifted as more of the smaller metal cations entered the structure.[19] This was a result from the shortening of the Pb-Br bond length resulting in higher energy transition of the absorption spectra. As we increased the HBr to 200 μL we did observe the particle size decrease from 8.5 nm to 6.5 nm as a result from the increased amount Br^- in the system following a mechanism describe earlier. The synthesis was also able to produce nanoplatelets that could be separated from the nanocubes due to the inability to dissolve in hexanes from their large lateral dimensions.

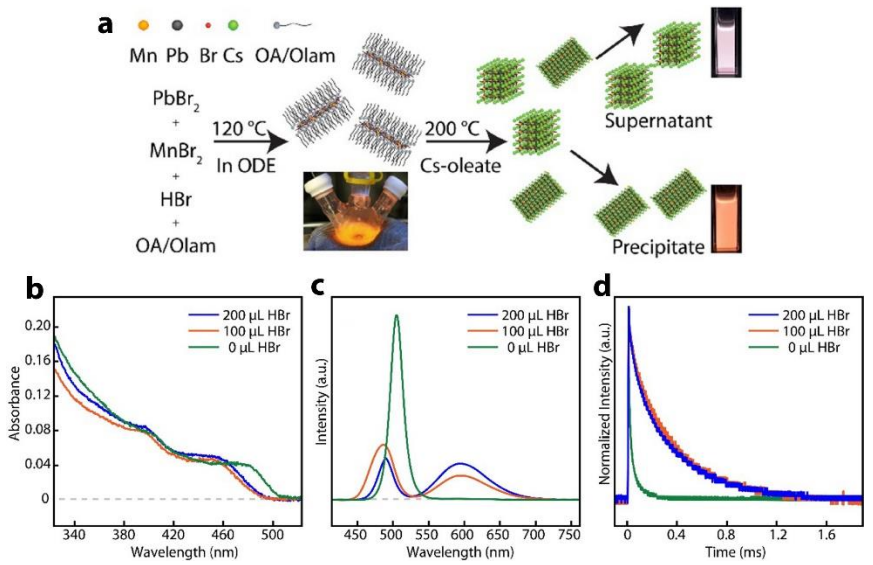

Figure 9. (a) Scheme of doping Mn into $CsPbBr_3$ NCs. (b) and (c) absorption and PL spectra of Mn doped $CsPbBr_3$ NCs made with different amount of HBr. (d) Time dependent PL intensity of Mn phosphorescence for sample made with different amount of HBr. Reprinted with permission from Parobek, D.; et al. *Chem. Mater.* **2018**, *30*, 9, 2939-2944. Copyright 2018 American Chemical Society.

Due to the lack of synthetic methods for doping $CsPbBr_3$ most of the spectroscopic as well as device fabrication was done on the Mn doped $CsPbCl_3$ system. From the presence of the exciton peak even after Mn doping it was crucial to determine the energy transfer rate in this system. It was hypothesized that since the particles were weakly confined and the exciton emission increased upon the addition of Mn that the energy transfer process was much slower than in the II-VI QD system. Through a transient absorption study done by Rossi *et al*, it was shown that the energy transfer rate was 380 ps which is about 2-5 times slower than the CdS/ZnS Mn doped QD (Figure 10a).[74] Considering the nanocrystals under study were not quantum confined, reducing the wavefunction overlap, this leaves room to develop synthetic methods to create confined systems that could potentially exhibit a fast energy transfer rate. This study also investigated the origin of the increasing exciton emission upon Mn doping by performing self-anion exchange on undoped nanocrystals passivating Cl vacancies increasing the PLQY. From the dynamics of the fast time

decay, attributed to electron trapping from surface defects, in the undoped phototreated sample there was an increase from 4.8 ps to 6.6 ps like the fast time decay between the undoped and Mn doped $CsPbCl_3$ nanocrystal. This helps confirm that the stability and raise in quantum yield could be occurring from the passivation of defects from the halide rich synthesis conditions.

The Mn doped $CsPbCl_3$ perovskite nanocrystal also displayed interesting behavior when cooled to low temperatures. Yuan *et al* showed that with decreasing temperature the Mn emission decreased while the exciton emission increased being attributed to the fast decay of the exciton which could compete with the slow energy transfer to the Mn[75]. It was also observed that the Mn PL decay time increased with the decreasing temperature, opposite to what is seen in II-VI systems. They predicted this occurred from the pseudo-octahedral symmetry of the Mn resulting in the transition being parity and spin forbidden. For allowed transitions to occur, they need to couple to symmetry breaking vibrations which activate at higher temperatures giving faster lifetimes as the temperature in the system increases (Figure 10b).

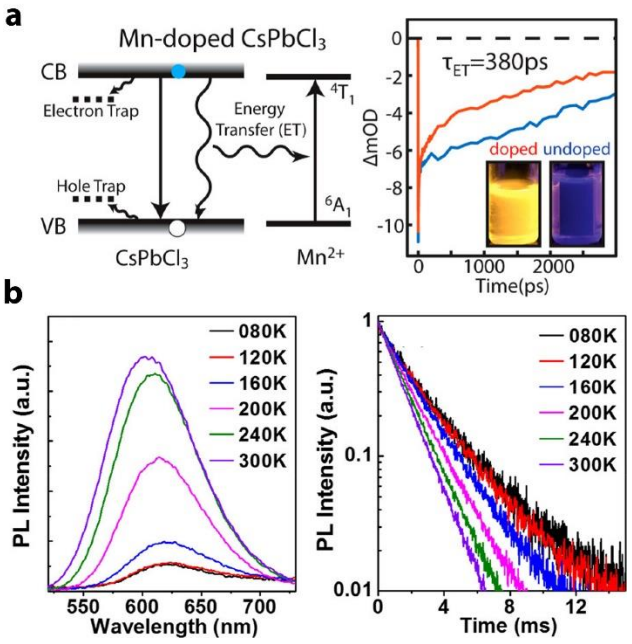

Figure 10. (a) Scheme of exciton-to-dopant energy transfer in Mn doped $CsPbCl_3$ NCs and Transient absorption data for doped and undoped $CsPbCl_3$ NCs. Reprinted with permission from

Rossi, D.; et al. *J. Phys. Chem. C* **2017,** *121*, 32, 17143-17149. Copyright 2017 American Chemical Society (b) Temperature dependent PL intensity of Mn doped $CsPbCl_3$ NCs. Reprinted with permission from Yuan, X.; et al. *Chem. Mater.* **2017**, *29*, 18, 8003-8011 Copyright 2017 American Chemical Society.

Mn doped $CsPbCl_3$ perovskite have also been used in multiple devices including solar concentrators or LEDs[70, 76-78]. Multiple works have used this to make a WLED with higher color temperatures arising from the intense Mn emission (Figure 11a)[79, 80]. The perovskite also has a large absorption cross section in the UV enabling it to act as a down converter, transferring the energy to Mn which can then reemit the light in a more visible region that a Si solar cell can absorb[77]. Two works showed a similar 3-5% increase in the power conversion efficiency and short circuit current when a layer of Mn doped $CsPbCl_3$ nanocrystals were placed on a Si solar cell (Figure 11b)[81]. The Mn doped $CsPbCl_3$ nanocrystals demonstrated sensing capabilities through detecting the amount of oxygen present in an environment based on the quenching of the Mn PL[82]. As shown in the II-VI QD systems the Mn doped perovskite nanocrystals could be potential candidates for hot electron generation pushing their capabilities for photocatalysis. Preliminary studies have already shown Mn doped $CsPbCl_3$ under low intensity visible light can generate a photocurrent from photoemitted hot electrons under vacuum.

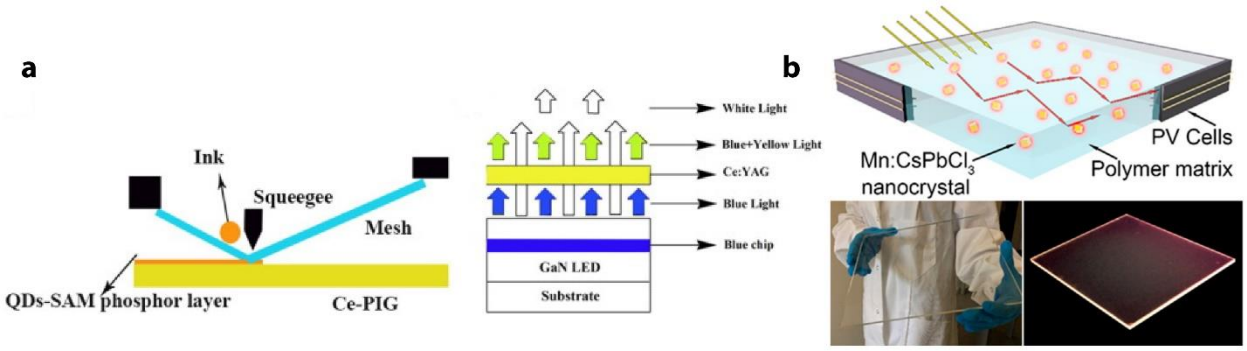

Figure 11. (a) Scheme of WLED made of Mn $CsPbCl_3$ NCs. Reprinted with permission from He, M.; et al. *App. Surf. Sci.* **2018**, *448*, 400-406. Copyright 2018 Elsevier B. V. (b) Solar concentrators made of Mn doped $CsPbCl_3$ NCs. Reprinted with permission from Meinardi, F.; et al. *ACS Energy Lett.* **2017,** *2,* 10, 2368-2377. Copyright 2017 American Chemical Society.

There has been a considerable amount of progress over the past few years for Mn doping as well as including other dopants into the perovskite structure. With this progress there are still discrepancies in the reported literature and further goals to achieve. A major issue when doping $CsPbX_3$ perovskite is completing proper cleaning procedures to receive accurate doping concentrations. If not done properly, this can lead to overestimations in the doping concentration leading to misguided conclusions about the properties of the doped nanocrystal. Another major hurdle is doping the Mn into a 0-dimensional QD structure to learn the full extent of the interaction between the exciton and dopant wavefunction. From further optimization and understanding of the synthesis of perovskite this is an obtainable goal to achieve.

2.3.1 Optical Properties of Mn doped II-VI QDs

When an electron-hole pair or exciton is created in a semiconductor QDs there are several possible relaxation pathways (Figure 12). There is fast electron (2) and hole traps (3) that will outcompete band edge luminescence (1), quenching it. The addition of dopants creates new photophysical pathways through charge or energy transfer (4) that are capable of outcompeting electron and hole trapping. The transition metal doping of Mn has been a heavily researched topic from the new optical and magnetic properties that it imparts on the host structure. Mn^{2+} is a d^5 high spin transition metal which results in its excitation from its ground state ($^6A_1$) to an excited state ($^4T_1$) to be a forbidden transition from the change in total spin. This results in its extinction coefficient to be several orders of magnitude lower than its host[83] causing the direct excitation of this transition to be highly improbable.

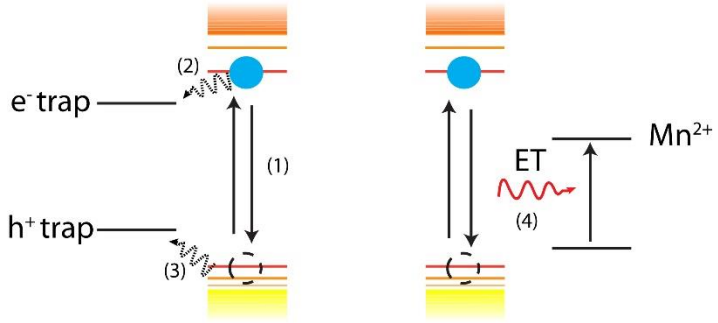

Figure 12. Potential relaxation pathways for exciton. (1) Radiative recombination of electron and hole, (2) electron trap, (3) hole trap, and (4) energy transfer to dopant impurity.

The excitation of Mn from its $^6A_1$ to $^4T_1$ state occurs via energy transfer from the host which is then followed by its long lived (μs to ms) phosphorescence ($^4T_1 \rightarrow {}^6A_1$) which is located around 600 nm. The peak position of the Mn phosphorescence is dependent on the ligand field splitting and is not affected greatly by the host structure[84] but it has been shown to redshift with increasing pressure from the distortions that occur in the crystal lattice.[85] The lifetime of the Mn excited state is dependent on the ligand field surrounding the Mn where ZnSe and ZnS show lifetimes of 100 μs and 1 ms respectively which a similar effect was seen in Br and Cl perovskite.[51, 52, 86] This is a result of the heavier anions resulting in greater spin orbit coupling which relaxes the forbidden nature of the transition. When the doping concentration is high the Mn dopants have a probability of being in clusters which will result in mixing of their *d* orbitals and also reduce the lifetime and QY of the Mn phosphorescence.[48]

In some host QD the Mn PLQY can reach near unity from the fast energy transfer rate of the exciton that can outcompete nonradiative relaxation that would typically result in a decrease of radiative relaxation. To determine the actual rate though there was some difficulty in determining this number accurately.[87] It can theoretically be calculated through the lifetime and Mn QY through the following equation (1).

$$QY_{Mn} = \frac{(\tau_{ET})^{-1}}{(\tau_{EX})^{-1}+(\tau_{ET})^{-1}} \quad (1)$$

Where QY_{Mn} is the Mn luminescence, τ_{ET} is the energy transfer rate, and τ_{EX} is the exciton relaxation rate. This method is not entirely accurate since it does not consider the contributions of nonradiative relaxation and other pathways that are created from this. Pump-probe transient absorption is a technique that can be used to measure the energy transfer rate from monitoring the decay rates of intraband absorption of the exciton. Olano found that this showed energy transfer rates of 10s of ps but this did not take into account the interference from other factors that can result in fast relaxation.[88] A more accurate way to determine the energy transfer rate is from the comparative analysis of the undoped QD and doped QD. They should be spectroscopically similar so the fast process that are not from energy transfer can be accounted for which would be seen in the undoped QD.

This was probed by Chen et al by preparing core shell CdS/ZnS QD with Mn doped at different distances and concentrations from the core.[48] This allowed for understanding how the distance and concentration of Mn would affect the energy transfer from the exciton. In this study it showed that the rate of energy transfer decreased as the Mn was moved further away from the core. The energy transfer mechanism is thought to be Dexter due to its spin forbidden nature so it will be exponentially dependent on distance of the exciton and Mn wavefunction overlap. This can explain the decreased efficiency of the energy transfer rate as the Mn is moved further away from the core decreasing the overlap since the exciton wavefunction is localized to the core. The amount of Mn will also increase the efficiency of energy transfer since there are more acceptors, but this will affect the lifetime and QY. From this it is important to balance the amount of Mn and its location to have an optimal energy transfer rate as well as maintain the long lifetime and high QY.

This study also showed that the major competing pathway with Mn energy transfer is from hole trapping.

2.3.2 Copper Doping in II-VI QDs[†]

Another avenue producing new luminescence in doped QDs is by introducing dopants that function as the charge carrier recombination center, where one of the charge carriers localized on or near the dopant radiatively recombines with the remaining charge carrier.[89] Among the doped QDs that can exhibit the luminescence via dopant-centered charge carrier recombination, Cu-doped II-VI QDs were the most extensively studied. The dopants that can produce the luminescence via similar mechanism includes Ag^{+}, Cr^{3+} and Ni^{2+}, while they have not been explored as extensively as Cu dopant.[90] In contrast to Mn luminescence, the energy of Cu luminescence varies widely depending on the host QDs, e.g., 3 eV in Cu-doped ZnS QD and 0.9 eV in $Cu_2ZnSn(S_{1-x}Se_x)_4$ QD.[91, 92] The Cu luminescence decays on μs time scale, because it involves the recombination of the localized charge carrier exhibiting much lower oscillator strength than the delocalized exciton.[93]

Earlier literature discussing the luminescence from Cu-doped QDs had two different views on the oxidation state of the dopant between Cu^{+} [94-97] and Cu^{2+},[98-100] which fueled many detailed studies to identify the oxidation state of the dopant. Various optical,[97, 101] electron spin resonance,[102, 103] X-ray absorption spectroscopic[95, 104-106] and computational studies[107] were performed to clarify this issue. The full scope of the discussion of this issue can be found in a recent review[93], the highlights of the key arguments supporting each view are described here.

[†] Reproduced from Qiao, Tian.; Parobek, David.; Son, Dong Hee. Photons and charges from colloidal doped semiconductor quantum dots *J. Mat. Chem. C* **2019**. *7, 14788-14797* with permission from the Royal Society of Chemistry

Studies by Gamelin and coworkers described the Cu luminescence as coming from QDs doped with Cu^+, where the rapid localization of the hole by Cu^+ after the photoexcitation of exciton results in the radiative recombination of the localized hole with the remaining electron.[97] (Figure 13a) In this picture, the initial hole localization on Cu^+ produces Cu^{2+} like state, which returns back to Cu^+ through the recombination with the electron giving rise to Cu luminescence.[97] The authors supported Cu^+ state of the dopant in Cu-doped QDs by comparing the calculated absorption spectra of Cu^+- and Cu^{2+}-doped CdSe clusters (Cu^+:$Cd_{33}Se_{34}$ and Cu^{2+}:$Cd_{33}Se_{34}$).[107] In their work, they argued that only Cu^{2+}:$Cd_{33}Se_{34}$ exhibit distinct valence band-to-metal electron transfer transition extending into the near infrared (NIR) region at < 1eV, which has been experimentally observed in bulk ZnS doped with Cu^{2+} but not in Cu-doped ZnS QDs. The authors also reported the observation of valence band-to-metal electron transfer in the transient absorption studies of Cu-doped CdSe/CdS core/shell QDs as a weak photoinduced absorption, fortifying the mechanism of forming a Cu^{2+} state through hole localization at Cu^+ after photoexcitation.[101] In addition, the absorption peak at 2.7 eV in the calculated absorption spectrum of Cu^+:$Cd_{33}Se_{34}$, attributed to the transition of the electron in Cu^+ to the conduction band of the host. was observed experimentally below the band to band transition in Cu-doped CdSe QDs.[97] These results were taken as a strong support for the argument that the oxidation state is Cu^+ in Cu-doped QDs.

On the other hand, studies by Klimov and coworkers suggested that the dopant exists as Cu^{2+} in the QDs and acts as a permanent hole in the QD that recombines with the electron in the conduction band to produce the dopant luminescence and Cu^+. (Figure 13b) [108] In their study, they reported magnetic circular dichroism (MCD) data of Cu-doped ZnSe/CdSe QDs showing an enhanced Zeeman splitting of 2.5 meV indicative of magnetic activity associated with Cu^{2+} with d^9 as opposed to Cu^+ with d^{10} configuration of *d* electrons. On the other hand, this has been disputed

by another study that reported the absence of electron paramagnetic resonance (EPR) signal and MCD from Cu-doped CdSe, InP and $CuInS_2$ QD, leaving room for further clarification.[97] The authors also observed the increase of Cu luminescence intensity when dodecanethiol was introduced to the Cu-doped ZnSe/CdSe QD surface, which acts as the hole trap that removes the hole produced in the valence band of the host after the photoexcitation.[108] This observation was interpreted as the result of the competition between the permanent hole on Cu^{2+} and the photogenerated hole in the valence band in the recombination with the electron in the conduction band, supporting Cu^{2+} dopant state. However, the absence of the channel regenerating Cu^{2+} state from Cu^{+} after charge carrier recombination that is required to sustain Cu luminescence under continued photoexcitation was pointed out as a weakness of Cu^{2+} scenario.[97]

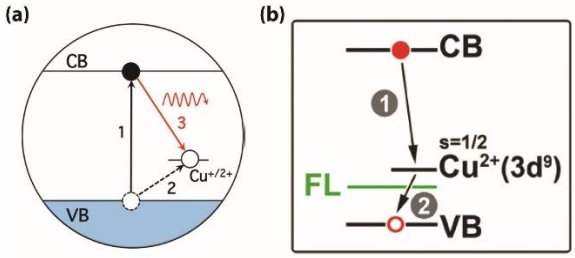

Figure 13. (a) Copper dopant exists in the QDs as Cu^{+} that rapidly localizes a hole after the photoexcitation. The localized hole recombines with the electron to emit a photon. Reprinted with permission from Knowles, E. K.; et al. *J. Am. Chem. Soc.* **2015**, *137*, 40, 13138-13147 Copyright 2015 American Chemical Society. (b) Copper dopant exists in the QDs as Cu^{2+} that acts as a permanent hole, which recombines with the electron to emit a photon. Reprinted with permission from Viswanatha, R.; et al. *Nano Lett.* **2011**, *11*, 11, 4753-4758 Copyright 2011 American Chemical Society.

2.3.3 Theory of Energy Transfer

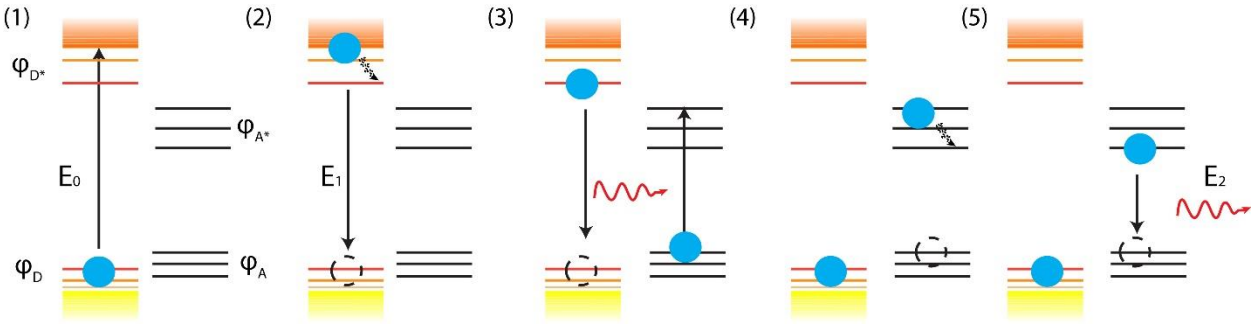

Figure 14. Representation of energy transfer process. φ_D, φ_A, φ_{D^*}, φ_{A^*} represent the ground and excited donor and acceptor states respectively. E_0, E_1, and E_2 represents the excitation energy, donor relaxation energy, and acceptor relaxation energy respectively.

When studying the photophysical properties of a material it is important to understand the potential transitions that can occur. One such process, is that of energy transfer from a donor ion (D) to an acceptor ion (A).[109] This can occur either through coulombic interaction (FRET) or exchange interaction (Dexter) between D and A. This process can be described to occur in five stages as shown in Figure 14. The first is step is the absorption of a photon (E_o) by D which is then followed by the relaxation of the lattice around D so the available radiative transition is $E_1 < E_o$. This step occurs in the order of 10^{-13} s and is associated with the Stokes shift. The third step is the transfer of the energy to A. The fourth step is the relaxation of the lattice around D so the available electronic energy is $E_2 < E_1$. The final step is the emission of E_2 from A. From the difference in energy between E_2 and E_o back energy transfer is typically not considered. The energy transfer rate in step 3 is dependent the distance between D and A as well as the concentration of A. The probability (P_{DA}) for this process can be represented as shown in equation (2).

$$P_{DA} = \frac{2\pi}{\hbar}\left|\langle\psi_{D^*A}|\hat{H}|\psi_{DA^*}\rangle\right|^2 \int g_D(E)\, g_A(E)\, dE \qquad (2)$$

Where ψ_{D^*A} is the wavefunction that represents the initial step where D is in an excited state and A is in the ground state and ψ_{DA^*} is the wavefunction that represents the final step where D is in its ground state and A is in an excited state. The $g_D(E)$ term is the donor emission spectral profile while $g_A(E)$ is the acceptor absorption spectral profile, which when integrated accounts for the spectral overlap between D and A.

The transition probability $\left|\langle\psi_{D^*A}\left|\hat{\mathrm{H}}\right|\psi_{DA^*}\rangle\right|^2$ is represented by equation (3).

$$\langle\varphi_{D^*}(r_1)\varphi_A(r_2)\left|\hat{\mathrm{H}}\right|\varphi_D(r_1)\varphi_{A^*}(r_2)\rangle \times \langle\chi_{D^*}(\sigma_1)\chi_A(\sigma_2)\left|\hat{\mathrm{H}}\right|\chi_D(\sigma_1)\chi_{A^*}(\sigma_2)\rangle -$$
$$\langle\varphi_{D^*}(r_1)\varphi_A(r_2)\left|\hat{\mathrm{H}}\right|\varphi_{A^*}(r_1)\varphi_D(r_2)\rangle \times \langle\chi_{D^*}(\sigma_1)\chi_A(\sigma_2)\left|\hat{\mathrm{H}}\right|\chi_{A^*}(\sigma_1)\chi_D(\sigma_2)\rangle \quad (3)$$

The terms φ_D, φ_A, φ_{D^*}, φ_{A^*} represent the donor state, acceptor state, excited donor state, and excited acceptor state respectively. $\chi(\sigma)$ represents the spin state and r_1 and r_2 represent the position of the electrons involved. The first term in equation (3) represents the Coulombic interactions and the second term is representative of Exchange interactions. Whenever the transition occurring preserves the spin ($\chi_D = \chi_{D^*}$ and $\chi_A = \chi_{A^*}$) and is not forbidden then the coulombic term dominates and the exchange interactions can be ignored.

To compute the energy transfer probability the Hamiltonian $\hat{\mathrm{H}}$ must be determined which represents the interaction between D and A. For the case where the transition is allowed then $\hat{\mathrm{H}}$ is expressed as the sums of Coulombic interactions of the outer and core electrons of D and A. This interaction is reduced by the dielectric medium of the lattice and expanded as a Taylor series. This can be represented by equation (4).

$$\hat{\mathrm{H}} = \frac{1}{4\pi\varepsilon}\sum_{ij}\frac{e^2}{\vec{R}+\overrightarrow{r_{Aj}}+\overrightarrow{r_{Di}}} \quad (4)$$

Where ε is the dielectric constant $\vec{R}$ is the vector between D and A, $\overrightarrow{r_{Di}}$ and $\overrightarrow{r_{Aj}}$ are the vectors of the electrons from the D state and A state respectively. When this is expanded it gives dipole-dipole, dipole-quadruple, and higher order interactions but these are omitted since when there is an allowed transition the dipole-dipole term dominates. From the application of the Hamiltonian the probability for energy transfer in a dipole-dipole system is shown in equation (5).

$$P_{DA}^{dd} = \frac{4\pi}{3\hbar}\left(\frac{1}{4\pi\varepsilon}\right)^2 \frac{1}{R^6} |\langle\mu_D\rangle|^2 |\langle\mu_A\rangle|^2 \int g_D(E)\, g_A(E)\, dE \tag{5}$$

The $|\langle\mu_D\rangle|^2, |\langle\mu_A\rangle|^2$ terms are the matrix element of the electric dipole for D and A respectively and are proportional to the oscillator strength of the transition. The ($1/R^6$) is the distance dependence for the energy transfer to occur and is iconic of the FRET process.

If spin is not conserved the $|\langle\mu_A\rangle|^2$ would be zero which would result in the probability for the energy transfer to occur through dipole-dipole interactions go to zero. This would result in a spin forbidden transition and rely on the exchange interaction from the second term in equation (3). The Hamiltonian for this process represents the electrostatic interaction between D and A which is shown in equation (6).

$$\hat{\mathrm{H}} = \sum_{ij} \frac{e^2}{\varepsilon \overrightarrow{r_{ij}}} \tag{6}$$

This then gives the following probability for energy transfer to occur through exchange interaction shown in equation (7).

$$P_{DA}^{ex} = \frac{2\pi e^4}{\hbar\varepsilon^2} \left| \langle \varphi_{D^*}(r_i) \varphi_A(r_j) \left| \Sigma_{ij} \frac{e^2}{\varepsilon \overrightarrow{r_{ij}}} \right| \varphi_{A^*}(r_i) \varphi_D(r_j) \rangle \right|^2 \int g_D(E)\, g_A(E)\, dE \tag{7}$$

This is representative of Dexter energy transfer. The distance dependence of the energy transfer probability is represented by the exponential function exp(-2R/L), where L is the Bohr radius for the excited and unexcited states of D and A.

2.3.4 Hot Electron Generation in II-VI QDs[‡]

As described earlier an electron is considered hot when it is at a higher temperature than the lattice and it possess excess energy. In semiconductors, this can be achieved either by exciting the electron into the conduction band before it relaxes through multi-photon excitation or via high energy photons. This is a limiting factor of hot electron generation since the access for these routes of excitation are not typical of solar radiation. The benefit of using Mn-doped QDs is from the long-lived Mn excited state due to its spin forbidden nature that can facilitate two photon upconversion generating hot electrons as shown in figure 15. First a photon is absorbed by the host creating an electron hole pair. Then when the exciton relaxes it can transfer its energy to Mn^{2+} putting it into an excited state. From the long millisecond lifetimes, the Mn^{2+} can stay in its excited state while the host absorbs a second photon creating an exciton. If all of the Mn is in an excited state then back energy transfer can occur from the Mn to the conduction band electron, resulting in a hot electron.

[‡] Reprinted with permission from Parobek, David.; Qiao, Tian.; Son, Dong Hee. erspective: Energetic hot electrons from exciton-to-hot electron upconversion in Mn-Doped semiconductor nanocrystals *J. Chem. Phys.* **2019**. *151, 120901*

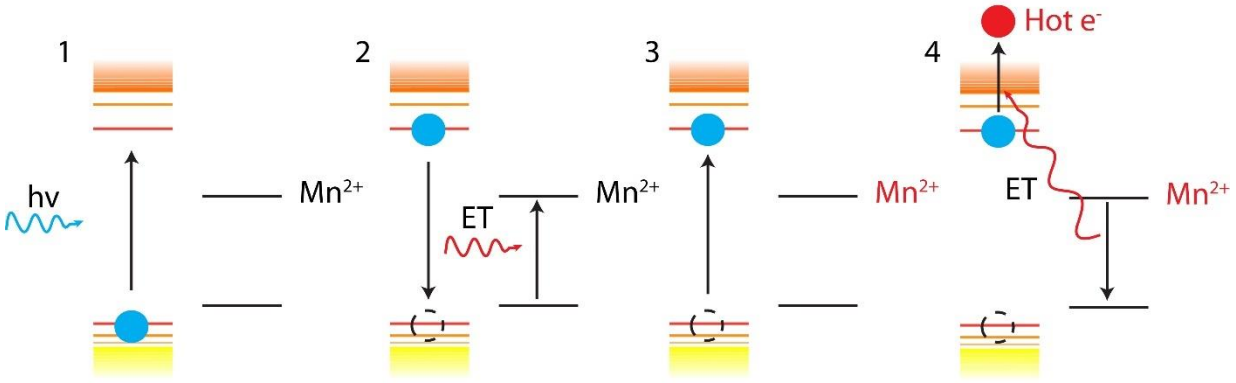

Figure 15. Mechanism for two photon up-conversion for Mn doped QDs. (1) A photon is absorbed by a material followed by the creation of an electron hole pair. (2) Energy transfer from the relaxation of the exciton to the Mn^{2+} putting it in an excited state. (3) A second photon creates another electron-hole pair while the Mn^{2+} is still in an excited state. (4) Back energy transfer can occur to the conduction band electron resulting in a hot electron.

Multiple works by our group and others have shown prototype devices utilizing hot electrons to overcome energetic barriers producing a photocurrent with experimental conditions that directly rely on the photophysical properties received from Mn dopants. In the first iteration of these devices, Son and coworkers utilized an electrochemical cell with an ITO/Al_2O_3/QD electrode in a polysulfide solution with a Pt counter electrode (Figure 16a).[110] The Al_2O_3 layer acted as an energy barrier with a conduction band level ~2 eV above the conduction band of the CdS host QD. Under low intensity *cw* excitation conditions undoped CdS/ZnS QDs did not possess enough energy to hop or tunnel through the Al_2O_3 insulating layer resulting in no signal being received above the noise level of the detector. Following the same conditions, Mn-doped QDs are capable of overcoming the energy barrier of the insulating Al_2O_3 layer producing a photocurrent which follows a superlinear excitation dependence exhibiting a biphotonic process. In the experiment, the Mn-doped QDs were capable of producing a photocurrent through Al_2O_3 layers with thicknesses of 5.4 and 7.5 nm producing a current density of 400 nA/cm^2 and 50 nA/cm^2 respectively under an excitation intensity of 1.5 W/cm^2 (Figure 16b). This provides evidence that

under low intensity *cw* excitation conditions Mn-doped QDs are capable of producing high energy hot electrons that can hop over energetic barriers in excess of 2 eV of energy as well as penetrate through layers as thick as 7.5 nm.

Gamelin and coworkers also designed a device which used Mn doped QDs to generate hot electrons that were capable of overcoming an energetic barrier producing a photocurrent.[111] Their device used a 4 layer scheme with an aluminum contact, 175 nm layer of $Cd_{1-x}Mn_xS$, 50 nm ZnS layer, and ITO (Figure 16c). In their study, they changed the direction and magnitude of the applied bias to see how it affected the Mn PL intensity and in turn the received photocurrent. Interestingly, under a + 15V bias the Mn PL intensity had decreased by 75% with the photocurrent signal increasing beyond the point of 1 photon per electron showing a gain value of 175 from hot electron impact ionization throughout the QD and ZnS layer. This effect was not seen under negative biases or with undoped QDs which both showed minimal PL quenching under with these conditions. They explored further into the effect the gain had on the systems signal and when they performed the same experiment with a 20Hz lock in frequency the signal dropped considerably from incident photon to current value of 17500% to 30% also indicating a large time constant decay for the gain mechanism(Figure 16d). This shows the potential importance of the gain received from the impact ionization from the hot electrons generated in detecting the photocurrent. The previous works were using devices similar to a metal insulator metal scheme which provides an insulating barrier requiring the QDs to overcome an energy barrier or tunnel through the layer. This requires the hot electrons to provide excess kinetic energy to overcome the barrier.

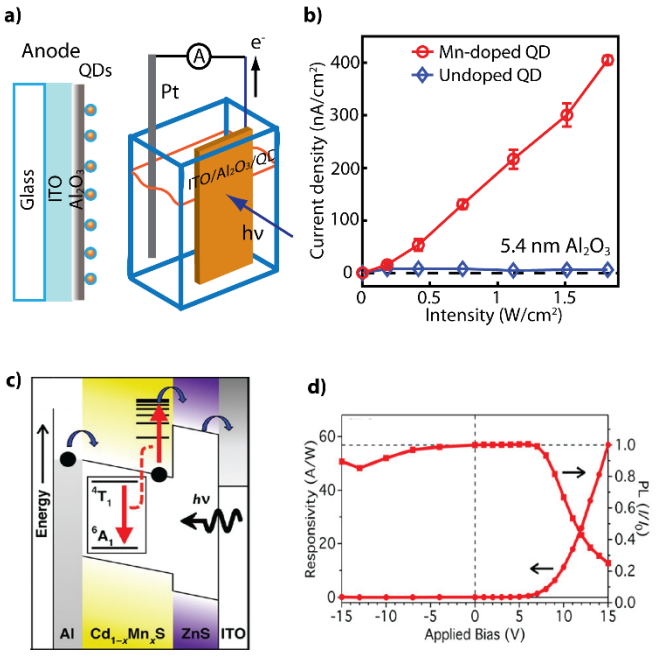

Figure 16. Hot electron photocurrent measurement. (a) Photoelectrochemical cell that detects hot electron photocurrent from Mn-doped QDs, (b) Comparison of photocurrent measured with anodes deposited with Mn-doped and undoped QDs, (c) Structure of the photodiode detecting hot electron photocurrent, (d) Bias-dependent Mn PL intensity and responsivity of photodiode. Reproduced with permission from Dong, Y.; et al. *ChemPhysChem*, **2016.** *17,* 660 Copyright 2016 from the Royal Chemistry Society. (a,b) and with permission from Barrows, C. J.; et al. *J. Phys. Chem. Lett.* **2016,** *8,* 126. Copyright 2016 American Chemical Society.

To further test the limits of the hot electrons Son and coworkers creating a device that requires the hot electrons to possess enough energy to be emitted into vacuum.[112] The conduction band level of the CdS QD is ~ to 3 eV below vacuum level and can receive ~ to 2 eV of energy from back energy transfer from the Mn excited state. From the large bandwidth of Mn (300 meV) from the large vibronic coupling, this provides the potential for a portion of the hot electrons to be above the vacuum level. In this scheme the Mn-doped QDs were attached to an ITO glass slide which was then placed parallel to a copper electrode with a 1.5 mm spacer separating them and kept under vacuum (Figure 17a,b). In this experiment, they studied the location and concentration of Mn in the QD to see how it affected the photocurrent from the ejected electrons. As described

previously the hot electron generation rate is related to the efficiency of the energy transfer to the Mn dopants in the QD. The greater the overlap between the wavefunction between the Mn dopants and the exciton of the core QD will result in a faster energy transfer time. This can be done by moving the manganese dopants closer to the QD core as well as increasing the concentration. This has its drawbacks though typically resulting in shorter Mn lifetimes which would then require higher a higher photon flux to saturate the Mn dopants and sustain hot electron generation. Three types of doping conditions were tested in the experiment with the Mn being on the 2^{nd} layer with high and low doping concentration and Mn on the core with a high doping concentration. The hot electron photocurrent intensity followed as expected with the highest signal coming from the sample with Mn on the core and a higher doping concentration (Figure 17c). The energy of the hot electron could not be completely mapped from the experiment, but its upper limits could be determined by applying a negative bias to the electrodes. This could act as an energy barrier stopping electrons that did not possess enough kinetic energy to overcome the applied bias. The hot electrons generated showed to have an excess of 0.4 eV of energy above the vacuum level with the signal decreasing to the noise level and higher negative biases (Figure 17d). This provides a basis for the capabilities hot electrons possess and how this long-range electron transfer could be applied to other applications such as photocatalysis which will be discussed later.

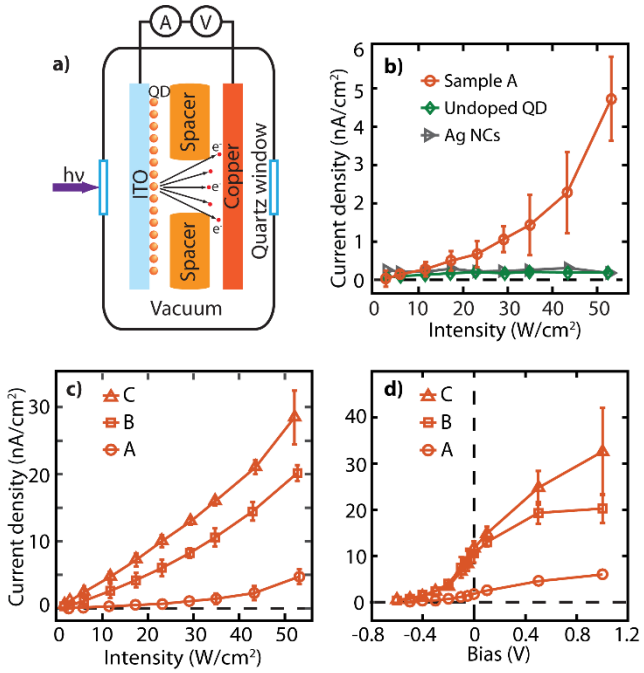

Figure 17. Photoelectron emission of hot electrons. (a) Diagram of electrodes for detecting photoelectron emission from hot electrons, (b) Comparison of the current density from photoelectrons between Mn-doped QD, undoped QD and plasmonic Ag NC, (c) Comparison of the current density from three different Mn-doped QDs (Sample A, B, C) with different exciton-to-Mn energy transfer times ($\tau_A > \tau_B > \tau_C$), (d) Bias-dependent current density at 29 W/cm^2 of excitation intensity. Reproduced with permission from Dong, Y.; et al. *Nano Lett.* **2016.** *16*, 7270. Copyright 2016 American Chemical Society.

2.4 Photocatalysis

Finding alternative sources of energy to fossil fuels has been a highly active area of research due to the limited quantity of fossil fuels and their negative environmental impact. In today's global society the total energy consumption of the world is 16.3 TW which is only predicted to rise. The concentration of CO_2 is also predicted to increase to 590 ppm by 2100 will result in rising global temperatures and sea levels. The energy that hits the Earth from the sun is around 1.3 x 10^5 TW, which is 10000 times the amount of energy needed per year. This has led scientists to try and discover ways to utilize this source of free energy as a way to create new fuel sources through water splitting or energy storage via chemical bonds.[113]

In 1979 one of the first examples of photocatalysis was published by Fujishima, who utilized TiO_2 semiconductor powders to produce carbon feedstocks from CO_2.[114] TiO_2 is a heavily researched wide band gap semiconductor used in photocatalysis due to its higher stability compared to narrow band gap systems.[115] An inherent issue of TiO_2 is its wide band gap which only absorbs UV light which only accounts for 5% of the total energy from the sun. This has led to coupling TiO_2 with photosensitizers (i.e. dyes) that can absorb the light and then transfer an electron to the conduction band of TiO_2. The use of molecular photosensitizers has their limitations from low absorption cross sections to instability over long periods of light exposure. The use of semiconductor QDs has gained attention since they are not limited by these issues and also possess a wide range of tunability from quantum confinement effects.[116]

The large absorption cross section and the tunability of absorption throughout the visible has made QDs popular photosensitizers for photocatalysis. H_2 is an energy rich fuel source which has made it a target product for photocatalysis reactions. There are many examples of QD systems effectively reducing H_2 but the efficiency suffers due to the fast electron-hole recombination.[116] One strategy that has been successful at separating the electron from the hole is attaching a noble metal to the QD. One example that has become a model system for this is use CdS nanorods with a platinum tip.[117] In this system, with a CdSe seed in the CdS nanorod with only one Pt tip had efficiencies up to 27% and stable for over 12 hours of excitation (Figure 18a).[118] The high stability originates from the effective separation of the hole from the CdS nanorod which prevents it from oxidizing and Pt is a common co-catalyst which can effectively generate H_2. The use of molecular catalysts instead of noble metals has also reported highly efficient systems. Krauss and coworkers showed that with a CdSe QD and a Ni-dihydrolipoic acid complex they could achieve over 600000 turnovers which was stable over 360 hrs of excitation (Figure 18b).[119]

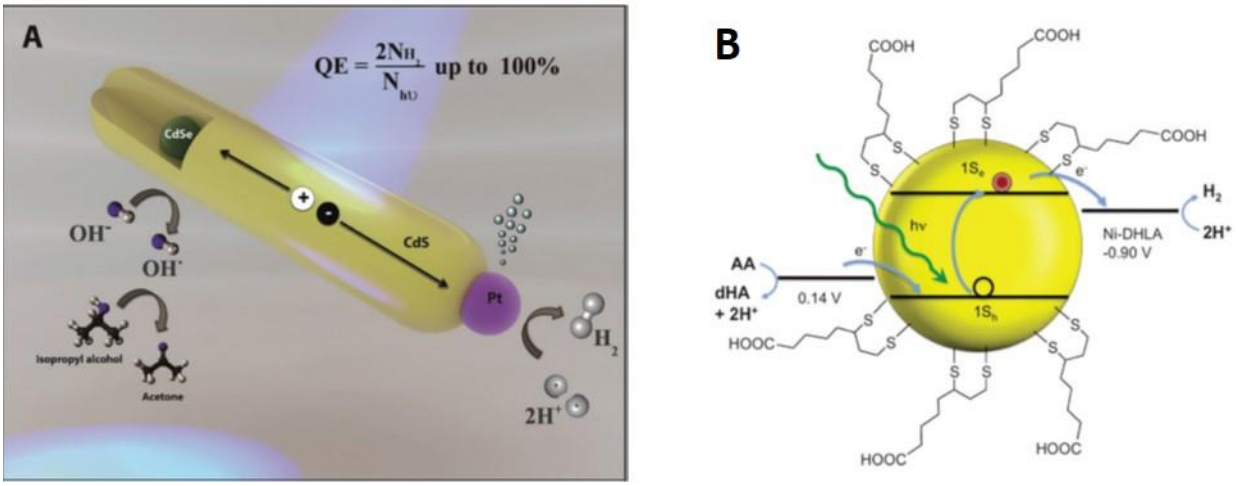

Figure 18. (a) Illustration of photocatalytic hydrogen production process using Pt-tipped CdSe@CdS nanorods. Reprinted with permission from Kalisman, P.; et al. *Nano Lett.* **2016**, *16*, 3, 1776-1781. Copyright 2016 American Chemical Society (b) Diagram showing the photocatalytic hydrogen production using CdSe QDs and Ni-DHLA cocatalyst. Reprinted with permission from Han, Z.; et al. *Science* **2012.** *228*, 6112, 1321-1324. Copyright 2012 American Association for the Advancement of Science.

While H_2 can provide an energy dense fuel source to replace oil and gas, a large amount of consumer products and chemicals are derived from the oil industry. CO_2 is a stable compound that can be used to create other carbon feedstocks (i.e. CO, CH_4, HCO_2H) (Table 1) that are used in chemical industry. Its accumulation in our atmosphere is a major cause for global warming so having the capability to remove and turn it into a useful resource would be promising. The downside of CO_2 being chemically stable is that reduction it to other products is difficult. CO_2 is a linear molecule and when electron transfer occurs to the LUMO, the C-O bond length increases causing a geometric distortion. This results in a high reduction potential to facilitate the reorganization energy of this distortion making outer sphere uncoupled electron transfer not very probable.[120] The cost of this reaction is reduced through inner sphere multielectron transfer when CO_2 binds to a substrate. The selectivity of a specific reduction product (i.e. CH_4, CO, HCOOH)

can be difficult though from the similar reduction potentials and in aqueous phase H_2 generation can also dominate complicating the reaction further.

Table 1. Reduction potential for CO_2 and H_2O in aqueous condition at pH 7 vs SHE[113]

Reaction	**Voltage (SHE)**
$CO_2 + e^- \rightarrow CO_2^{*-}$	-1.850
$CO_2 + H_2O + 2e^- \rightarrow HCOO^- + 2OH^-$	-0.665
$CO_2 + H_2O + 2e^- \rightarrow CO + 2OH^-$	-0.521
$CO_2 + 5H_2O + 6e^- \rightarrow CH_3OH + 6OH^-$	-0.399
$CO_2 + 5H_2O + 6e^- \rightarrow CH_4 + 8OH^-$	-0.246
$H_2O + 2e^- \rightarrow H_2 + 2OH^-$	-0.414

Transition metal complexes composed of Ni, Mn, Fe, and Co have been heavily studied as substrates to bind CO_2 from their multiple redox states that can facilitate the multielectron process for its reduction. Ni is an abundant transition metal that will undergo a reduction from square planar Ni^{2+} to a tetrahedral Ni^+ which results in its ligand typically being tetradentate.[120] A highly studied Ni metal catalyst is 1,4,8,11-tetraazacyclotetradecane (cyclam) from its high selectivity and turnover frequency for CO generation in aqueous solutions (Scheme 1).[121] While metal complexes are efficient at reducing chemical species they need a supply of electron which are typically received through electrochemical means. In photocatalytic reactions the metal catalyst needs to be attached to a photosensitizer with a linker molecule to ensure electron transfer.

Scheme 1. Proposed CO_2 reduction catalytic cycle for $[Ni(cyclam)]^{2+}$

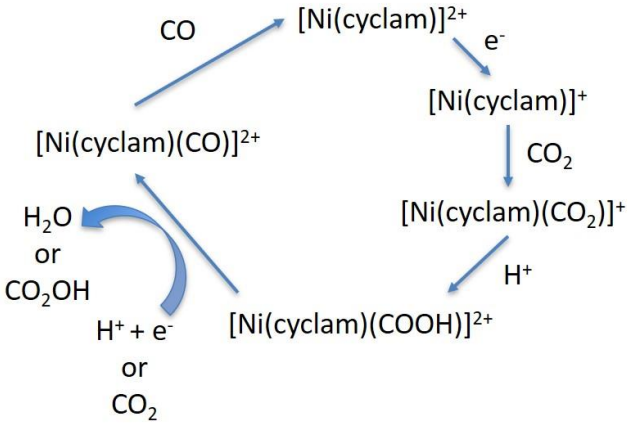

For the effective generation of CO from CO_2 most QD systems require the usage of a metal catalyst due to the inability of the CO_2 to outcompete proton binding at the surface.[122-125] The catalyst can be bound to the QD through either electrostatic interactions with the capping ligand[123] or through the covalent attachment of the catalyst to the QD.[124, 125] In either case it is necessary to have the catalyst in the vicinity of the QD to have efficient charge transfer to the catalyst before exciton recombination occurs. The metal catalyst is also necessary since they are designed specifically to bind to the CO_2 instead of hydrogen, resulting in the generation of CO. In most of these systems though there is still competition with H_2 generation since there are multiple binding sites on the QD surface and the catalyst loading can vary based on the ligand used. For example Kuehnel et al. showed that when an additional capping ligand was used in their ZnSe-[Ni(cyclam)P] system the amount of H_2 production was decreased from the lack of binding sites available for the proton.[125] They also showed that the CO generation is directly dependent on the catalyst loading by changing the binding ligand on the metal catalyst. In a CdS-Ni(terpy) they varied the binding molecule (thiol, phosphoric acid, carboxylic acid) and showed that with the higher amount of metal catalyst the CO increased while the H_2 generation decreased while the lowest loading had predominately H_2 (Figure 19a,b).[124] This increases the difficulties of these

systems since they are directly dependent on the ability of the metal catalyst to find binding sites on the QDs.

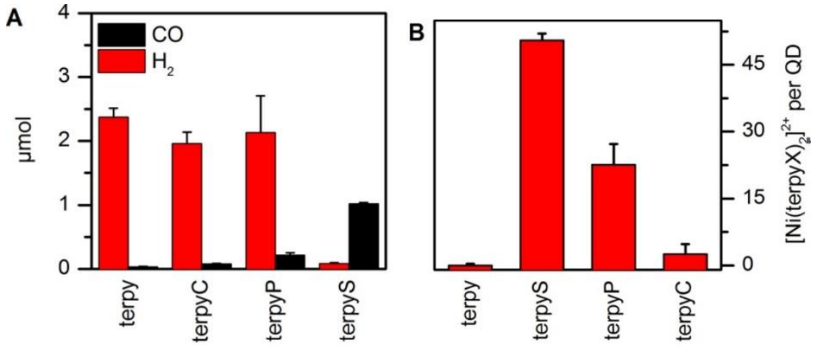

Figure 19. (a) Generation of CO and H_2 with respect to the type of anchor group on the Ni(terpy) catalyst. (b) The amount of Ni(terpy) bound to the QD surface for each anchor group used. Reprinted with permission from Kuehnel, M. F.; et al. *J. Am. Chem. Soc.* **2017**, *139*, 21, 7217-7223. Copyright 2017 American Chemical Society.

There are only a few examples of using solvated electrons generated from semiconductors for photocatalysis due to the difficulty in generating them. A solvated electron is made when a material can emit an electron that can then be solvated in a cavity in the liquid. While the solvated electrons possess a great deal of reduction capability it takes high energy UV photons to create them. Hamers et al. were able to generate solvated electrons from H_2 terminated diamond with a UV laser excitation source for the production of ammonia from N_2.[126] The conduction band of diamond is located above the vacuum level so each electron created has a chance to be emitted and solvated in the solvent. They believed that the solvated electrons were able to destabilize the hydrazine that forms during the multi electron reaction to form ammonia.[127] They also showed that the solvated electrons were able to selectively reduce CO_2 into CO even in an aqueous solution due to the faster kinetics of the CO_2 to CO compared to H_2 generation.[128] While the limiting factor of using solvated electrons is its reliance on UV excitation, the usage of hot electrons in photocatalysis has been displayed for Mn-doped II-VI QDs. Dong et al. showed that hot electrons

are more efficient than band edge electrons at generating H_2 under visible light excitation.[33] This provides a potential platform to utilize high energy hot electrons that have the chance of becoming solvated without the restrictions of UV excitation.

CHAPTER III

EXCITON-TO-DOPANT ENERGY TRANSFER IN MN-DOPED CESIUM LEAD HALIDE PEROVSKITE NANOCRYSTALS[§]

3.1 Introduction

Colloidal nanocrystals of semiconducting perovskites have become a subject of intense research in recent years due to their superb luminescence properties and facile chemical tunability of the bandgap, which is attractive in many applications where colloidal quantum dots have been very successful as a source for photons or charge carriers[15, 17, 18, 20, 129]. In particular, all-inorganic cesium lead halide ($CsPbX_3$) nanocrystals have shown great potential for outperforming commonly used II-VI metal chalcogenide quantum dots from their capability to harvest photons, create charge carriers, and generate photons from the recombination of charge carriers efficiently, even in the absence of a passivating shell[15]. The facile modification of the bandgap via post-synthesis anion-exchange is also a unique attribute of perovskite nanocrystals for chemical tuning of their properties[17, 18].

In II-VI semiconductor quantum dots, doping with transition metal ions has been extensively explored as a way to introduce new optical, electronic and magnetic properties, making them much more functional than their undoped counterparts[36]. For instance, substitutional isoelectronic doping of MX (M=Cd, Zn, X=S, Se) quantum dots with paramagnetic transition metal ions such as Mn^{2+} can generate intense sensitized dopant luminescence[46, 130] and create a magnetically-coupled exciton state enabling optical control of magnetism[131] or production of energetic hot electrons via exciton-to-hot carrier upconversion[33, 132]. These new properties of Mn-

[§] Reprinted with permission from Parobek, David.; Roman, Benjamin.; Dong, Yitong.; Jin, Ho.; Lee, Elbert.; Sheldon, Matthew.; Son, Dong Hee. Exciton-to-Dopant Energy Transfer in Mn-Doped Cesium Lead Halide Perovskite Nanocrystals *Nano Lett*., **2016** *16(12)* 7376.

doped quantum dots result from the exchange coupling between the charge carriers of the host semiconductor and *d* electrons of the dopant, which opens new pathways of energy exchange or forms new coupled electronic states between the exciton and dopant[87, 133]. One may anticipate new optical, electronic and magnetic properties also in $CsPbX_3$ perovskite semiconductor nanocrystals, similar to Mn-doped II-VI quantum dots, if Mn^{2+} ions can be doped in $CsPbX_3$ nanocrystals stably with sufficiently strong exchange coupling between the charge carriers.

Here, we successfully synthesized Mn-doped $CsPbCl_3$ and $CsPb(Cl/Br)_3$ nanocrystals exhibiting a strong sensitized Mn luminescence, indicative of the presence of the exchange coupling between the exciton and Mn sufficiently strong to mediate efficient energy transfer between them. This suggests that one may expand the range of the host semiconductor nanocrystal materials to include $CsPbX_3$ perovskites to obtain new properties originating from the exchange coupling between the charge carriers and magnetic dopant ions, beyond the extensively studied II-VI quantum dots. The common difficulties faced with the synthesis of Mn-doped colloidal semiconductor nanocrystals, in general, arise from the fact that the incorporation of Mn^{2+} ions in the lattice of small nanocrystals is usually kinetically unfavorable[134]. For this reason, many strategies to synthesize Mn-doped quantum dots rely on the delicate kinetic control of the growth and doping process during synthesis[46, 49, 130, 135]. In the case of doping $CsPbX_3$ nanocrystals, almost instantaneous formation of $CsPbX_3$ nanocrystals during the solution-phase synthesis, and the quaternary elemental composition of the doped nanocrystals make identification of the optimum combination of precursors and synthetic conditions more challenging than the case of ternary systems.

3.2 Experimental Section

3.2.1 Synthesis of Mn-doped and undoped $CsPbCl_3$ and $CsPb(Cl/Br)_3$ NCs

The Cs-oleate solution was made in a similar way for all the following synthesis. Cs_2CO_3 (0.402 g), OA (1.74 mL), and ODE (18 mL) were added to a 50-mL 3-neck round bottomed flask and evacuated and refilled with nitrogen 3 times then heated to 150 °C for at least 10 minutes before use. The $CsPbCl_3$ ($CsPb(Cl/Br)_3$) was synthesized by adding $PbCl_2$ (0.0661 g) ($PbCl_2$ (0.0857 g) and $PbBr_2$ (0.0755 g)) , OAm (0.8 mL), OA (0.8 mL), and ODE (5 mL) to a 25-mL 3 neck round bottom flask and were evacuated and refilled with N_2 followed by heating the solution to 120 °C for 30 minutes. The solution was then increased to 165 °C and then 200 °C for 10 minutes each. At 200 °C, dried OAm (0.8 mL) and dried OA (0.8 mL) were subsequently injected to solubilize the solution. Then the Cs-oleate (0.4 mL) was swiftly injected and after 1 minute the solution was cooled with an ice bath. The NCs were precipitated with acetone and the centrifuged followed by dissolving in hexanes. The Mn-doped $CsPbCl_3$ ($CsPb(Cl/Br)_3$) was synthesized following the same procedure as above but had $PbCl_2$ (0.0615 g) ($PbBr_2$ (0.0775 g)), $MnCl_2{\cdot}(H_2O)_4$ (0.0615 g), OAm (0.8 mL), OA (0.8 mL), and ODE (5 mL) added to a 25-mL 3 neck round bottom flask.

3.2.2 Purification and elemental analysis of Mn-doped $CsPbCl_3$ and $CsPb(Cl/Br)_3$ NCs

To purify the nanocrystals, gel permeation chromatography (GPC) was used following a similar method by Shen et al.[61] Prior to use, 4 g of poly(styrene-divinylbenzene) gel was soaked in toluene overnight and then packed into a column with toluene as the mobile phase. The perovskite samples were then loaded into the column and run through multiple times to ensure the removal of excess Mn-oleate or Mn-oleylamine complexes. The first 2 mL of the eluent

nanocrystals were collected for each run followed by the measurement of the absorption, emission, and Mn doping concentration. The optical properties of the NC show little change after being put through the column multiple times (Figure 20a,b) while the elemental analysis (Figure 20c) also confirms that the excess Mn was removed giving a final doping concentration that converges at 0.2%.

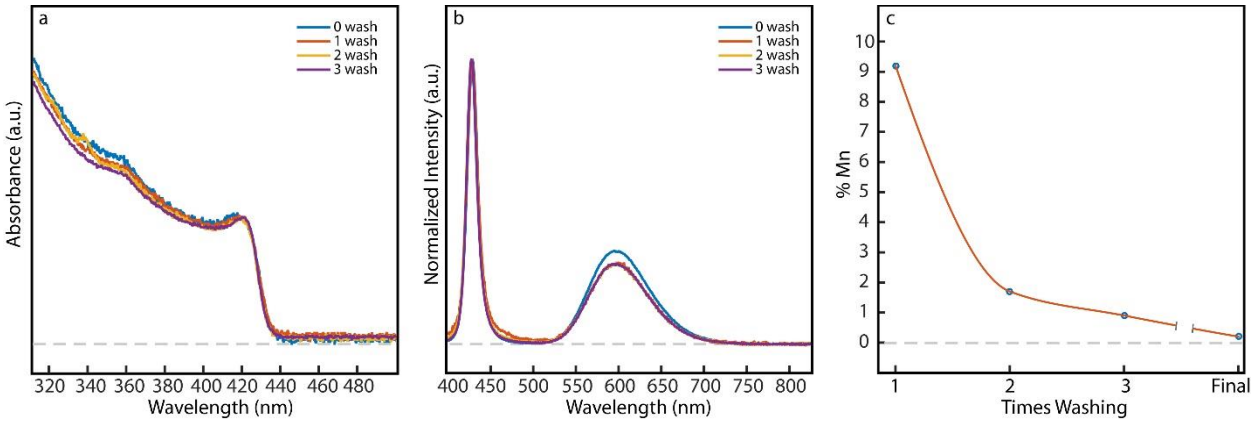

Figure 20. (a) Absorption spectra of unwashed Mn-doped $CsPb(Cl/Br)_3$ and after being washed multiple times. (b) Emission spectra of of unwashed Mn-doped $CsPb(Cl/Br)_3$ and after being washed multiple times. (c) Elemental analysis of %Mn doping concentration correlated to the amount of times run through the GPC column.

The doping concentration and elemental composition was determined by using both inductively coupled plasma mass spectrometry (ICP-MS) (NexIon 300D) and scanning electron microscopy energy dispersive x-ray spectroscopy (SEM-EDS) (FEI Quanta 600 FE-SEM). For the ICP-MS the samples were digested in concentrated nitric acid followed by sonication. The standard solutions were made through a serial dilution and measured gravimetrically to construct the calibration curve to quantify the amount of Cs, Pb, and Mn. The doping concentration $\langle n_{mn} \rangle$ was calculated in the following way.

$$[NCs] = \frac{[Cs^+]}{1000} \tag{8}$$

Where [Cs^+] is the concentration of Cs in the solution and [NCs] is the amount of NCs present.

$$< n_{Mn} \geq \frac{[Mn^{2+}]}{[NCs]} \quad (9)$$

The halide composition for the mixed halide system was determined from the SEM-EDS. The samples were prepared by drying them under vacuum overnight and placing them on a carbon substrate where multiple locations were scanned (Figure 21a, b).

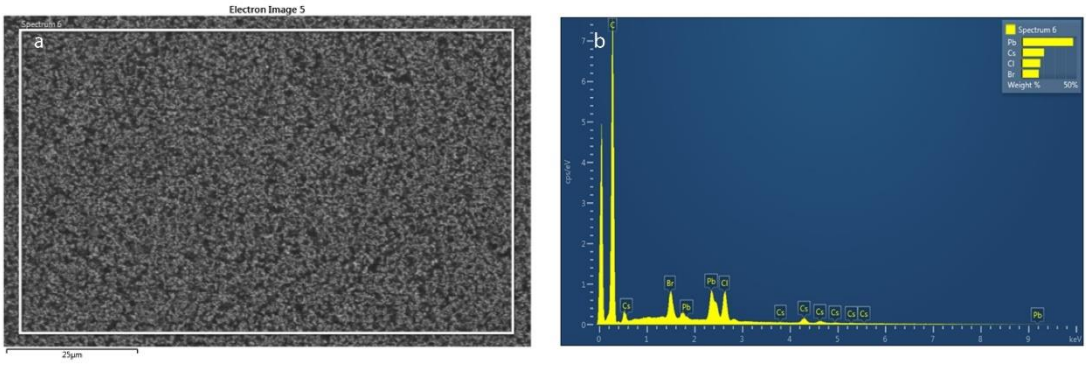

Figure 21. (a) SEM scan of Mn-doped $CsPb(Cl/Br)_3$ perovskite nanocrystals. (b) SEM/EDS atomic composition of Mn-doped $CsPb(Cl/Br)_3$ perovskite nanocrystals.

3.3 Results and Discussion

In this study, Mn-doped $CsPbX_3$ nanocrystals were prepared via a one-pot synthesis method using $MnCl_2$ as the precursor, employing a modified version of the reported synthesis method[15] for $CsPbX_3$ nanocrystals as shown in Scheme 2. Further details of the synthesis are in the experimental section. Among the various organometallic and halide Mn precursors tested, $MnCl_2$ resulted in the most consistent production of Mn-doped nanocrystals. Briefly, $PbCl_2$ (0.22 mmol) and $MnCl_2{\cdot}(H_2O)_4$ (0.31 mmol) were added into a mixture of oleylamine (0.8 ml), oleic acid (0.8 ml), and 1-octadecene (5 ml). After heating the mixture to 120-200 °C, additional oleylamine and oleic acid was injected to dissolve the metal salts. Subsequently, 0.4 ml of a cesium-oleate solution in 1-octadecene (64 mM) was swiftly injected into the heated metal salt

solution, which immediately formed Mn-doped $CsPbCl_3$ nanocrystals in seconds. The reaction mixture was quenched with an ice bath after the completion of the reaction, and the nanocrystals were precipitated with acetone then suspended in hexanes. When $PbBr_2$ was used as the precursor instead of $PbCl_2$, the resulting Mn-doped perovskite nanocrystals had mixed halide composition, *i.e.* $CsPb(Cl/Br)_3$, and the exciton PL redshifted from that of $CsPbCl_3$.[17, 18] The ratio of Cl/Br in $CsPb(Cl/Br)_3$ was determined to be 4.4:1 according to the energy dispersive X-ray spectroscopy (EDS) performed on a scanning electron microscope. The control, undoped $CsPbX_3$ nanocrystals were also synthesized under similar experimental condition.

Scheme 2. Schematic representation of synthetic procedure for Mn-doped $CsPbCl_3$.

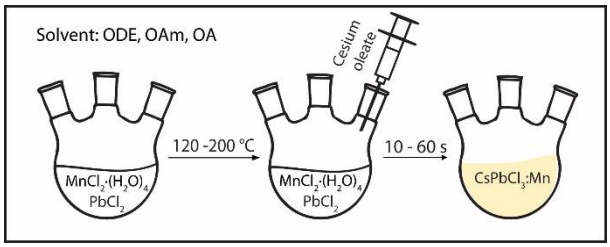

Because of the large excess amount of Mn precursors and low doping efficiency in the host nanocrystal, thorough purification of Mn-doped $CsPbX_3$ nanocrystals is important for the reliable determination of the doping concentration. The usual precipitation/resuspension cycles, which is effective for purifying other semiconductor nanocrystals such as II-VI metal chalcogenides, could not completely remove the unreacted Mn source from the reaction product. This is likely due to the insufficient difference in the solubility of Mn-doped $CsPbX_3$ nanocrystals and Mn^{2+} complexes (*e.g.,* Mn-oleate) in the solvents used for the purification. For this reason, gel permeation chromatography (GPC) was used for further purification of the nanocrystals.[61] Separation of the nanocrystals from the remaining contaminants that are trapped in the pores of the gel with (<3nm pore size) was very effective enabling more reliable measurement of doping concentration via

elemental analysis. The details of the GPC purification procedure and the robustness of optical spectra of Mn-doped $CsPbX_3$ nanocrystals after many cycles of GPC are described in section 3.2.2.

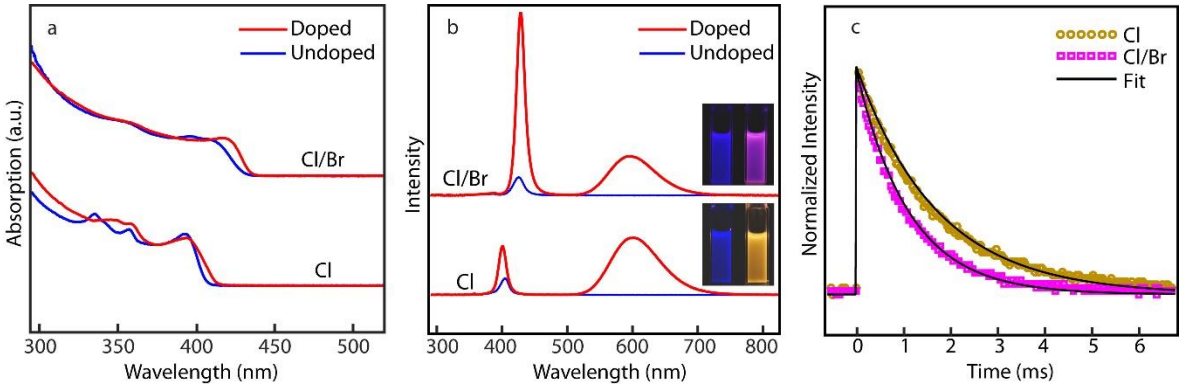

Figure 22. (a) Absorption spectra of Mn-doped and undoped $CsPbCl_3$ and $CsPb(Cl/Br)_3$ nanocrystals. (b) Photoluminescence of Mn-doped and undoped $CsPbCl_3$ and $CsPb(Cl/Br)_3$ nanocrystals. Insets are photographs of the sample under UV excitation. (c) Time-dependent Mn luminescence intensity from Mn-doped $CsPbCl_3$ and $CsPb(Cl/Br)_3$ nanocrystals. Solid lines are the fit to a single-exponential function.

Figure 22a compares the absorption spectra of Mn-doped $CsPbCl_3$ and Mn-doped $CsPb(Cl/Br)_3$ nanocrystals with those of the undoped nanocrystals. The Mn-doping concentrations determined from elemental analysis are ~0.2% for $CsPbCl_3$ and $CsPb(Cl/Br)_3$. The absorption spectra of the host perovskite nanocrystals show minor changes at these doping concentrations, indicating the relatively weak effect of the doped Mn^{2+} ions on the electronic structure of the host nanocrystals. While a weak absorption from the lowest-energy ligand field transitions of Mn^{2+} ($^6A_1 \rightarrow {}^4T_1$) was observed at 500-550 nm in bulk $CsMnX_3$ crystal[136], it is virtually absent in the absorption spectra of Mn-doped $CsPbX_3$ nanocrystals shown in Figure 22a due to the spin forbidden nature of the transition. Figure 22b compares the photoluminescence spectra of Mn-doped and undoped nanocrystals upon excitation at 365 nm above the band-edge absorption of the host perovskite nanocrystals. While undoped nanocrystals exhibit the narrow exciton luminescence only, Mn-doped nanocrystals exhibit a broad luminescence attributed to the ligand

field transition ($^4T_1$-$^6A_1$) of Mn^{2+} ions at ~600 nm, in addition to the exciton luminescence of the host. The insets are the photographs comparing the luminescence of undoped (left) and Mn-doped (right) nanocrystals dispersed in hexanes. A long lifetime of the 600 nm luminescence (1-2 ms), shown in Figure 22c, further supports that it originates from the spin forbidden ligand field transition of the doped Mn^{2+} ions. For both undoped $CsPbCl_3$ and $CsPb(Cl/Br)_3$ nanocrystals, the exciton luminescence quantum yield is relatively low (<5%), unlike in $CsPbBr_3$ nanocrystals that exhibited much higher quantum yield (> ~60%) in separate experiments and in a previous report[18]. However, doping these nanocrystals with Mn^{2+} ions produces much more intense Mn luminescence compared to the exciton luminescence of the undoped nanocrystals as shown in Figure 22b. Exciton luminescence in Mn-doped $CsPbCl_3$ and $CsPb(Cl/Br)_3$ nanocrystals also increased substantially compared to their undoped nanocrystals, reaching the overall luminescence quantum yields of 30-60%. Table 2 summarizes the quantum yield of undoped and Mn-doped $CsPbX_3$ nanocrystals.

Table 2. Quantum yields of doped and undoped $CsPbX_3$ perovskite

Sample	Exciton QY (%)	Mn QY (%)	Total (%)
$CsPbCl_3$	1.1	-	1.1
Mn:$CsPbCl_3$	1.3-3.5	22-58	26-60
$CsPb(Cl/Br)_3$	1.8	-	1.8
Mn:$CsPb(Cl/Br)_3$	15	16	31

The intense Mn luminescence upon the excitation of the host nanocrystals indicates that Mn^{2+} ions doped in $CsPbX_3$ host serve as an efficient energy acceptor, competing favorably with the nonradiative relaxation pathways. The efficient energy transfer from exciton to Mn^{2+} ions possessing very weak transition dipole relies on the exchange coupling between the donor and

acceptor, similar to the case of Mn-doped II-VI quantum dots[87]. Therefore, the appearance of strong sensitized Mn luminescence indicates the presence of sufficiently strong exchange coupling between the charge carriers of $CsPbX_3$ nanocrystals and *d* electrons of Mn^{2+} ions, which is also capable of introducing new optical and magnetic properties originating from it. On the other hand, it is intriguing to observe the increase of exciton luminescence after Mn doping, although the reason is unclear requiring further investigations. This suggests that the competitive kinetics between radiative and nonradiative relaxation is altered by Mn doping. It is unlikely to have an increased exciton luminescence via reversible energy exchange between exciton and Mn transitions, similarly to Mn-doped CdSe[72], due to the large differences in the transition energies between the two. Considering the low quantum yield of exciton luminescence in undoped $CsPbX_3$ nanocrystals containing Cl as halide, doping may remove some of the preexisting structural defects responsible for the low quantum yield. Compared to Mn-doped II-VI nanocrystals, where the energy transfer can occur on a several picosecond time scale at Mn doping concentration of <1%[48] leaving no residual exciton emission, the exciton luminescence of the host perovskite nanocrystals still persists suggesting a weaker coupling of the exciton and Mn dopant in $CsPbX_3$ nanocrystals compared with II-VI host nanocrystals, further studies are needed to gain additional insights into the strength of this coupling. Direct time-resolved measurement of the energy transfer rate in Mn-doped perovskite nanocrystals is under way for a quantitative understanding of the energy transfer dynamics in this system. Nevertheless, we attempted to estimate an approximate energy transfer time (τ_{ET}) under the assumption that quantum yield of Mn luminescence (QY_{Mn}) can be expressed as follows[137], despite the limitation of this simple analysis.

$$QY_{Mn} = \left(\frac{\frac{1}{\tau_{ET}}}{\frac{1}{\tau_{ex}} + \frac{1}{\tau_{ET}}} \right) \quad (10)$$

Here, τ_{ET} and τ_{ex} are the energy transfer time and the exciton relaxation time respectively. For $CsPbCl_3$ nanocrystals with QY_{Mn}=0.58 and τ_{ex}= ~5ns, the calculated energy transfer time is τ_{ET} =3.6 ns.

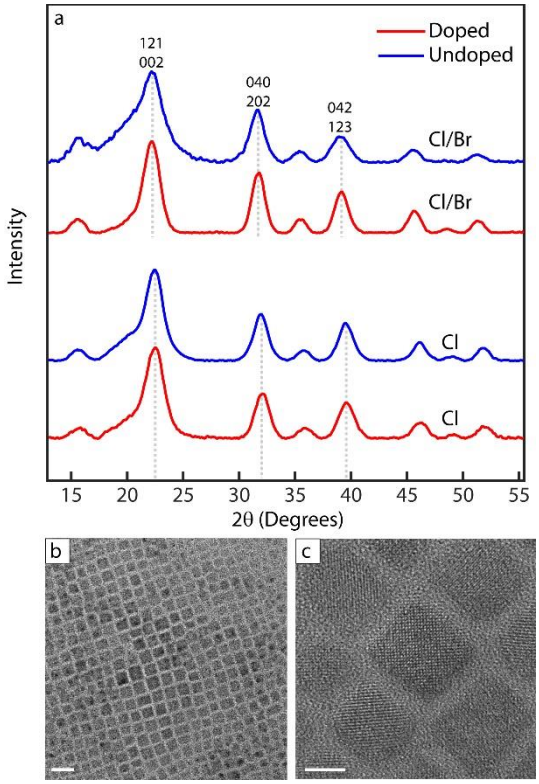

Figure 23. (a) XRD patterns of Mn-doped and undoped $CsPbCl_3$ and $CsPb(Cl/Br)_3$ nanocrystals. X-ray λ=1.54056 Å. Miller indices of the orthorhombic $CsPbX_3$ structure are indicated at the top of the figure. (b,c) TEM images of Mn-doped $CsPb(Cl/Br)_3$ nanocrystals. Scale bar is 20 nm and 5 nm respectively

Table 3. X-ray diffraction angle (2θ) of perovskite nanocrystals.

Sample\hkl	**121/002**	**040/202**	**042/123**
Mn:CsPbCl3	22.5°	32.0°	39.6°
CsPbCl3	22.5°	32.0°	39.6°
Mn:CsPb(Cl/Br)3	22.2°	31.7°	39.1°
CsPb(Cl/Br)3	22.2°	31.7°	39.1°

In order to obtain structural information of Mn-doped $CsPbX_3$ nanocrystals, transmission electron microscopy (TEM), X-ray diffraction (XRD) and electron paramagnetic resonance (EPR) measurements were made. Figure 23a compares the XRD patterns of Mn-doped $CsPbCl_3$ and Mn-doped $CsPb(Cl/Br)_3$ nanocrystals with those of the undoped nanocrystals obtained using Cu K-α emission line. Although bulk $CsMnX_3$ crystallizes in a hexagonal lattice structure, distinct from the orthorhombic structure of $CsPbX_3$, XRD patterns of Mn-doped $CsPbX_3$ nanocrystals show the peaks of only the orthorhombic phase, which is nearly identical to that of undoped host nanocrystals. Rietveld refinement analysis of the XRD patterns[138] were used to confirm that both the doped and undoped nanocrystals adopted an orthorhombic phase of space group *Pnma*(62), consistent with recent results by Cottingham and Brutchey on $CsPbBr_3$[139]. This indicates that there is no detectable phase separation between $CsPbX_3$ and $CsMnX_3$ in the doped nanocrystals at the doping concentrations of this study. The comparison of the diffraction angles (2θ) of several planes in undoped and Mn-doped nanocrystals listed in Table 3 shows that Mn^{2+} ions can be accommodated, likely substituting the sites of Pb^{2+} ions as in bulk Mn-doped $CsPbX_3$ crystals[140], with little change in the lattice parameters. TEM images of the Mn-doped nanocrystal shown in Figure 23b and 23c, also indicate that the size control and high crystallinity of the host structure are preserved in the synthesis of Mn-doped perovskite nanocrystals.

At ambient temperature Mn-doped $CsPbCl_3$ and Mn-doped $CsPb(Cl/Br)_3$ nanocrystals display a single-exponential decay of Mn luminescence with a lifetime of 1.75 ms and 1.12 ms respectively. In contrast, the luminescence lifetimes of Mn^{2+} ions in bulk $CsMnCl_3$ and $CsMnBr_3$ crystals from direct excitation of the weak ligand field transition, where Mn^{2+} ions are antiferromagnetically coupled, are 110 μs and 10 μs respectively[141]. More than an order of magnitude longer lifetime in Mn-doped perovskite nanocrystals is consistent with larger spatial separation between Mn^{2+} ions that suppresses the antiferromagnetic coupling responsible for the short Mn luminescence lifetime[142]. Figure 24a,b compares the normalized exciton and Mn luminescence spectra of several single particles and solution ensemble of Mn-doped $CsPb(Cl/Br)_3$ nanocrystals. In contrast to the exciton luminescence varying from particle to particle due to the size heterogeneity in the ensemble and quantum confinement effect, Mn luminescence spectra from different particles are indistinguishable from each other and from the ensemble spectrum. In fact, the energy and bandwidth of Mn luminescence and its lifetime are generally sensitive to the local lattice structure at the doping site that determines the structure and strength of the ligand field on Mn^{2+} ions as well as the vibronic coupling. In the case of the extensively studied Mn-doped II-VI core/shell quantum dots, with radially varying local ligand fields at the doping sites due to lattice strain, Mn luminescence spectra exhibited a strong dependence on the doping location within the quantum dot and often display multi-exponential decay due to the heterogeneity of the local environment at the doping sites [48, 143]. In principle, the local environment of Mn^{2+} ions in $CsPbX_3$ nanocrystal host can be heterogeneous due to the large surface/volume ratio, such that a significant portion of Mn^{2+} ions may reside on the surface. However, the highly homogeneous spectral characteristics and single exponential decay of Mn luminescence suggest the relatively uniform local lattice environment at the Mn doping sites in near-cubic (orthorhombic) host lattice

at least for those Mn^{2+} ions contributing to the observed sensitized luminescence. An X-band EPR spectrum of Mn-doped $CsPbCl_3$ nanocrystals at room temperature shown in Figure 24c exhibits the hyperfine structure and splitting (86 Gauss) very close to those of bulk Mn-doped $CsPbCl_3$ crystals grown in a furnace at high temperature reported in an earlier study[140], where Mn^{2+} ions occupy Pb^{2+} sites with an octahedral ligand field. This observation further corroborates the relative uniformity of the doping sites resulting in highly homogeneous spectral characteristics of the dopant luminescence in the perovskite nanocrystal host.

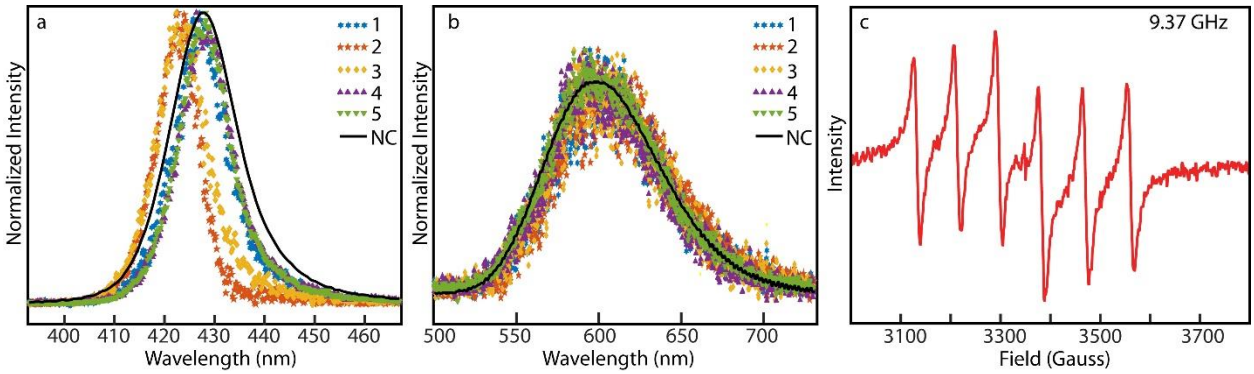

Figure 24. (a,b) Spectra taken from several single particles comparing the normalized exciton (a) and Mn luminescence (b) of each one (dot) with the ensemble measurement of Mn-doped $CsPb(Cl/Br)_3$ nanocrystals (line). (c) X-band EPR spectrum of Mn-doped $CsPbCl_3$ nanocrystal at room temperature.

3.4 Conclusion

In conclusion, we report a colloidal synthetic approach for the doping of Mn^{2+} ions into $CsPbCl_3$ and $CsPb(Cl/Br)_3$ perovskite nanocrystals. Both species exhibited strong dopant luminescence characteristic of *d-d* transition of Mn^{2+} ions resulting from exciton-to-Mn energy transfer, similar to the case of Mn-doped II-VI quantum dots. XRD, EPR and luminescence lifetime data indicate that the host nanocrystal structure is nearly intact after doping and that Mn^{2+} ions are located in the lattice, likely substituting Pb^{2+}. The successful synthesis of Mn-doped

perovskite nanocrystals and the observation of intense sensitized Mn luminescence show the potential of $CsPbX_3$ nanocrystals as the host of the magnetically doped quantum dots that can take advantage of the coupling between excitons and the *d* electrons of paramagnetic dopants for expanded functionality.

CHAPTER IV

DIRECT HOT-INJECTION SYNTHESIS OF Mn-DOPED $CsPbBr_3$ NANOCRYSTALS[**]

4.1 Introduction

The promising capabilities of cesium lead halide nanocrystals ($CsPbX_3$ NCs) for photovoltaic[144] and optoelectronic[145] applications have driven immense interest in expanding the range of their useful properties via further chemical and structural modification. For example, recent works have demonstrated relatively facile tuning of the bandgap and electronic structure via chemical or photochemical anion/cation-exchange[17-19, 146] and achieving extremely high luminescence quantum yield via simple surface modification.[16] Similarly to other semiconductor NCs,[36, 93] doping has also been explored extensively as a major way to modify the material properties in $CsPbX_3$ NCs expanding their functionality.[19, 54, 58, 69] Among these, doping of Mn^{2+}, which is well known to introduce many interesting optical, electronic and magnetooptic properties resulting from the exchange coupling of exciton and Mn^{2+} seen in II-VI semiconductor NCs,[33, 48, 56, 131, 147] is being actively pursued in anticipation of the same benefits in $CsPbX_3$ NCs. The first successful doping of Mn^{2+} ions in $CsPbX_3$ NC host was demonstrated in $CsPbCl_3$[51, 148], which was achieved by a simple modification of the usual hot-injection synthesis method for the undoped NCs, i.e., adding $MnCl_2$ as an additional reactant. Subsequently, various other methods were developed to synthesize Mn-doped $CsPbCl_3$ NCs in a wider range of doping levels.[62, 149, 150] While $CsPbCl_3$ has less desirable characteristics compared to $CsPbBr_3$ or $CsPbI_3$ as the host NCs, such as poor luminescence quantum yield and a high bandgap limiting the visible light absorption, it is

[**] Reprinted with permission from Parobek, David.; Dong, Yitong.; Qiao, Tian.; Son, Dong Hee. Direct Hot-injection Synthesis of Mn-doped $CsPbBr_3$ Nanocrystals, *Chem. Mat.,* **2018**. *30(9), 2939*

the most explored system due to the relative ease of doping. On the other hand, doping Mn^{2+} ions in $CsPbBr_3$ NCs could not be achieved readily by using the same hot-injection method for the synthesis of Mn-doped $CsPbCl_3$ NCs. A recent study suggested that the difficulty of doping Mn^{2+} ions in $CsPbBr_3$, in contrast to the case of $CsPbCl_3$, is due to the larger disparity of M-Br (M=Pb, Mn) bond dissociation energies between $PbBr_2$ (249 kJ/mol) and $MnBr_2$ (314 kJ/mol) compared to $PbCl_2$ (301 kJ/mol) and $MnCl_2$ (338 kJ/mol) precursors.[148] It was argued that the higher stability of Mn-Br bond compared to Pb-Br bond impeded the incorporation of Mn^{2+} in $CsPbBr_3$ lattice. While still not clearly understood yet, the difference in the thermochemistry can certainly be a factor affecting the ability to dope Mn^{2+} in different $CsPbX_3$ NCs. To circumvent the difficulty of doping Mn^{2+} directly into $CsPbBr_3$ NCs via hot-injection method, anion exchange reactions were attempted on Mn-doped $CsPbCl_3$ NCs. While Mn-doped $CsPb(Cl_{1-x}Br_x)_3$ ($x<0.63$) exhibiting Mn luminescence could be obtained,[151] full conversion of the host from $CsPbCl_3$ to $CsPbBr_3$ could not be achieved without entirely losing Mn^{2+} ions during the anion exchange process.

Here, we report the successful direct hot-injection synthesis of Mn-doped $CsPbBr_3$ NCs. The key to doping is the formation of Mn-doped monolayer structure ($L_2[Pb_{1-x}Mn_x]Br_4$, L: ligand) exhibiting intense Mn luminescence as the intermediate structure before injecting the Cs precursor. A strong correlation was observed between the Mn luminescence intensities of the intermediate $L_2[Pb_{1-x}Mn_x]Br_4$ structure and the final Mn-doped $CsPbBr_3$ NCs for a given amount of Mn precursor used. This suggests that the formation of $L_2[Pb_{1-x}Mn_x]Br_4$, which contains the same Mn-Br coordination present in Mn-doped $CsPbBr_3$ NCs, is crucial to enabling the synthesis of Mn-doped $CsPbBr_3$ NCs under a hot-injection condition. The successful Mn-doping in $CsPbBr_3$ NCs demonstrated here will expand the utility of Mn-doped $CsPbX_3$ NCs in their future applications.

4.2 Experimental Section

4.2.1 Synthesis of Mn-doped $CsPbBr_3$ Nanocrystals and $L_2[Pb_{1-x}Mn_x]Br_4$

The cesium-oleate was synthesized by adding Cs_2CO_3 (0.125 g), OA (0.400 g) and ODE (3.500 g) were to a 25-mL three-neck round-bottom flask under N_2 environment in a glovebox. Subsequently, it was transferred to a Schlenk line and heated up to 150 °C for 10 min and lowered to 110 °C until further use. The Mn-doped $CsPbBr_3$ nanocrystals were synthesized by adding $PbBr_2$ (0.16 mmol) and $MnBr_2$ (0.79 mmol) into a mixture of ODE (5 mL), OA (0.7 mL), Olam (0.7 mL) and HBr (0-200 μL of) in a three-neck round-bottom flask. After the evacuation of the flask on a Schlenk line, the reactant mixture was heated to 120 °C under vacuum for 30 mins. At this stage, the intermediate monolayer $L_2[Pb_{1-x}Mn_x]Br_4$ that exhibit Mn luminescence under UV excitation was formed. To produce Mn-doped $CsPbBr_3$ NCs, the intermediate product in the flask was further heated to 200 °C and additional OA (0.7 mL) and Olam (0.7 mL) were injected. After 10 min, 0.4 mL of Cs-oleate was swiftly injected in to the flask, which resulted in the formation of $CsPbBr_3$ NCs in < 1s. After the immediate quenching of the reaction by lowering the temperature using an ice bath, the crude product was precipitated with acetone and centrifuged at 3500 rpm for 10 min. The recovered crude product, which contains both Mn-doped nanocubes and nanoplatelets, was redispersed in hexane for the additional centrifugation to separate each species. After 5 mins of centrifuging at 3500 rpm, Mn-doped $CsPbBr_3$ nanocubes remained in the supernatant and Mn-doped $CsPbBr_3$ nanoplatelets precipitated at the bottom, enabling clean separation of the two species. To isolate $L_2[Pb_{1-x}Mn_x]Br_4$ formed as the intermediate structure, the flask was cooled to room temperature without injecting Cs-oleate. After centrifuging the intermediate product at 3500 rpm for 10 min, the precipitate was dispersed in hexane for the characterization.

4.3 Results and Discussion

Scheme 3 shows the overall synthesis procedure for Mn-doped $CsPbBr_3$ NCs via hot-injection method. The details of the synthesis are in the Experimental Section. The first step involves the formation of the intermediate monolayer $L_2[Pb_{1-x}Mn_x]Br_4$ structure that incorporates Mn^{2+} ions within the structure, which exhibits strong Mn luminescence. Briefly, two precursor compounds ($PbBr_2$ and $MnBr_2$) in the mixture of 1-octadecene (ODE), oleylamine (Olam), oleic acid (OA) and HBr were prepared in a three-neck round-bottom flask and heated to 120°C under vacuum. The intermediate structure produced at this first step showed strong Mn luminescence under UV (370 nm) excitation even at ~160°C. The second step is the injection of Cs-oleate after further heating the flask to 200°C. Right after the injection of Cs-oleate, the flask was rapidly cooled to room temperature and Mn-doped $CsPbBr_3$ NCs were obtained as the final product. Mn-doped $CsPbBr_3$ NCs obtained in this synthesis consists of a mixture of nanocubes and thin nanoplatelets. However, each species is readily separated via simple centrifugation, giving not only the usual nanocubes but also nanoplatelets with potentially stronger exciton-Mn exchange coupling due to the quantum confinement along the thickness direction.

Scheme 3. Synthesis procedure for Mn-doped $CsPbBr_3$ nanocrystals

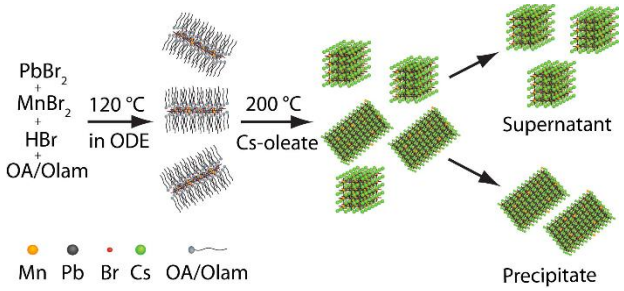

In the first step, $L_2[Pb_{1-x}Mn_x]Br_4$ formed readily when the relative amount of each ingredient ($PbBr_2$, $MnBr_2$, OA, Olam and HBr) was kept close to the condition described in the Experimental section. However, when the relative amount of the organic ligands exceeded significantly from the condition reported here, $L_2[Pb_{1-x}Mn_x]Br_4$ did not form and impeded the ability to obtain Mn-doped $CsPbBr_3$ NCs in the subsequent step. As will be discussed later, the Mn luminescence intensities of $L_2[Pb_{1-x}Mn_x]Br_4$ and Mn-doped $CsPbBr_3$ NCs are strongly correlated, where the Mn luminescence intensity depends on the amount of HBr that controls x in $L_2[Pb_{1-x}Mn_x]Br_4$. It is worth mentioning that several recent studies on the synthesis of Mn-doped $CsPbCl_3$ NCs reported that HCl in the reactant promotes Mn doping in $CsPbCl_3$ host.[65,152] Pradhan et al. proposed that alkyl amine chloride produced by HCl in hot-injection synthesis increases the density of the NCs at the expense of the NC size, increasing the overall chances of Mn doping in $CsPbCl_3$ NCs.[152] Xu et al. proposed that HCl plays two roles in the room-temperature synthesis of Mn-doped $CsPbCl_3$ NCs; increasing the amount of metal monomers facilitating the generation of $CsPbCl_3$ NCs and providing excess Cl^- to the NC surface, therefore increasing the number of potential binding sites for Mn^{2+}.[65] Seemingly, the effect of HBr in this study is similar to that of HCl in the hot-injection synthesis of Mn-doped $CsPbCl_3$ NCs. However, the key role of HBr in the present study is considered increasing x in $L_2[Pb_{1-x}Mn_x]Br_4$ formed in the first step that ultimately leads to the formation of Mn-doped $CsPbBr_3$ NCs.

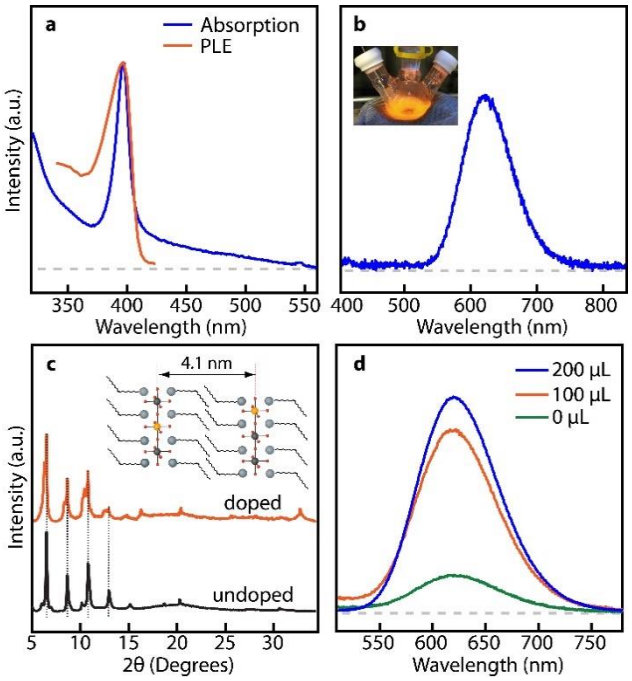

Figure 25. (a) Absorption and PLE spectra and (b) PL spectrum of monolayer $L_2[Pb_{1-x}Mn_x]Br_4$ intermediate structure. (c) XRD patterns of $L_2[Pb_{1-x}Mn_x]Br_4$ (red) and L_2PbBr_4 (black) showing the stacking of multiple layers. In the inset, the orange sphere represents Mn^{2+} replacing Pb^{2+}. (d) Mn luminescence intensity of $L_2[Pb_{1-x}Mn_x]Br_4$ vs the amount of HBr used in the synthesis.

The identity of the intermediate structure exhibiting Mn luminescence as $L_2[Pb_{1-x}Mn_x]Br_4$ and the effect of varying the amount of HBr were examined by optical spectroscopy and X-ray diffraction (XRD). Figure 25a shows the absorption and photoluminescence excitation (PLE) spectra of the intermediate structure formed at the first step when the following amount of the reactants was used: $PbBr_2$ (0.16 mmol), $MnBr_2$ (0.79 mmol), Olam (0.7 mL), OA (0.7 mL), and HBr (200 µL). Figure 25b shows the photoluminescence (PL) spectrum from the intermediate structure in-situ at 120°C under 370 nm excitation and the photograph of the flask the reaction is taking place in. The absorption and PLE spectra in Figure 25a were obtained after cooling the intermediate structure to room temperature.

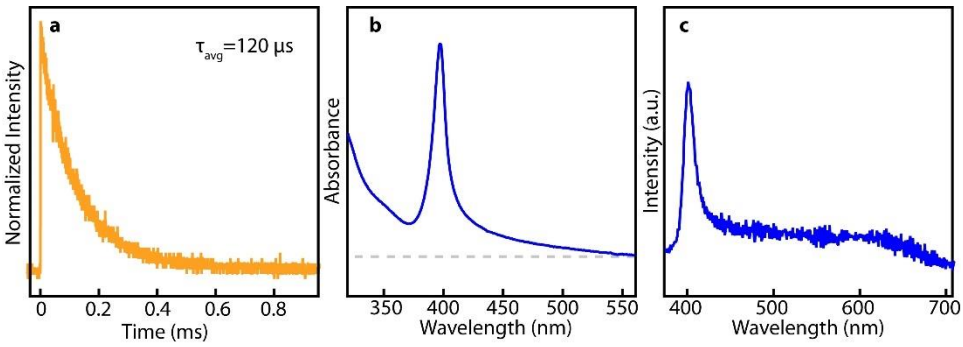

Figure 26. (a) Time-dependent Mn luminescence intensity of $L_2[Pb_{1-x}Mn_x]Br_4$. (b) Absorption and (c) PL spectra of L_2PbBr_4 synthesized with 200 µL of acid.

The absorption spectrum with a prominent peak at 395 nm is very similar to what was previously reported for the monolayer L_2PbBr_4 synthesized through a recrystallization method.[153] However, there is a strong luminescence centered at 620 nm with a lifetime of ~120 µs (Figure 26a) attributed to Mn^{2+} under the appropriate ligand environment, in contrast to L_2PbBr_4 with negligible luminescence (Figure 26b,c). While the observation of Mn luminescence alone does not rule out the possibility of forming L_2PbBr_4 and other Mn-luminescing species separately, the PLE spectrum showing the peak at 395 nm indicates that the observed Mn luminescence is sensitized. This suggests that Mn^{2+} is doped within L_2PbBr_4 host enabling the sensitization of the host excitation to Mn^{2+} ions likely replacing Pb^{2+}.

XRD pattern of the intermediate structure in figure 25c (red) shows the signature of multiple stacked monolayers, similarly to the case of L_2PbBr_4 in the previous study.[153] A series of small angle diffraction peaks (2θ=5-15°) with the equal spacing of 2.2°, corresponding to 4.1 nm for the interlayer distance, is consistent with ~3.5 nm gap between the layers created by the two oleyl carbon chains in the ligands.[154] For comparison, XRD pattern of the stacked monolayer L_2PbBr_4 synthesized in the absence of $MnBr_2$ is also shown in figure 25c (black). Both structures exhibit the same 2.2° spacing between the adjacent diffraction peaks, while the Mn-doped structure

shows a more apparent doublet feature that may reflect the structural distortion of the host due to the incorporation of Mn^{2+}. The above observations suggest that Mn-luminescing intermediate structure is $L_2[Pb_{1-x}Mn_x]Br_4$ with Mn^{2+} ions occupying Pb^{2+} site as illustrated in the inset of figure 25c.

While the microscopic role of HBr in the formation of $L_2[Pb_{1-x}Mn_x]Br_4$ is not entirely clear, its presence increases Mn luminescence intensity of $L_2[Pb_{1-x}Mn_x]Br_4$. When the amount of HBr was varied (0, 100, 200 μL) while keeping the amount of other reactants the same, Mn luminescence intensity of $L_2[Pb_{1-x}Mn_x]Br_4$ increased with the amount of HBr as shown in figure 25d. On the other hand, the absorption spectrum of $L_2[Pb_{1-x}Mn_x]Br_4$ shown in figure 25a did not change significantly with the amount of HBr. These suggest the increase of x in $L_2[Pb_{1-x}Mn_x]Br_4$ with increasing HBr, while retaining the general structure of $L_2[Pb_{1-x}Mn_x]Br_4$. Quantitative determination of x in $L_2[Pb_{1-x}Mn_x]Br_4$ from the elemental analysis, however, could not be performed reliably because of the difficulty in removing all the unreacted Mn^{2+} species.

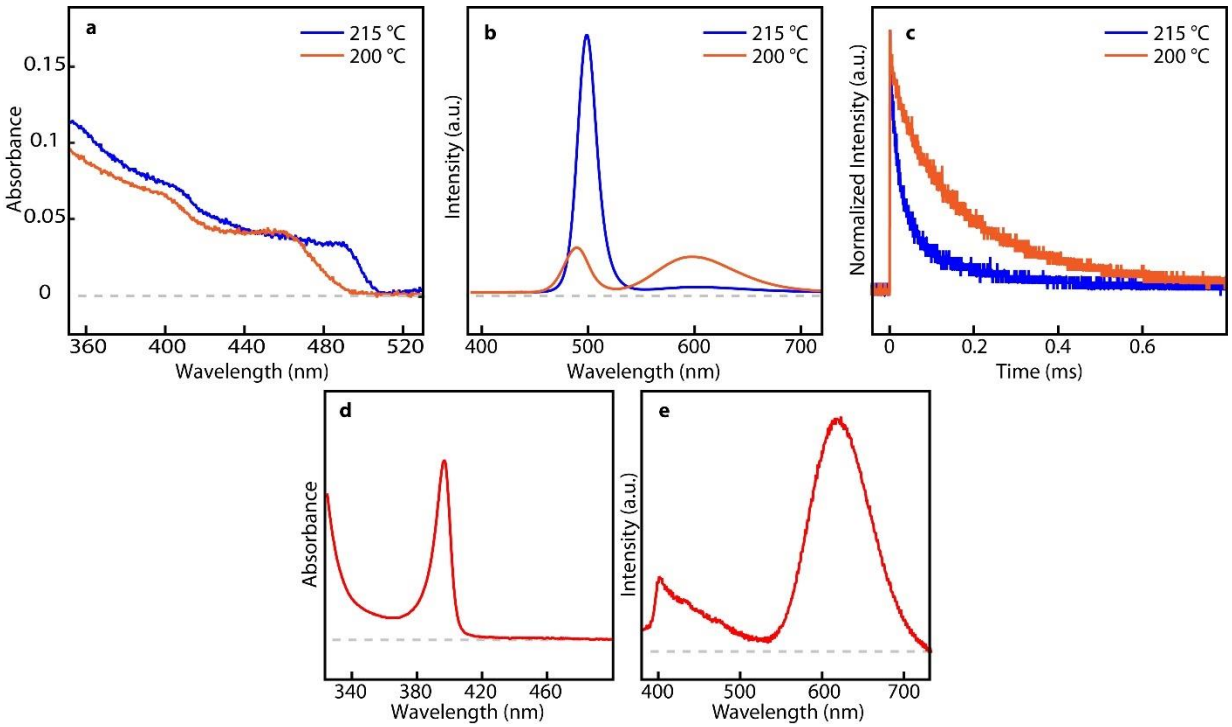

Figure 27. Comparison (a) absorption and (b) PL spectra, and (c) time-dependent Mn luminescence intensity of varying Mn-doped $CsPbBr_3$ nanocubes synthesized at different temperatures. (d) Absorption and e) PL spectra of $L_2[Pb_{1-x}Mn_x]Br_4$ synthesized at 160 °C

Once the intermediate $L_2[Pb_{1-x}Mn_x]Br_4$ structure with strong Mn luminescence is formed in the first step, Mn-doped $CsPbBr_3$ NCs were obtained by injecting Cs-oleate after further heating the reaction mixture to 200 °C. It is important to mention that the relatively high stability of $L_2[Pb_{1-x}Mn_x]Br_4$ exhibiting strong Mn luminescence up to 160 °C required that Cs-oleate be injected at a relatively narrow range of temperatures near 200 °C to obtain Mn-doped $CsPbBr_3$ NCs. Below 160 °C, the majority of the final product after Cs-oleate injection was still Mn-luminescing $L_2[Pb_{1-x}Mn_x]Br_4$ (Fig. 27d,e). At the temperatures significantly above 200 °C, the doping level in the final product decreased drastically (Fig. 27a,b,c).

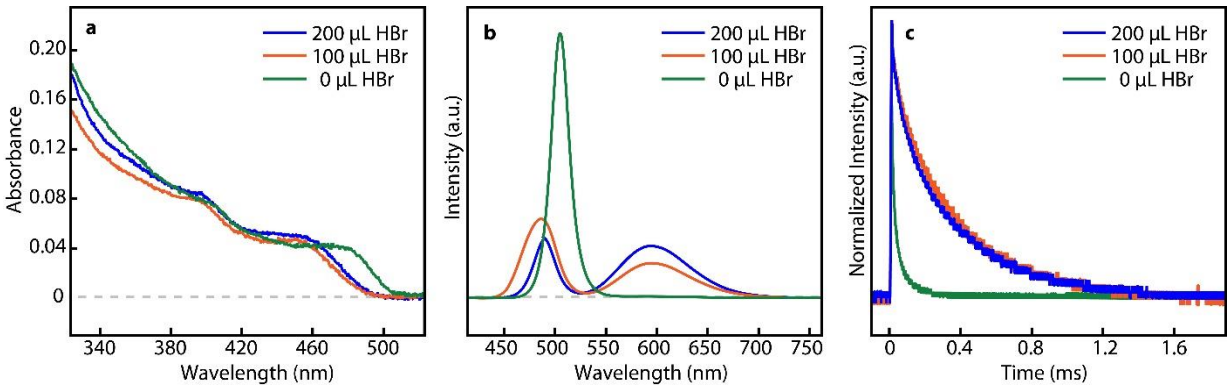

Figure 28. (a) Absorption spectra, (b) PL spectra, (c) Time-dependent Mn luminescence intensity of Mn-doped $CsPbBr_3$ nanocubes synthesized with varying amount of HBr.

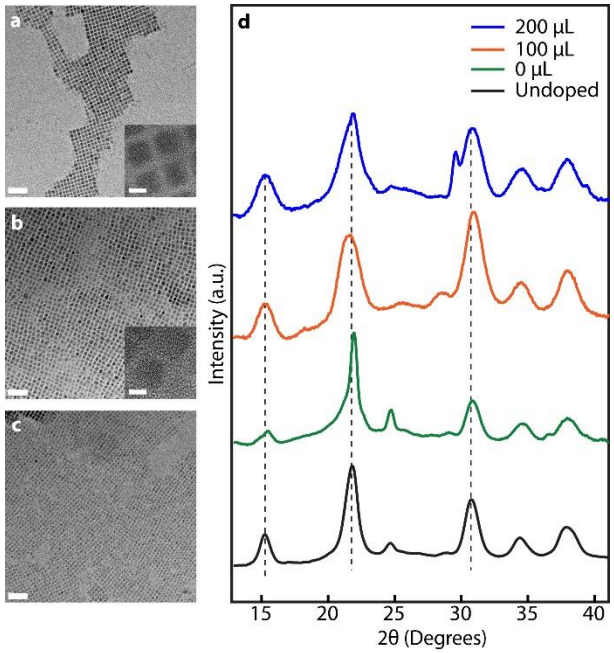

Figure 29. TEM image of Mn-doped $CsPbBr_3$ nanocubes synthesized with (a) 0 µL (b) 100 µL, (c) 200 µL of HBr, (d) XRD patterns of the corresponding Mn-doped $CsPbBr_3$ nanocubes. For comparison, the XRD pattern of undoped $CsPbBr_3$ nanocubes is also shown. Scale bar in (a), (b), (c) is 50 nm. Scale bar of inset in (a) and (b) is 5 nm.

Table 4. Wavelength of the bandedge absorption (λ_{BE}), average NC size, total and Mn luminescence quantum yields (QY_{tot} and QY_{Mn}), and Mn luminescence lifetime (τ_{Mn}) of Mn-doped $CsPbBr_3$ nanocubes.

HBr	λ_{BE} (nm)	Size (nm)	QY_{tot} (%)	QY_{Mn} (%)	τ_{Mn} (μs)
0 μL	480	8.2 ±0.7	40	1.6	24
100 μL	460	8.4 ±1.0	41	20	271
200 μL	455	6.5 ±0.9	38	27	266

Figure 28a-c show the absorption and PL spectra and the time-dependent Mn luminescence intensity of Mn-doped $CsPbBr_3$ nanocubes produced using varying amounts of HBr (0, 100 and 200 μl). As mentioned earlier, while the product is the mixture of nanocubes and nanoplatelets, nanocubes were cleanly isolated by precipitating nanoplatelets via gentle centrifugation. The corresponding TEM images and X-ray diffraction patterns are shown in figure 29. Table 4 summarizes the wavelength of the bandedge absorption (λ_{BE}), average NC size, total luminescence quantum yield (QY_{tot}), Mn luminescence quantum yield (QY_{Mn}) and Mn luminescence lifetime (τ_{Mn}) of the three different Mn-doped $CsPbBr_3$ nanocubes. The blueshift of λ_{BE} in the absorption spectra by 20 nm between 0 and 100 μL of HBr results from the relatively high doping concentration that can modify the bandgap of the host via lattice distortion not from the quantum confinement, which has also been recently observed in the cation-exchanged $CsPbBr_3$ NCs[19]. Upon further increasing the amount of HBr to 200 μL, a small additional blueshift of λ_{BE} is observed possibly due to the combination of the further increase in Mn doping and weak quantum confinement from the reduction in the NC size to 6.5 nm.[15]

In figure 28b, the Mn luminescence at 595 nm in Mn-doped $CsPbBr_3$ nanocubes occurs through the energy transfer from the exciton to Mn^{2+} ions doped within the lattice of the perovskite

host.[51, 74] As the amount of HBr increases, the intensity of Mn luminescence increases at the expense of the intensity of bandedge luminescence of the host. The nearly constant total luminescence quantum yields (QY_{tot}) and increasing Mn luminescence quantum yield (QY_{Mn}) with increasing HBr indicates the more efficient energy transfer from the exciton to Mn^{2+} reflecting the higher doping concentration. The Mn doping concentration determined from the elemental analysis employing inductively coupled plasma mass spectrometry (ICP-MS) and TEM EDX was in 3-15 % range, while there is several % of uncertainty due to the common issue of the incomplete removal of all the unreacted Mn^{2+} during the purification of $CsPbX_3$ NCs.[51] Figure 28c shows the time-dependent Mn luminescence intensity, from which the average Mn luminescence lifetime (τ_{Mn}) was obtained. While τ_{Mn} is comparable for 100 and 200 μL HBr, it is much shorter for 0 μL HBr. This may be due to the doping on the surface rather than the interior of the nanocrystals.[65] Compared to the case of Mn-doped $CsPbCl_3$ with τ_{Mn} of up to 1.8 ms,[155] τ_{Mn} is significantly shorter in $CsPbBr_3$ host (~270 μs), likely due to the stronger spin-orbit coupling with the heaver anion analogous to the case of Mn-doped II-VI NCs[156]. The same trend was also observed in bulk $CsMnCl_3$ and $CsMnBr_3$ exhibiting τ_{Mn} of 110 μs and 10 μs respectively.[141] The XRD patterns of Mn-doped $CsPbBr_3$ nanocubes in figure 29d show some changes in the crystal structure upon doping of Mn^{2+} ions in $CsPbBr_3$ host. In particular, the intensities of the peaks at 15.3°, 30.8° and 34.7° decreased significantly compared to undoped $CsPbBr_3$ NCs. This may be due to the relatively high doping concentration that may have distorted the lattice of the host nanocubes. Further structural characterization at the atomic detail will be needed to obtain the deeper understanding of the effect of Mn doping on the crystal structure at this relatively high doping level in $CsPbBr_3$ host.

As mentioned earlier, the Mn luminescence intensity of Mn-doped $CsPbBr_3$ reflecting the doping level strongly correlates with that of $L_2[Pb_{1-x}Mn_x]Br_4$ produced as the intermediate structure, despite the fact that the same amount of $MnBr_2$ is used in all syntheses. This suggests the possibility of $L_2[Pb_{1-x}Mn_x]Br_4$ playing the role of the 'structural precursor', which already contains Mn^{2+} coordinated by six Br^- ions that is necessary to form Mn-doped $CsPbBr_3$ NCs. It is interesting that the formation of the monolayer intermediate structure is distinctly different from the case of Mn-doped $CsPbCl_3$ NCs. In hot-injection synthesis of Mn-doped $CsPbCl_3$ NCs under the condition similar to Mn-doped $CsPbBr_3$ NCs, the equivalent intermediate monolayer structure (i.e., $L_2[Pb_{1-x}Mn_x]Cl_4$) was neither identified (Figure 30) nor necessary for obtaining Mn-doped $CsPbCl_3$ NCs.

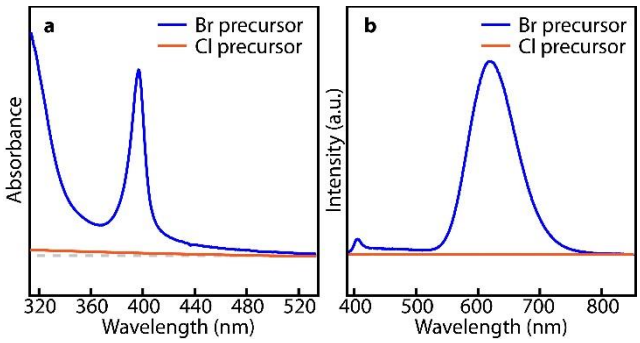

Figure 30. Comparison of the optical spectra of the intermediate product before the injection of Cs-oleate for the synthesis of Mn-doped $CsPbCl_3$ and $CsPbBr_3$ nanocrystals. (a) Absorption and (b) PL spectra under 320 nm excitation from Xe lamp. If $L_2[Pb_{1-x}Mn_x]Cl_4$ is formed as an intermediate species, we anticipate the absorption peak appear near 334 nm[153] and luminescence from Mn, which are completely absent in the case of the synthesis of Mn-doped $CsPbCl_3$ nanocrystals.

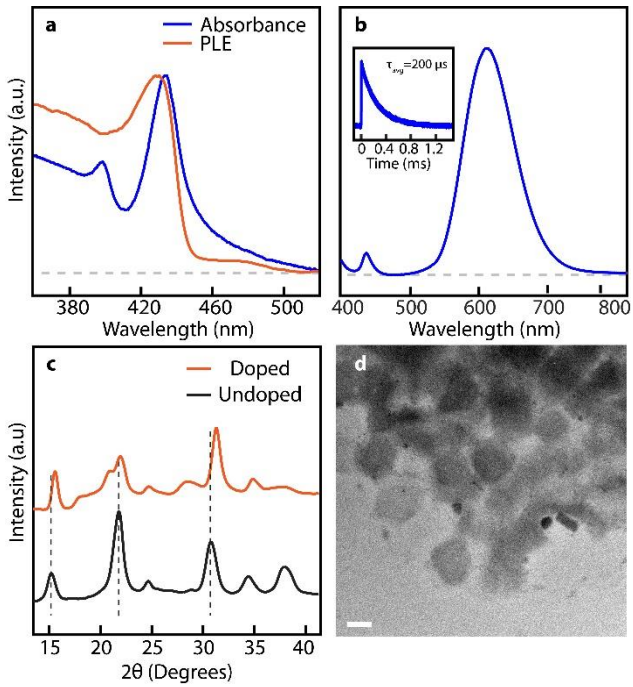

Figure 31. (a) Absorption and PLE spectra, (b) PL spectrum, (c) XRD pattern, (d) TEM image of Mn-doped $CsPbBr_3$ nanoplatelets. Scale bar in (d) is 100 nm. XRD pattern of undoped nanocubes is shown for comparison in (c).

Figure 31a,b show the absorption, PLE and PL spectra of the Mn-doped nanoplatelets recovered from the precipitates in the mixture of Mn-doped $CsPbBr_3$ NCs obtained as the final product when 200 µL of HBr was used. The XRD pattern and TEM of the Mn-doped nanoplatelets are shown in figure 31c,d respectively. The absorption spectrum has a prominent peak at ~430 nm, which is similar to the previously reported absorption spectrum of undoped $CsPbBr_3$ nanoplatelets containing three units of $PbBr_6$ octahedra in the thickness corresponding to ~2 nm.[22, 33] The significantly more blushifted λ_{BE} compared to the nanocubes is due to the 1-dimensional quantum confinement in nanoplatelets. A smaller peak near 395 nm is from the remaining monolayer intermediate structure. PL spectrum shown in figure 31b is dominated by Mn luminescence appearing at 610 nm, while the bandedge luminescence from the host appearing at ~440 nm is much weaker than in Mn-doped nanocubes. The Mn luminescence lifetime obtained from the time-

dependent PL measurement (inset of Figure 31b) is 200 μs. The PLE spectrum detected at 610 nm, while somewhat distorted due to the turbidity of the sample solution, also shows the peak near the absorption peak of the nanoplatelets. This indicates that Mn luminescence in nanoplatelets also results from the exciton-to-Mn energy transfer as in Mn-doped nanocubes. The dominant Mn luminescence in nanoplatelets, in contrast to the nanocubes with significant bandedge luminescence of the host, may be partially due to the strong quantum confinement of exciton that enhances the rate of the energy transfer by increasing the exchange coupling mediating the energy transfer.[74] Considering that many useful properties of Mn-doped semiconductor NCs results from the exchange coupling of the exciton and *d* electrons of the doped Mn^{2+} ions, thin nanoplatelets can potentially be the superior host to nanocubes in providing the stronger coupling between exciton and dopant ions.

4.4 Conclusion

We report the direct hot-injection synthesis method for effectively doping Mn^{2+} ions in $CsPbBr_3$ NCs, which has been difficult to achieve in contrast to Mn doping in $CsPbCl_3$ NCs. In the new approach reported here, the formation of monolayer $L_2[Pb_{1-x}Mn_x]Br_4$ exhibiting strong Mn luminescence before injecting Cs precursor is considered to be the crucial intermediate species leading to the production of the final Mn-doped $CsPbBr_3$ NCs. A strong correlation was observed between the Mn luminescence intensities of $L_2[Pb_{1-x}Mn_x]Br_4$ and the final Mn-doped $CsPbBr_3$ NCs indicating the importance of $L_2[Pb_{1-x}Mn_x]Br_4$ for the successful doping of Mn^{2+} in $CsPbBr_3$ NC host. This suggests that $L_2[Pb_{1-x}Mn_x]Br_4$ already containing the same Mn-Br coordination in Mn-doped $CsPbBr_3$ NCs may have facilitated the formation of Mn-doped $CsPbBr_3$ NCs by providing the structural precursor. This strongly contrasts to the case of Mn-doped $CsPbCl_3$ NCs, where the intermediate structure was neither observed nor necessary for the successful Mn doping.

It is also notable that not only usual nanocubes but also thin nanoplatelets of Mn-doped $CsPbBr_3$ NCs with significantly different quantum confinement can be obtained, offering an opportunity to explore the varying exciton-Mn coupling affected by the quantum confinement in future studies.

CHAPTER V

PHOTOINDUCED ANION EXCHANGE IN CESIUM LEAD HALIDE PEROVSKITE NANOCRYSTALS[††]

5.1 Introduction

The ability of colloidal $CsPbX_3$ perovskite NCs to undergo rapid anion exchange reactions in solution phase has opened the doors to many interesting applications of these materials. A broad range of tunable photoluminescence (PL) from $CsPbX_3$ NCs could be obtained via a simple post-synthesis procedure, where mixing the solution of NCs with the reactive anion precursors results in the formation of the anion-exchanged NCs with tunable bandgap[15, 17, 18] for perovskite nanostructures of various morphologies.[22, 33, 157] The labile nature of the halide anions in the perovskite system is generally accepted responsible for their facile exchange in perovskite NCs and other processes involving ion transport, such as long-range anion diffusion under weak perturbation[158, 159] and the phase segregation in the methylammonium lead mixed halide system.[160] Several recent studies investigated methylammonium lead iodide/bromide films and $CsPbX_3$ colloidal solutions to understand the nature of anion transport and exchange of halide ions in perovskites of various phases.[31, 161] Due to the simple and wide tunability of the photophysical properties of perovskite NCs, anion exchange has been extensively explored using various sources of anions for different applications. [132, 162] In most of these cases, the precursors possessed high

[††] Reprinted with permission from Parobek, David.; Dong, Yitong.; Qiao, Tian.; Rossi, Daniel.; Son, Dong Hee. hotoinduced Anion Exchange in Cesium Lead Halide Perovskite Nanocrystals" *J. Am. Chem. Soc.*, **2017**. *139(12)*, 4358.

reactivity to undergo spontaneous anion exchange reaction upon contact with the NCs and the extent of reaction was usually controlled by stoichiometrically limiting the reactant.

In this work, we report the photoinduced anion exchange in solution of $CsPbX_3$ (X=Cl, Br) NCs suspended in dihalomethane, where the extent of the anion exchange reaction and its rate are controlled by the intensity or wavelength of light without using any reactive sources of halide. In our study, dihalomethane molecules that normally function as the unreactive solvent produce halide ions via photoinduced electron transfer from $CsPbX_3$ NCs resulting in reductive dissociation of the solvent molecules. The halide ions generated in-situ near the surface of NCs drive the anion exchange reaction efficiently, as long as the $CsPbX_3$ NCs are photoexcited above the bandgap. The proposed mechanism of the photoinduced anion exchange in $CsPbX_3$ NCs is illustrated in Scheme 4. The photoinduced anion exchange in $CsPbX_3$ NCs can give a unique capability not available from the earlier anion exchange reactions, such as spatial patterning with controllable stoichiometry.

Scheme 4. Illustration of the proposed mechanism for photoinduced anion exchange of perovskite nanocrystals.

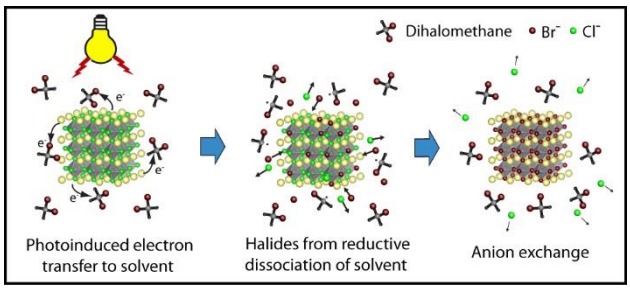

5.2. Experimental Section

5.2.1 Synthesis of $CsPbCl_3$ and $CsPbBr_3$ Perovskite Nanocrystals

Cs-oleate was synthesized by adding Cs_2CO_3 (0.234 g), OA (0.75 g), and ODE (7.04 g) to a 50-mL 3 neck round bottom flask and was evacuated and refilled with N_2 3 times before being heated to 150 °C for at least 10 minutes before using. The $CsPbCl_3$ and $CsPbBr_3$ were synthesized in the following way. $PbCl_2$ (0.0661 g) or $PbBr_2$ (0.0741 g), OAm (0.8 mL), OA (0.8 mL), and ODE (5 mL) were added to a 25-mL 3 neck round bottom flask. The solution was evacuated and refilled with N_2 followed by heating to 120 °C for 30 minutes. The solution was then increased to 165 °C and then 200 °C for 10 minutes each where at 200 °C, dried OAm (0.8 mL) and dried OA (0.8 mL) were consecutively injected to solubilize the solution. Then the Cs-oleate (0.4 mL) was injected and after 1 minute the solution was cooled with an ice bath. The NCs were precipitated with acetone and then centrifuged followed by dissolving in hexanes.

5.2.2 Synthesis of CdSSe/ZnS Quantum Dot

The core shell quantum dot nanocrystals were synthesized following a previously reported method.[48] The CdSSe core was synthesized by first injecting a TBP-selenium solution (0.3 mL, 29 M) into an ODE-sulfur solution (0.25 M). Then 2 mL of the mixture was injected into a solution of CdO (128 mg), ODE (12 mL) and OA (2.02g) at 250 °C under N_2 protection where the reaction proceeded at 240 °C for 1 minute until it was quenched. The nanocrystals were precipitated with acetone, centrifuged, and dispersed in toluene followed by additional cleaning with methanol precipitation. The ZnS shell was deposited on the prepared core following the SILAR method. The CdSSe QD was dissolved in an ODE (6 mL) and OAm (2 mL) solution and heated to 220 °C under N_2 protection. Then in successive 10 minute intervals solutions of ODE-sulfur (0.25 M) and ODE-

zinc stearate (0.25 M, ~5% octylamine) were added dropwise. The solution was then quenched and precipitated with acetone and dispersed in toluene followed by further precipitation with methanol.

5.2.3 Anion Exchange Reactions

The anion exchange reactions were conducted with a home built optical setup using a 405 nm diode laser and a 445 nm diode laser with intensities of 21 mW/cm^2. For $CsPbBr_3$ anion exchange a mixture of DCM/hexane (2:1) with 25 µL was used and for $CsPbCl_3$ anion exchange a mixture of DBM/hexane (1:1) with 25 µL of oleylamine was used. All reactions were done under ambient conditions without stirring. Photoluminescence measurements were taken with a fiberoptic-coupled CCD spectrometer (Ocean Optics, QE65pro) with a 365 nm LED excitation source. The absorption measurements were taken with an Ocean Optics USB2000 spectrometer. Control experiments were conducted for $CsPbCl_3$ (Figure 32a) and $CsPbBr_3$ (Figure 32b).

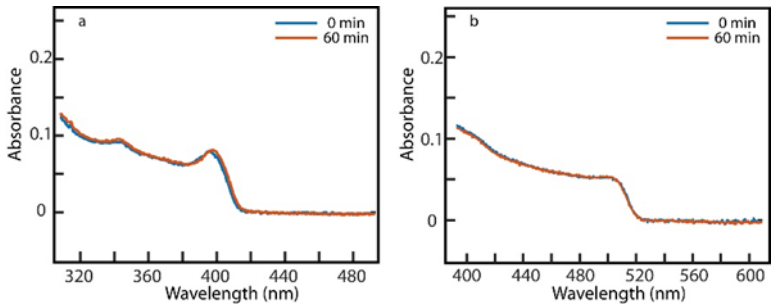

Figure 32. Absence of the anion exchange under dark condition. (a) $CsPbCl_3$ NCs in DBM/hexane, (b) $CsPbBr_3$ NCs in DCM/hexane.

5.2.4 TEM and XRD Before and After Anion Exchange

All TEM images of $CsPbX_3$ NCs were collected using a FEI Tecnai G2 F20 ST FE-TEM microscope operated at 4100 kV.

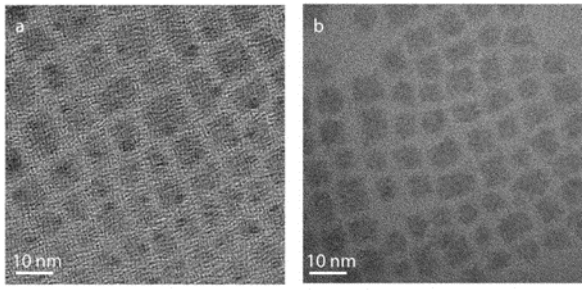

Figure 33. TEM image of NCs before (a) and after (b) the photoinduced anion exchange in DBM/hexane solution under 405 nm excitation.

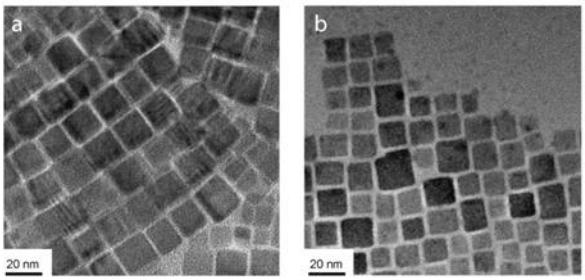

Figure 34. TEM images of $CsPbBr_3$ NCs before a) and after b) the photoinduced anion exchange in DCM/hexane solution under 405 nm excitation.

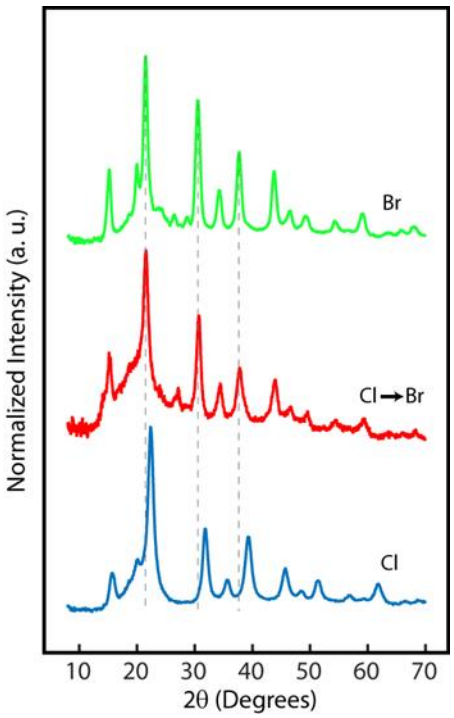

Figure 35. XRD patterns of $CsPbCl_3$ before (blue) and after (red) anion exchange in DBM/hexane solution. XRD pattern of the freshly synthesized $CsPbBr_3$ is shown in green. XRD patterns were obtained using a Bruker-AXS GADDS MWPC diffractometer equipped with Cu K-α x-ray radiation and a multi-wire proportional counter.

5.2.5 Photoinduced Anion Exchange Substrate Patterning

The photopatterning of a substrate was done by first placing $CsPbCl_3$ NCs in a mixture of DBM (5 mL) and polymethylmethacrylate (20 mg) and then dropcasting the solution onto a glass slide. Another slide was used to sandwich the polymer to keep it in place. A 405 nm laser was used to excite the $CsPbCl_3$ and complete the anion exchange in the localized area of the light spot in the viscous reaction medium (Figure 36). The same reaction can be completed starting with $CsPbBr_3$ and using DCM as the solvent for the polymer.

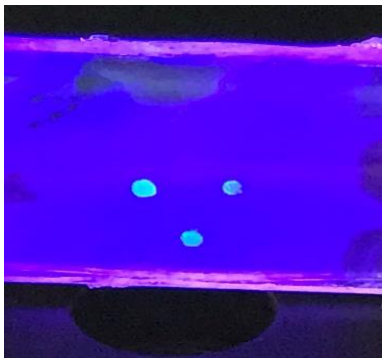

Figure 36. Photoinduced anion exchange of a thin film of $CsPbCl_3$ in a DBM/PMMA matrix to $CsPbBr_3$ with spatial patterning. Three bright dots are the locations where the beam was focused on.

5.3 Results and Discussion

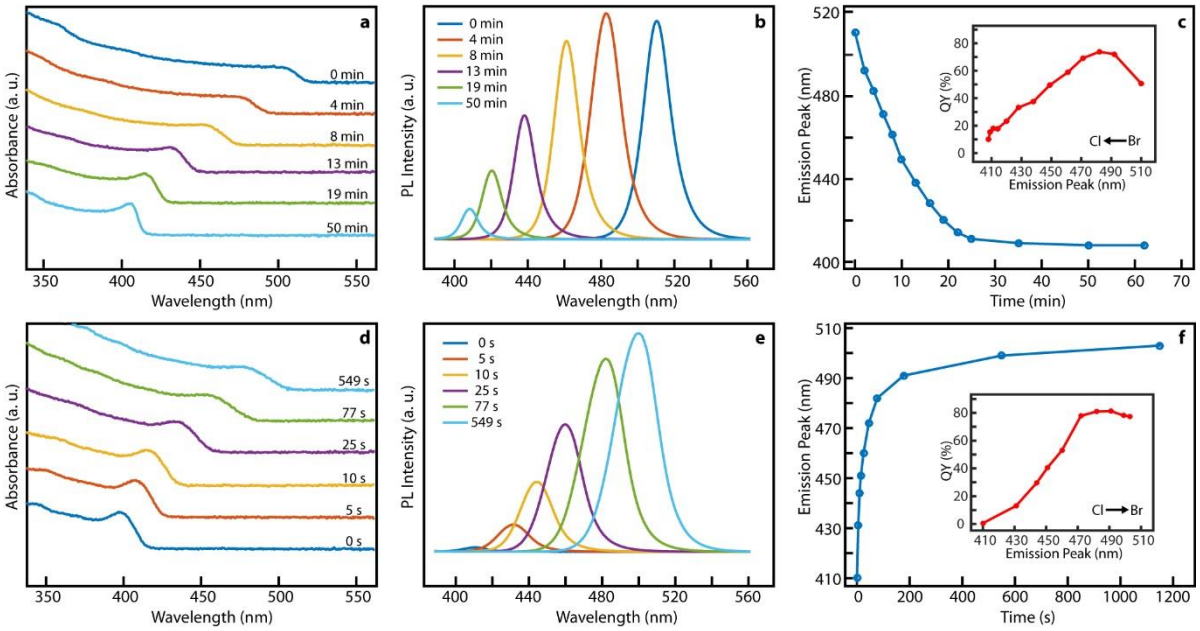

Figure 37. Photoinduced anion exchange of $CsPbX_3$ NCs in dihalomethane solvent. (a,b,c) Time dependence of absorption spectrum (a), PL emission spectrum b), and PL emission peak (c) for $CsPbBr_3 \rightarrow CsPbCl_3$ in DCM/hexane. (d,e,f) Time dependence of absorption spectrum (d), PL emission spectrum (e), and PL emission peak (f) for $CsPbCl_3 \rightarrow CsPbBr_3$ in DBM/hexane.

We demonstrate the photoinduced anion exchange using dichloromethane (DCM) and dibromomethane (DBM) as the inert solvent that also functions as the locally photoactivatable

source of halide anions in the immediate vicinity of the perovskite NCs. $CsPbBr_3$ and $CsPbCl_3$ NCs used in this study were synthesized following a previously reported method[15] with minor modifications. The detailed procedures of $CsPbX_3$ NC synthesis and photoinduced anion exchange reaction, TEM images and X-ray diffraction patterns of the NCs before and after the anion exchange are in the experimental section. Figure 37 summarizes the continuous changes of the absorption and emission spectra during the process of photoinduced anion exchange in $CsPbBr_3$ NCs dispersed in mixed solvent of DCM/hexane (Figure 37 a,b) and $CsPbCl_3$ NCs in DBM/hexane (Figure 37 d,e). The time-trace of the PL emission peak and the PL quantum yield correlated with PL emission peak are also shown for both reactions (Figure 37 c,f). The mixture of hexane and dihalomethane was used as the solvent instead of pure dihalomethane for better solubility of the NCs facilitating more accurate measurement of the optical spectra, while the same photoinduced chemistry can be performed in pure dihalomethane. The entire volume of the solution sample contained in a 1 cm-thick cuvette was illuminated with weak 405 nm light (~20 mW/cm^2) to excite the NCs without stirring the solution.

In the absence of photoexcitation in the dark, the absorption and emission spectra were constant over time, indicating that no anion exchange occurs in the solution of $CsPbCl_3$ and $CsPbBr_3$ NCs in their respective dihalomethane/hexane solvent (Figure 37). Upon illumination with 405 nm light, $CsPbBr_3$ NCs in DCM/hexane showed a blueshift of both absorption and emission spectra indicating the exchange of bromide with chloride. Similarly, $CsPbCl_3$ NCs in DBM/hexane showed a redshift of the spectra from the exchange of chloride with bromide. This indicates that the exchange of anions can occur in both directions and that the direction of the reaction can be varied by changing the solvent composition. The PL quantum yield, shown as insets in Figure 37 c,f, generally decreases with increasing Cl content in $CsPb(Cl/Br)_3$ mixed halide

NCs for the anion exchange reaction in both directions, consistent with earlier observations.[17, 18] In order to confirm that the exchange between the two different halide ions is the direct result of light absorption by perovskite NCs, the progress of the reaction was monitored by changing both the intensity and wavelength of the excitation light. Figure 38a shows the shift of the PL emission peak with alternating 'on' and 'off' periods of the photoexcitation for the anion exchange reaction of $CsPbBr_3$ NCs in DCM/hexane. The shift of the PL emission peak occurs only during the 'on' period, indicating that the extent of reaction can be precisely controlled with photon dose. In addition, the rate of reaction could also be controlled by varying the intensity of light (Fig. 38c), indicating that the rate of production of halide ions via photoexcitation is the main rate limiting step for the overall exchange reaction.

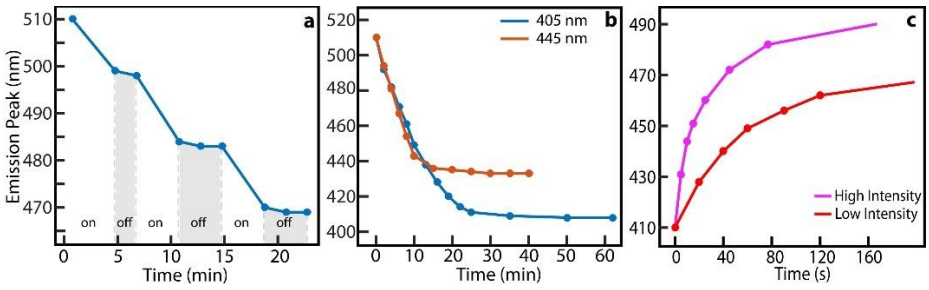

Figure 38. PL emission peak shift for $CsPbBr_3$ in DCM/hexane (a) under 'on' and 'off' period of excitation light (b) under two different excitation wavelengths, 405 and 445 nm. (c) PL emission peak shift from anion exchange of $CsPbCl_3$ in DBM/hexane at two different 405 nm excitation intensities.

The essential role of photoexcitation of the perovskite NCs in anion exchange is further demonstrated in the 'self-limiting' behavior of the reaction when the excitation light becomes off-resonance with the absorption of the perovskite NCs during the exchange process. Figure 38b compares the PL emission peak shift from the anion exchange of $CsPbBr_3$ in DCM/hexane under excitation at 405 and 445 nm. When 445 nm light is used, the reaction stops near the PL emission peak of 440 nm due to the inability of the NCs to absorb light, in contrast to the case of 405 nm

excitation that results in a nearly complete anion exchange. This demonstrates that the extent of reaction can be controlled also with the wavelength of the excitation light in addition to the photon dose. Furthermore, two-photon excitation of the perovskite NCs at 800 nm, where there is no linear absorption in solution, could induce the anion exchange (Figure 39), suggesting an interesting possibility of photo patterning even in 3-dimensions, with an appropriate medium that limits the diffusion of the NCs and solvent. The above observations demonstrate the unique benefits of the photoinduced anion exchange reaction in gaining precise post-synthesis control of the perovskite NCs bandgap.

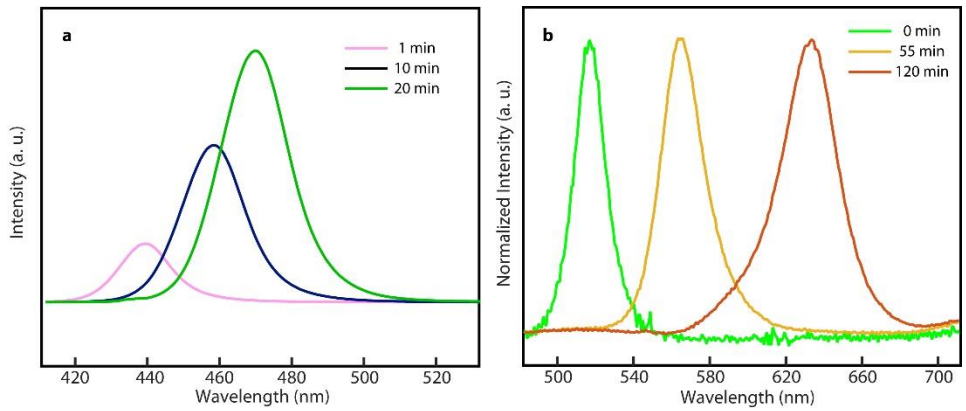

Figure 39. (a) PL emission peak shift from anion exchange of $CsPbCl_3$ in DBM/hexane mixture induced by two-photon excitation at 800 nm from Titanium Sapphire laser. (b) Photoinduced anion exchange from $CsPbBr_3$ to $CsPbI_3$ in diiodomethane/toluene mixture using two-photon excitation.

The possible mechanism for the photoinduced anion exchange reaction is the dissociation of the reduced solvent molecules via interfacial electron transfer from the photoexcited perovskite NCs. Most alkyl halides are known to undergo concerted reductive dissociation into halide ion and alkyl radical under both heterogeneous (e.g., electrochemical) and homogeneous reduction conditions.[163, 164] The reduction potential of various alkyl halides are less negative than -1V vs SCE (saturated calomel electrode) in common organic solvents.[165]

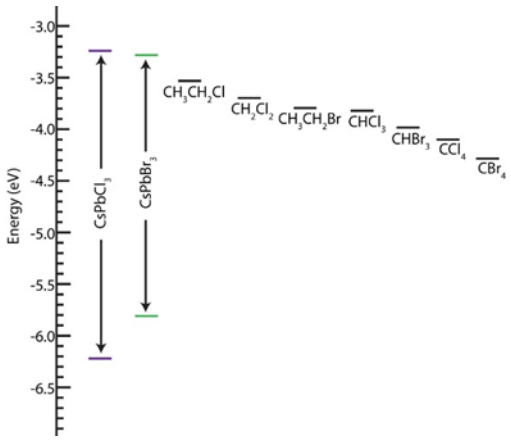

Figure 40. Energy level diagram with respect to vacuum of $CsPbCl_3$ and $CsPbBr_3$ [166] compared to the reduction potential of common halogenated solvents[165].

Therefore, the reduction can be achieved via interfacial electron transfer from the conduction band of $CsPbX_3$ NCs that are energetically located above the reduction potential. For instance, the conduction band edge of $CsPbBr_3$ measured electrochemically[166] and from ultraviolet photoelectron spectroscopy,[167] is 3.35 eV below vacuum level, which is sufficient to reduce DCM that has a reduction potential of -1.04 V vs SCE corresponding to 3.7 eV below vacuum level (Figure 40). From the interfacial electron transfer to solvent molecules, halide ions should be produced in the immediate vicinity of the NCs creating a relatively high local concentration which should facilitate the exchange reaction. This scenario is also corroborated by the observation of the slower reaction rate when the solution is rapidly stirred, which can be attributed to the reduced local concentration of the photogenerated halide ions near the surface of NCs. The holes remaining on NCs should ultimately be removed to continue the reaction and this may involve back electron transfer from remaining halide ions.

For the two anion exchange reactions shown in Figure 37, the absorbance of $CsPbX_3$ NCs at the excitation wavelength and light intensities are comparable. However, the rate of reaction is an order of magnitude faster for $CsPbCl_3$ to $CsPbBr_3$ in DBM/hexane than $CsPbBr_3$ to $CsPbCl_3$ in

DCM/hexane. This may be explained from the combination of the differences in the reduction potential of the solvent molecules and conduction band edge of $CsPbX_3$ NCs rather than photon absorption rate per each NC dictated by the absorption cross section. For alkyl halide molecules, the reduction potential of bromide is less negative than chloride.[165] Furthermore, the conduction band edge of $CsPbCl_3$ is higher than that of $CsPbBr_3$. Therefore, one would expect more facile electron transfer from $CsPbCl_3$ to DBM than from $CsPbBr_3$ to DCM, resulting in a large difference in the rate of halide ion production. In the case of chloromethane series, teterachloromethane showed a faster photoinduced anion exchange reaction than DCM. This may be partially due to the lower reduction potential promoting the faster electron transfer. It is worth to mention that photoinduced anion exchange is less controllable in trihalomethane because of the potentially higher concentration of the reactive contaminants that can be produced under light exposure, resulting in the partial anion exchange even in the absence of light.

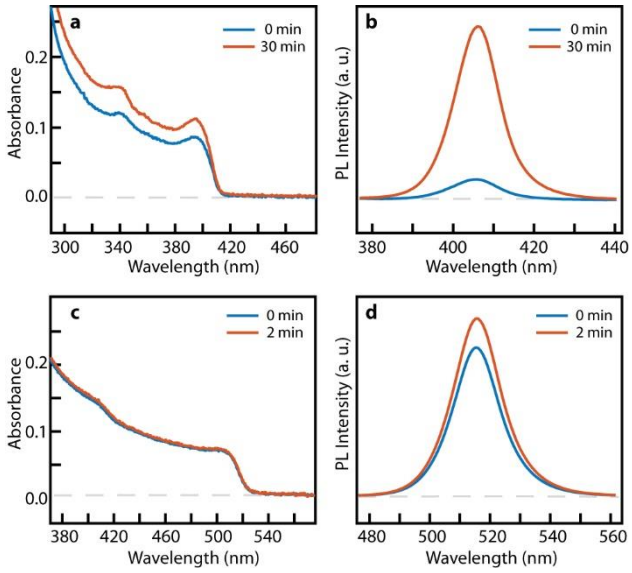

Figure 41. (a,b) Absorption and PL emission spectra before and after excitation of $CsPbCl_3$ NCs in DCM/hexane. (c,d) Absorption and PL emission spectra before and after excitation of $CsPbBr_3$ NCs in DBM/hexane.

When $CsPbBr_3$ and $CsPbCl_3$ NCs are photoexcited in solvent containing their respective halide, i.e., DBM and DCM, there is no net exchange of halides. However, a significant enhancement of PL quantum yield was observed especially in $CsPbCl_3$, typically exhibiting low PL quantum yield (~1%) when freshly synthesized.[18] The absorption and PL emission spectra before and after the photoinduced exchange of the same anion are shown in Figure 41. In the case of $CsPbCl_3$ NCs, the PL quantum yield increases by an order of magnitude (~1%→~10%) accompanied by a substantial increase of the absorption intensity (Figure 41 a,b). In the case of $CsPbBr_3$ NCs that already exhibit 60-80% PL quantum yield when freshly synthesized, the increase of PL quantum yield is ~10% with negligible change in the absorption intensity (Figure 41 c,d). This observation suggests one possible origin of particularly low PL quantum yield in $CsPbCl_3$ NCs and the potential role of photoinduced 'self-anion exchange'. The lower PL quantum yield of $CsPbCl_3$ compared to $CsPbBr_3$ could occur from the relatively high concentration of halide vacancies which could be removed through photoinduced self-anion exchange. The increase of the absorption intensity may reflect the filling of vacancies that increases the density of states involved in the optical absorption. Further confirmation of the above hypothesis will require additional work on the measurement of the optical absorption cross section and accurate elemental analysis.

In a separate experiment, we tested whether the anion exchange reaction can be performed without directly exciting the perovskite NCs by using a separate species that can transfer the electron to the solvent molecules. For this purpose, we examined the anion exchange reaction in the mixture of $CsPbCl_3$ NCs and CdSSe/ZnS core/shell quantum dots dispersed in DBM/hexane under 445 nm excitation, where only CdSSe/ZnS quantum dots absorb light. Figure 42 compares the result from this measurement with that from the reaction of $CsPbCl_3$ NCs under 405 nm

excitation, where the average photon absorption rates in the two sample solutions were kept similar. As expected, the mixture of $CsPbCl_3$ NCs and CdSSe/ZnS can also undergo anion exchange reaction, although the rate is slower likely due to the lower local anion concentration near the surface of the perovskite NCs.

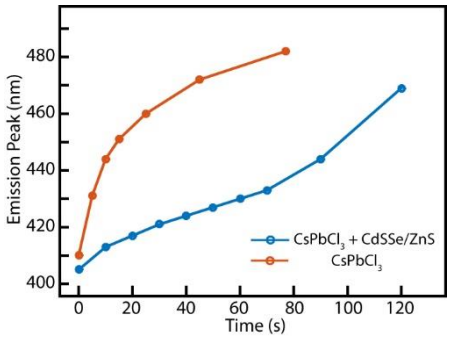

Figure 42. Comparison of the photoinduced anion exchange reactions occurring from the excitation of $CsPbCl_3$ NCs (orange curve) and excitation of CdSSe/ZnS quantum dots (blue curve) in the mixture of $CsPbCl_3$ NCs and CdSSe/ZnS quantum dots.

5.4 Conclusion

In summary, we have shown a highly controllable method of anion exchange using light as the triggering mechanism in the solution of $CsPbX_3$ NCs dispersed in dihalomethane. In-situ production of halide anions via reductive dissociation of the solvent molecules following the interfacial electron transfer from the photoexcited $CsPbX_3$ NCs is considered as the mechanism for the photoinduced anion exchange. We were able to control the extent of anion exchange reaction precisely by controlling either photon dose or wavelength of the excitation light. Multiphoton excitation was also able to induce the anion exchange, creating the potential use for photo patterning in a viscous medium. The self-exchange of the same anions, particularly in $CsPbCl_3$ NCs, resulted in an order of magnitude increase of the PL quantum yield, which may have resulted from the removal of the anion vacancy. The high level of control of the rate and

extent of anion exchange reaction and the potential to spatially pattern the chemical transformation with light will be valuable for the post-synthesis modification of perovskite NCs for various applications.

CHAPTER VI

BREAKING THE SHORT-RANGE PROXIMITY REQUIRENTS IN QUANUTUM DOT/MOLECULAR CATALYST HYBRIDS FOR CO_2 REDUCTION VIA LONG-RANGE HOT ELECTRON SENSITIZATION[‡‡]

6.1 Introduction

Hybrid photocatalytic systems, constructed from a photosensitizing unit (PU) and a catalyst, have been extensively studied for homogeneous photocatalytic conversions of energy relevant small molecules to generate hydrogen (H_2) and reduction products of carbon dioxide (CO_2).[120] For the homogeneous light-driven reduction of CO_2, hybrid systems employing molecular catalysts, such as Ni(cyclam) and Fe(porphyrin),[125, 168, 169] have been studied in combination with either molecular photosensitizers, like $Ru(bpy)_3^{2+}$ and $Ir(ppy)_3$,[170] as well as semiconductor quantum dots (QDs).[116, 122, 124, 125, 171]

In contrast to utilizing molecular photosensitizers, QD/molecular catalyst hybrid systems take advantage of the comparatively higher photostability and larger absorption cross section of QDs for photosensitization, thereby "powering" the molecular catalyst for precise and selective catalytic reactions more effectively. However, all two-component photocatalytic systems require, at least temporarily, proximity between the PU (in its excited or reduced state) and the catalysts molecules (pre-catalysts and all catalyst intermediates) for productive electron transfer to be possible. One route to overcoming this inherent limitation, is the use of synthetic chemistry to link

[‡‡] Reprinted with permission from Parobek, David.; Meeder, Jeremy.; Pounthenpurayil, Joseph.; Nippe, Michael.; Son, Dong Hee. Breaking the Short-Range Proximity Requirement in Quantum Dot/Molecular Catalyst Hybrids for CO2 Reduction via Long-Range Hot Electron Sensitization **2020**.

both components together. Examples of this approach include the covalent attachment of catalysts to the PU,[172] as well as the utilization of supramolecular interactions, such as van der Waals interaction,[173] hydrogen bonding,[174] and ion pairing.[123] For example, in a report by Weiss et al. it was shown that ion pairing between anionically terminated II-VI QDs and synthetically modified, highly cationic Fe(porphyrin) catalysts, allowed for a significant increase in CO_2 conversion to carbon monoxide (CO).[123]

Scheme 5. Potential CO generation pathways for doped (left) and undoped (right) QDs in QD/catalyst systems.

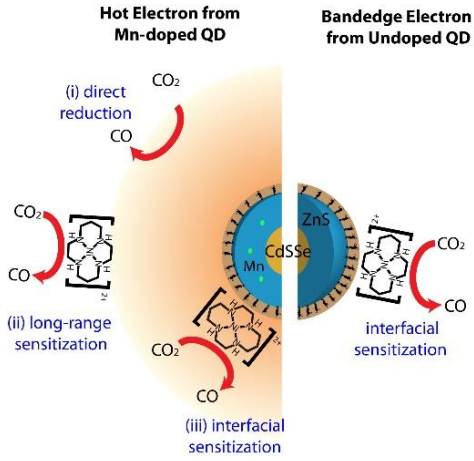

Although these approaches are certainly promising, they add complexity, require additional synthetic steps, may not be applicable to a large variety of catalysts, and given the sensitivity of molecular catalysts performance to ligand design, may not allow to tune catalyst and PU independently from each other. We propose that the burden of linking QDs and molecular catalyst can potentially be alleviated by using hot electrons which would enable long-range electron transfer for sensitization of molecular catalysts that are separated far from the QDs. Since hot electrons can transfer across a thick and high-energy barrier, QD sensitizer and molecular catalyst do not necessarily need to be linked as tightly in space. Recently, the generation of hot electrons with excess kinetic energies of more than 2 eV above the conduction bandedge was demonstrated

via exciton-to-hot electron 'upconversion' under weak visible excitation conditions in Mn-doped II-VI QDs.[175-177] The exciton-to-hot electron upconversion is achieved through a sequential two-photon process, mediated by the long-lived excited ligand field state of Mn^{2+} as the intermediate state that adds excess energy to the electrons in the conduction band. These hot electrons can transfer across a 7 nm-thick insulating Al_2O_3 layer in an electrochemical cell platform,[110] and even create photoelectron emission current under vacuum condition,[112] demonstrating their ability to travel long distances over the high energy barrier. Therefore, hot electrons generated in Mn-doped QDs are expected to overcome the shortcomings of short-range interfacial electron transfer of bandedge electrons that limits the spatial extent of catalytic reactions to the immediate proximity of the QD surface. Compared to plasmonic hot electrons in metal nanostructures, the absolute energy of hot electrons from upconversion is several eV higher.[112] The advantage of these hot electrons in QD-based photocatalysis was recently demonstrated for photocatalytic H_2 production with Mn-doped QDs in the absence of a molecular catalyst or other cocatalyst.[33]

Building on these results, the present study establishes the feasibility of using hot electrons for long-range sensitization of molecular catalysts in "non-linked" QD/molecular catalyst hybrid systems. We show that for simple QD/molecular catalyst (precatalyst is $[Ni(cyclam)]^{2+}$) mixtures, both CO_2 to CO conversion (under a CO_2 atmosphere) and H_2 production (under an Ar atmosphere) are strongly enhanced if Mn-doped QDs are employed as the PUs as compared to those using undoped QDs (Scheme 5). The comparison of CO production rates of Mn-doped QD/$[Ni(cyclam)]^{2+}$ and undoped QD/$[Ni(cyclam)]^{2+}$ systems strongly suggests that long-range hot electron sensitization is indeed possible, resulting in a 6-fold increase in the production of CO from CO_2 of the former under otherwise identical conditions. The results from this study clearly demonstrate the benefits of hot electron sensitization in non-linked hybrid systems, which will

greatly simplify the design and construction of hybrid photocatalysts by eliminating the need for linkages between PUs and molecular catalysts.

6.2 Experimental Section

6.2.1 Synthesis of [Ni(cyclam)](BF4)2

The [Ni(cyclam)](BF4)2 was synthesized following a previously reported method.[178] Ni(II) tetrafluoroborate hexahydrate(0.8306 g) was dissolved in 40 mL of 30 °C ethanol. This solution was then added to a solution of cyclam (0.5000 g) dissolved in 20 mL of 30 °C ethanol. The resulting orange solid was filtered off, washed with cold ethanol, and allowed to dry overnight.

6.2.2 QD Synthesis

Mn-doped and undoped CdSSe/ZnS core/shell quantum dots (QDs) were synthesized following procedures published previously.[179, 180] The sulfur/selenium (S/Se) precursor was prepared by adding 0.5 mL of a 1 M tributylphosphine (TBP) solution of selenium to a mixture of 10 mL of heated octadecene (ODE) and sulfur (0.081 g). Subsequently, 2 mL of S/Se precursor solution was swiftly injected to a solution of ODE (12 mL) with CdO (0.128 g) and oleic acid (2.1 mL) heated to 250 °C. After the injection, the reaction temperature was reduced to 240 °C and allowed to proceed for 70 seconds, which produced CdSSe core QDs. After quenching the reaction by rapid cooling of the reactant mixture, the produced QDs were precipitated by adding acetone and centrifugation. The precipitated CdSSe core QDs were recovered and dispersed in toluene. Three more cycles of precipitation/redispersion were applied to further purify the QDs before coating ZnS shell.

Shell coating and Mn doping were performed following the previously reported procedure employing successive ionic layer adsorption and reaction (SILAR) method. The core QDs were initially dissolved in a mixture of ODE (6 mL) and oleylamine (2 mL) and heated up to 220 °C under N2. Subsequently, the mixture of ODE-sulfur (0.25 M) and the zinc precursor solution (0.25 M zinc stearate in toluene with 5 % octylamine) were added dropwise to the core QD solution over 10 minutes. After adding two layers of ZnS shell, the 'intermediate' core/shell QDs were precipitated and purified following the same procedure of purifying the core QDs.

The purified 'intermediate' core/shell QDs were dispersed in the mixture of ODE (6 mL) and oleylamine (2 mL) and heated up to 260 °C for Mn-doping. Mn-doping was performed by adding ODE-sulfur solution and a solution of Mn(OAc)2 (0.029 g) in oleylamine (6 mL) dropwise then cooling after 20 minutes. Subsequently, the Mn-doped QDs were purified using the same procedure described above and 4 additional ZnS shell layers were coated. The final Mn-doped CdSSe/Zn core/shell QDs were recovered and purified by applying multiple precipitation/redispersion cycles using methanol and toluene as anti-solvent and solvent. The final doping concentration calculated from ICP elemental analysis was 4.7%. For the undoped QDs the same procedure was followed excluding the Mn-doping step.

The resulting QDs (both Mn-doped and undoped core/shell QDs), initially passivated with oleylamine and dispersible in nonpolar solvent underwent ligand exchange with 4-mercaptopropionic acid (MPA) to make them water soluble. To the QDs dispersed in chloroform the mixture of water (0.200 mL), methanol (0.800 mL) and MPA (0.100 mL) was added. The pH of solution was maintained at >8 by adding small amount of NaOH. After stirring the mixture for 3 hours, the ligand-exchanged QDs in the organic phase had transferred to the aqueous phase.

After separating the aqueous phase, the QDs were isolated by precipitating with acetone to remove any unbound MPA. The recovered QDs were dispersed in water before use.

6.2.3 Calculation of Extinction Coefficient and QD Concentration

The extinction coefficient of the QDs and concentration of QDs in the solution were obtained in the following ways from the size of the QDs estimated from the TEM images and total metal ion concentration of the QDs solution sample determined from the elemental analysis. The total concentration of metal ions (Cd2+ and Zn2+) in the acid-digested QD samples were determined from employing inductively coupled plasma mass spectrometry (NexIon 300D). The sample for the elemental analysis was prepared by first drying 1 mL of QD solution with absorbance of 0.1 at 460 nm and then digesting the dried QD sample in concentrated nitric acid. The calibration curve for the elemental analysis was built by measuring the various diluted element standard ICP solutions (Aldrich). The concentration of Cd2+ and Mn2+ ([Cd2+] and [Mn2+]) of each sample could be calculated to determine the absorption coefficient. The molar extinction coefficient (ε) was calculated using Beer's law:

$$\varepsilon = \frac{A}{(b*[QD])} \tag{11}$$

Where A is the absorbance of the sample, b is 1 cm, and [QD] is the molar concentration of the QDs. [QD] is calculated from [Cd2+]/<nCd>, where <nCd> is the average number of cadmium ions per QD. The number of Cd2+ ions was calculated from the radius of the CdSSe core in the TEM images then used to determine the number of Cd2+ ions per QD (~420). [QD] is then calculated by:

$$[QD] = \frac{[Cd^{2+}]}{420} \tag{12}$$

Resulting in $\varepsilon = 1.93 \times 10^5\ M^{-1}\,cm^{-1}$ at 460 nm.

6.2.4 Quantification of the Photocatalytic Reduction Product (CO and H2)

The quantification of the gaseous photocatalytic reduction products (CO and H2) were performed using a custom-built reactor and gas chromatography (GC) for detection. The cylindrically shaped reactor has the inner diameter of 5 cm with total internal volume of 150 cm3. The total volume of the reactant mixture is 60 mL (54 mL of DI water + 6 mL of triethylamine as the sacrificial hole scavenger). At the concentration of QDs of this study (~20 μM), the absorbance of the QDs at the excitation wavelength (450 nm) is 0.04 in a 1 cm pathlength cuvette. The concentration of [Ni(cyclam)](BF4)2 dissolved in the solution is 3 mM.

The sealed reactor containing all the reactant mixture, as described above, was bubbled with either CO2 (for CO2 reduction) or Ar (for control experiment) for 40 min then placed in a circulated water bath to keep the temperature of the reactor constant at 25 °C. A blue 450 nm LED was used as the excitation source. A 200 μL aliquot of the headspace was taken every 2 hrs (2, 4, 6 and 8 hrs) with a gas tight syringe (Gas Syringe Series A-2 Luer Lock 500 μL RN, VICI precision sampling) for the analysis of the concentration of the product gas. The analysis was performed on a GC with a thermal conductivity detector (for H2 detection) and flame ionization detector equipped with a methanizer (for CO detection). CH4 was used as an internal standard to check the potential variation during the sampling and injection of the aliquots.

The calibration of the detectors for the quantification of CO and H2 was done in the following way after the completion of each experiment. The reactor was first purged with CO2 for 30 minutes to remove all CO, H2, and CH4. This was confirmed by taking a 200 μL aliquot of the headspace and injecting it into the GC for the analysis. The reactor was injected with the internal standard (200 μL CH4) and known amount of CO and H2, and allowed to equilibrate with the

reactant mixture for 15 minutes. Subsequently, a 200 µL aliquot of the headspace was sampled and injected into the GC for the analysis. After adding additional known amount of CO and H2 into the reactor, the sampling of headspace and analysis with GC was continued to complete the full calibration curve. The calibration curve was created from taking the ratio of the integrated areas between the internal standard and generated gases (CO:CH4 and H2:CH4).

6.2.5 Quantum Efficiency Calculation for CO Generation

The quantum efficiency of the CO generation (QE) was calculated from the ratio of the number of CO molecules produced (n_{CO}) and the number of photons absorbed by the quantum dots (n_{ph}). The factor of 2 comes from the number of electrons needed to produce one CO molecule via reduction.

$$QE = 2\frac{n_{CO}}{n_{ph}} \tag{13}$$

n_{ph} for a given illumination time (t) was calculated from the average fraction of photons absorbed by the QDs across the reactor (f = 0.20), the area of illumination (A=15 cm^2) for a given excitation intensity (I =0.1W/cm^2) and photon energy (E_{ph} = 4.41· 10^{-19} J).

$$n_{ph} = (I \times f \times A \times t)/E_{ph} \tag{14}$$

For t =8 hrs (28800 s) and n_{CO}= 6.5µM × 6.02·10^{23}, we get QE of 0.04 %

6.3 Results and Discussion

In this work, we used Mn-doped and undoped CdSSe/ZnS core/shell QDs of the same size and host structure as the source of hot electrons and bandedge electrons,[181] respectively, to examine the capability of hot electrons to perform long-range sensitization of [Ni(cyclam)]$^{2+}$ in a non-linked hybrid photocatalyst system. We chose [Ni(cyclam)]$^{2+}$ as a molecular catalyst as Ni(cyclam)-based catalysts are well known to display good selectivity for CO_2 to CO conversion under electro-[182]

and photocatalytic[125] conditions while also being able to catalyse H_2 production in the absence of CO_2.[183] Figure 43 shows the absorption and photoluminescence (PL) spectra of Mn-doped and undoped QDs as well as their TEM images. Both Mn-doped and undoped QDs have nearly identical absorption spectra and extinction coefficient, ascertaining the same amount of light absorption for a given concentration of QDs in solution (see experimental for details). Exciton PL is centred at 487 nm for both Mn-doped and undoped QDs, while only Mn-doped QDs show PL near 600 nm from $^4T_1 \rightarrow {}^6A_1$ ligand field transitions from Mn excited states. Both, Mn-doped and undoped QDs, exhibit comparable total PL quantum yields of 50-60%.

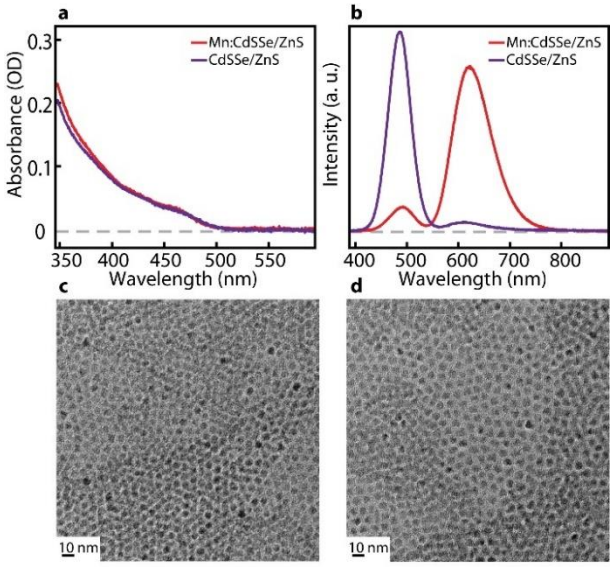

Figure 43 Absorption (a) and PL (b) spectra of Mn-doped (red) and undoped (purple) CdSSe/ZnS QDs before adding TEA and $[Ni(cyclam)]^{2+}$. TEM of Mn-doped (c) and undoped (d) QDs.

In order to assess the capability of hot electrons to perform long-range sensitization of $[Ni(cyclam)]^{2+}$ for CO_2 reduction, we compared the catalytic activity for CO production for four different catalyst systems in CO_2-saturated aqueous media: (i) undoped QD only, (ii) undoped QD/$[Ni(cyclam)]^{2+}$, (iii) Mn-doped QD only, (iv) Mn-doped QD/$[Ni(cyclam)]^{2+}$. For all four systems, the molar concentration of QDs were ~20μM and 0.77M triethylamine (TEA) was used

as the sacrificial hole scavenger (see experimental for details). Solutions in the photocatalytic reactor were illuminated using an LED (450 nm, 0.1 W/cm^2) to excite the QDs near the bandgap (Figure 44a). While [Ni(cyclam)]$^{2+}$ has an absorption at 450 nm (Figure 44b), it does not affect the comparison of the sensitization of non-linked [Ni(cyclam)]$^{2+}$ by hot electrons from Mn-doped QDs and bandedge electrons from undoped QDs.

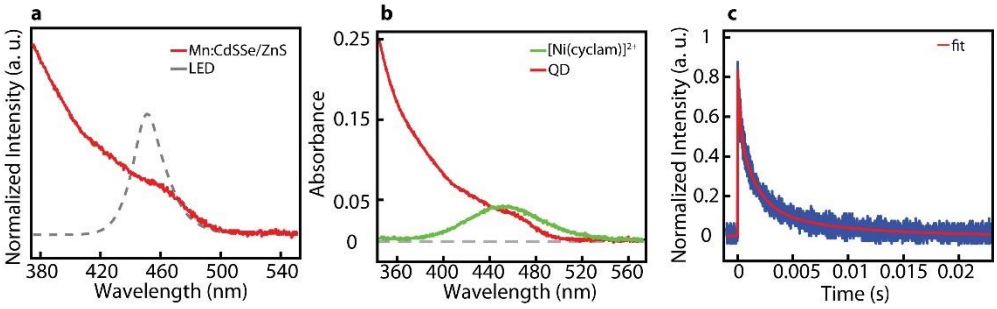

Figure 44. (a) Overlap of excitation light source (450 nm LED) and QD absorption. (b) Absorption of QD and [Ni(cyclam)]$^{2+}$. (c) Time dependent luminescence lifetime of Mn-doped CdSSe/ZnS QD.

Figure 45 shows the amounts of CO and H_2 produced for the four different photocatalyst systems as a function of irradiation time up to 8 hours. Table 5 summarizes the total amount of CO and H_2 produced after 8hrs of reaction and their ratio. In the absence of [Ni(cyclam)]$^{2+}$, undoped QDs did not result in detectable gaseous products with CO and H_2 being below the detection limit. The undoped QD/[Ni(cyclam)]$^{2+}$ system display an increase in the production of both, CO and H_2, with a CO:H_2 ratio of 0.76:1. Given the absence of appreciable amounts of CO in the absence of [Ni(cyclam)]$^{2+}$, CO was likely produced via the short-range sensitization of [Ni(cyclam)]$^{n+}$ by bandedge electrons. In this case, the sensitization can only occur for those [Ni(cyclam)]$^{n+}$ molecules sufficiently close to the surface of the QDs. In contrast to undoped QDs, Mn-doped QDs are able to produce CO even in the absence of [Ni(cyclam)]$^{2+}$ with an activity comparable to that of the undoped QDs/[Ni(cyclam)]$^{2+}$ system. However, the major product under these conditions is H_2, yielding a CO:H_2 product selectivity of 0.07:1.

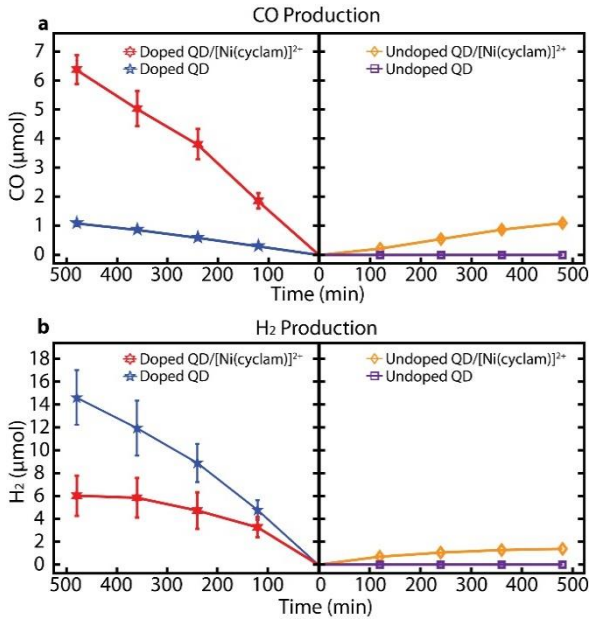

Figure 45. Comparison of photocatalytic CO (a) and H_2 (b) production under a CO_2 atmosphere, using Mn-doped (left) or undoped QDs (right) in the presence or absence of $[Ni(cyclam)]^{2+}$.

Importantly, the efficiency and selectivity for CO production are greatly improved in Mn-doped QD/$[Ni(cyclam)]^{2+}$ system. A 6-fold enhancement for CO production is observed when compared to either undoped QD/$[Ni(cyclam)]^{2+}$ system or Mn-doped QD only. The CO:H_2 ratio of 1.05:1 is favoring the production of CO. These improvements suggest that sensitization of $[Ni(cyclam)]^{2+}$ by hot electrons is ~6 times more efficient than by bandedge electrons if the small contribution from the direct reduction of CO_2 to CO by Mn-doped QDs is ignored. The increase in efficiency of the sensitization by hot electrons is the combined result of the enhanced electron transfer rate to $[Ni(cyclam)]^{2+}$ at a given distance and the longer electron transfer distance of hot electrons. In a simplified picture, one may view the enhancement of sensitization as the larger spatial extent of sensitization by hot electrons giving access to more remotely located molecular catalysts. Several control experiments were carried out to validate our interpretations: *(1)* saturating post-CO_2 reduction solutions with Ar and continuing irradiation did not result in any CO formation for either test system, and confirms that CO production originates solely from the

reduction of CO_2. *(2)* Addition of the nickel salt $Ni(BF_4)_2 \cdot 6H_2O$ instead of $[Ni(cyclam)]^{2+}$ rapidly resulted in a grey precipitate (likely colloidal Ni particles) under irradiation with no detectable formation of CO and H_2, which strongly suggests that the molecular nature of $[Ni(cyclam)]^{n+}$ remains intact during catalysis and it is acting as the active catalyst. (3) Irradiation of $[Ni(cyclam)]^{2+}$ in the absence of either QD did not result in H_2 or CO production.

Table 5. CO and H_2 production by four different catalyst combinations under CO_2 atmosphere after 8 hrs of reaction. [a] below detection limit.

Catalyst combination	**CO (μmol)**	**H_2 (μmol)**	**CO:H_2 ratio**
undoped QD only	0 [a]	0 [a]	-
undoped QD/$[Ni(cyclam)]^{2+}$	1.0	1.3	0.76:1
Mn-doped QD only	1.0	14.6	0.07:1
Mn-doped QD/$[Ni(cyclam)]^{2+}$	6.3	6.0	1.05:1

Quantitative estimations of the enhancement of sensitization by each hot electron is difficult, because of the uncertainty in the quantum efficiency (QE) of hot electron generation from exciton-to-hot electron upconversion. In our earlier study that used Mn-doped QDs for hot electron-driven H_2 production, the upper limit to the QE of generating hot electron was estimated ~20 % for that particular QD structure. This suggests that each hot electron from Mn-doped QDs can be an order of magnitude more efficient in sensitizing unbound $[Ni(cyclam)]^{2+}$ than the bandedge electrons from undoped QDs. In this study, we focus on firm experimental verification of the effectiveness of hot electron sensitization in non-linked hybrid catalyst systems for photocatalytic reduction. Detailed quantitative assessment and optimization of the overall efficiency of photocatalytic reduction via hot electron sensitization, dictated by the hot electron

generation efficiency of the QD itself and other environmental variables will be addressed in future studies.

Although the presented results are obtained for not vigorously optimized conditions, we estimate the QE of CO and H_2 production by hot electrons in Mn-doped QD/$[Ni(cyclam)]^{2+}$ (see experimental for details). Assuming that the majority of reaction products are formed through hot electrons, we estimate a QE for CO production to be approximately 0.04 %, with nearly the same QE for H_2 production for the Mn-doped QD/$[Ni(cyclam)]^{2+}$ system under our experimental conditions. This QE is on the same order of magnitude as those for non-linked two component $Ru(bpy)_3^{2+}$/$[Ni(cyclam)]^{2+}$ hybrid systems (0.06%) studied earlier.[184] However, since it is often difficult to make meaningful direct comparisons of QE values between different photocatalytic systems from different studies, we will not put much emphasis on this comparison. Nevertheless, it is informative to compare the enhancement factor (6-fold) of CO production gained by hot electron sensitization in non-linked QD/$[Ni(cyclam)]^{2+}$ system in this study with the reported enhancement factor of CO production obtained by 'linking' undoped QDs and $[Ni(cyclam)]^{2+}$. In a study by Reisner et al., it was shown that the covalent attachment of phosphonic acid-functionalized $[Ni(cyclam)]^{2+}$-derived catalysts to the surface of ZnSe QDs allowed for a 3-fold increase in photocatalytic CO production, as compared "non-linked" ZnSe QD/$[Ni(cyclam)]^{2+}$ mixtures.[125] Although detailed reaction conditions are different between the two hybrid catalyst systems, our results indicate that the net effect of hot electron sensitization in non-linked hybrid catalyst system is similar to that of forming chemical linkage between the sensitizer and molecular catalysts.

Scheme 5 illustrates the differences in the pathways of $[Ni(cyclam)]^{2+}$ sensitization and CO_2 to CO conversion by bandedge electron and hot electrons from undoped and Mn-doped QDs

respectively. Several pathways for CO generation in Mn-doped QD/[Ni(cyclam)]$^{2+}$ systems can be envisioned: (i) The direct reduction of CO_2 to CO by hot electrons without involving the molecular catalyst, (ii) reduction via long-range sensitization of remote [Ni(cyclam)]$^{2+}$, (iii) reduction via interfacial sensitization of [Ni(cyclam)]$^{2+}$ near the QD surface. Pathway (i) accounts for the production of CO from Mn-doped QDs in the absence of [Ni(cyclam)]$^{2+}$. While no detailed mechanism is available, the involvement of solvated electrons, similar to those reported by Hamers et al.,[185] is a possibility, since hot electrons from upconversion possessing >2eV excess energy above the bandedge could be injected into the solvent forming solvated electron. Considering the 6-fold increase in CO production in the presence of [Ni(cyclam)]$^{2+}$, this direct reduction pathway likely has only a minor contribution to the product formation in the hybrid catalyst system. Since non-linked [Ni(cyclam)]$^{2+}$ molecules are distributed with varying distances from the QD surface, both long-range and interfacial sensitization are operating when Mn-doped QDs are used, whereas only interfacial sensitization is possible with undoped QDs. Since undoped QD/[Ni(cyclam)]$^{2+}$ systems are 6 times less active than Mn-doped QD/[Ni(cyclam)]$^{2+}$ for CO production, pathway (iii) should also have minor contributions. Therefore, we conclude that long-range hot electron sensitization is the major pathway accounting for the enhanced CO production in Mn-doped QD/[Ni(cyclam)]$^{2+}$ system.

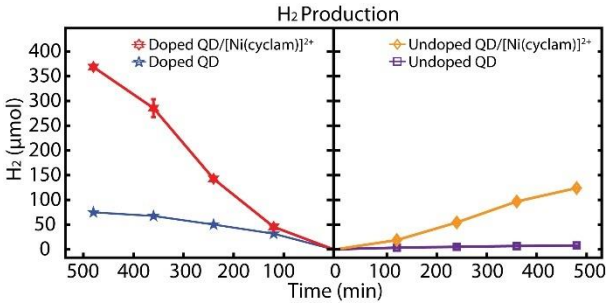

Figure 46. Comparison of photocatalytic activity for H_2 generation under Ar atmosphere using Mn-doped (left) or undoped QDs (right) in the presence or absence of [Ni(cyclam)]$^{2+}$.

To further support our conclusion, we also tested the photocatalytic H_2 production ability of $[Ni(cyclam)]^{2+}$ in the presence of either Mn-doped QDs or undoped QDs under Ar atmosphere. Although $[Ni(cyclam)]^{2+}$ displays good selectivity for CO_2 reduction in various media, it is also known to be a competent catalyst for H_2 evolution in the absence of CO_2.[183] Figure 46 and table 6 compares the amount of H_2 produced for four different QD/catalyst combinations. In agreement with the above results for CO_2 reduction, Mn-doped QD/$[Ni(cyclam)]^{2+}$ system is superior to both Mn-doped QDs in the absence of catalyst and undoped QD/$[Ni(cyclam)]^{2+}$ systems, displaying a 3-5-fold enhancement of producing H_2. This result also indicates that the benefits of long-range hot electron sensitization can be universal and applicable to a wide range of photocatalytic reductions facilitated by non-linked hybrid catalyst systems.

Table 6. H_2 production by four different catalyst combinations under Ar atmosphere after 8hrs of reaction.

Catalyst	CO (μmol @ 8hrs)	H_2 (μmol @ 8hrs)
Undoped QD	below detection limit	7.6
Undoped QD/$[Ni(cyclam)]^{2+}$	below detection limit	123
Mn-doped QD	below detection limit	75
Mn-doped QD/$[Ni(cyclam)]^{2+}$	below detection limit	368

6.4 Conclusion

In this work we showed that hot electron sensitization can be utilized to produce CO from CO_2 with QD/molecular catalyst hybrid systems without requiring a linkage between QDs and molecular catalysts. Mn-doped QDs generating energetic hot electrons could sensitize $[Ni(cyclam)]^{2+}$ in solution via long-range electron transfer, enabling CO_2 reduction. The results reveal a new avenue for the design of hybrid catalyst systems by removing the necessity of linkage and spatial proximity between photosensitizer and molecular catalysts.

CHAPTER VII

SUMMARY

7.1 Mn-doping in $CsPbCl_3$ Perovskite Nanocrystals

Perovskite nanocrystals have provided a new material platform in colloidal semiconductors that show promise in many photovoltaic and optoelectronic applications from their intrinsically high quantum yields. The ionic nature and structure lability also grant easy tunability of the optical properties through exchanging the constituent atoms further increasing the possibility to post synthetically tailor the nanocrystal for a specific application. Transition metal doping of semiconductors nanocrystals has been done for decades to impart new properties from the interaction between the exciton and the metal dopant.

Mn^{2+} ions are heavily studied in II-VI QDs from the interesting new photoluminescent and magnetic properties that it creates in the host structure. In $CsPbCl_3$ and $CsPb(Br_xCl_{1-x})_3$ Mn^{2+} is isoelectronically doped in the B site location of the perovskite replacing Pb^{2+}. The Mn doped $CsPbCl_3$ exhibits bright orange photoluminescence at 600 nm that is sensitized through energy transfer from the host structure. The Mn photoluminescence exhibits lifetimes greater than 1 ms that can fit to a monoexponential function indicating its homogeneous distribution throughout the lattice. Through gel permeation chromatography the nanocrystals were isolated from the crude solution to receive an accurate doping concentration of 0.2% which is corroborated through the well-defined hyperfine splitting seen via electron paramagnetic resonance. The Mn doped nanocubes also show an increase in excitonic emission when Mn is incorporated most likely arising from the inefficient energy transfer to Mn from the weakly confined nature of the host as

well as the increased concentration of Cl^- anion during synthesis, filling defect sites and decreasing nonradiative emission.

7.2 Direct Hot Injection Synthesis of Mn-doped $CsPbBr_3$ Nanocubes and Nanoplatelets

$CsPbBr_3$ nanocrystals are the hallmark system of the halide perovskites with intrinsic quantum yields greater than 80% and multiple post synthetic methods to achieve unity. They also have greater absorption cross sections in the visible absorbing up to 510 nm where $CsPbCl_3$ only absorbs up to 400 nm. This gives it a greater potential for uses in applications that rely on solar energy. Mn doping in $CsPbBr_3$ had eluded researchers for years after the method for synthesizing $CsPbCl_3$ was developed due to the unfavorable thermodynamic disparity between $MnBr_2$ and $PbBr_2$ bond strength. The incorporation of hydrobromic acid resulted in a Mn doped monolayer intermediate forming which facilitated the generation of $CsPbBr_3$ nanocubes and nanoplatelets.

The formation of $L_2[Pb_xMn_{1-x}]Br_4$ (L=oleylamine) was verified through the appearance of periodic peaks in the XRD pattern from the stacking of monolayers as well as the observation of a sharp excitonic absorption which the Mn emission at 600 nm was sensitized to. The Mn emission in the $CsPbBr_3$ nanocubes increased from 1% to 30% with the increasing amount of hydrobromic acid (0-200 μL). The absorption showed a 20 nm blueshift which is from a combination of confinement effects from the decreasing size of the nanocrystal (8.2 nm to 6.5 nm) and the incorporation of Mn which results in the shortening of Pb-Br bond length form the decreased size in ionic radius. The contraction of the lattice is also shown from the increase in 2θ from the XRD pattern. Mn doped nanoplatelets were also generated and separated from the nanocubes from their large lateral dimensions (> 100 nm) making them insoluble. They also exhibited strong Mn

luminescence sensitized to the host with the excitonic emission being quenched due to the greater extent of the confinement.

7.3 Photoinduced Anion Exchange of $CsPbX_3$ Perovskite Nanocrystals

Anion exchange in $CsPbX_3$ perovskite nanocrystals creates the opportunity to tune the photoluminescence throughout the visible from 400 nm for Cl containing perovskite to 700 nm for I. Most methods consisted of injecting a halide containing salt that will result in the fast exchange causing an immediate color change. This can be difficult to control if a certain wavelength is the target since the amount of the halide would have to been tuned each time. We developed an alternative method that relies on the use of light as the trigger to initiate the anion exchange of the perovskite in a halogenated solvent.

Photoinduced anion exchange was shown for $CsPbCl_3$ to $CsPbBr_3$ ($CsPbBr_3$ to $CsPbCl_3$) in a dibromomethane:hexane (dichloromethane:hexane) mixture under weak laser excitation. It was also possible to exchange $CsPbBr_3$ to $CsPbI_3$ under two photon excitation that selectively excited the nanocrystal instead of the light sensitive diiodomethane. The anion exchange occurred through the interaction of the nanocube with the solvent which resulted in a large local halide content facilitating the exchange. The fine control of the anion exchange could be controlled by the light exposure, laser power and excitation wavelength. This provides a method to easily select a desired wavelength when performing anion exchange. The self-anion exchange was also discovered by placing the nanocrystal in its respective halogenated solvent and illuminating it resulting in an increase of an order of magnitude in PLQY for $CsPbCl_3$ and an increase of 10% in $CsPbBr_3$.

7.4 Long Range Hot Electron Transfer from Mn-doped II-VI QDs to a Metal Catalyst for CO_2 Reduction

Hot electrons generated from Mn-doped II-VI QDs have already shown they have great capabilities from transferring through thick 7 nm barriers or being photoemitted in vacuum while being generated from *cw* visible light. This shows that the range of hot electron transfer can extend beyond the QD surface and the amount of energy available is above vacuum energy levels giving it enough energy to reduce chemically inert species. In typical photocatalytic systems where CO_2 is being reduced to CO, the photosensitizer must be linked to the catalyst to have efficient electron transfer. This results in complicated chemistries where the photosensitizers must be tailored to the catalyst with a specific linker. We were able to create a hybrid QD/metal catalyst system that was able to utilize the long-range transfer capability of the hot electrons to effectively generate CO from CO_2.

In our system we compared Mn doped and undoped QD with and without a $[Ni(cyclam)]^{2+}$ metal catalyst in an aqueous solution bubbled with CO_2. We observed that the Mn doped QD on its own was able to generate CO, which typically requires a catalyst, and performed at a similar efficiency to the undoped/catalyst system. The Mn doped QD/catalyst system had an increase of 6 times for CO generation while also having an increase in selectivity towards CO increase from 7% to 50%. When the solution was bubbled with Ar the catalyst was also able to increase the H_2 production by 5 times. This shows the versatility of the system and how it can be used as a catalyst for a range of different chemical species without having to make drastic changes to the reaction setup.

7.5 Future Works and Outlook

We were able to create the synthetic foundation for Mn-doping in $CsPbCl_3$ and $CsPbBr_3$ providing a new material for the study of hot electron generation. Quantum confined $CsPbBr_3$ perovskite has shown many interesting optical properties from light induced forbidden transition to large splitting of the bright and dark excitonic state. The dark exciton has μs decay lifetimes which could result in a greater chance of hot electron generation since bright exciton relaxation is on the order of 10s of ns. This can be studied by performing photoemission measurements of the Mn-doped $CsPbBr_3$ nanoplatelets at low temperature and seeing if the hot electron photocurrent increases under those conditions. While the inherent stability of the perovskite is still a major hurdle there have been several examples of photocatalytic reactions in organic phase with $CsPbBr_3$. Utilization of the Mn-doped $CsPbBr_3$ can possibly improve the photocatalytic ability of the perovskite as has been shown in II-VI QDs for H_2 and CO production.

The II-VI QDs remain the model system for testing proof of concept experiments for hot electron generation due to the well-developed system protocols in place. The reduction potential of the hot electron should theoretically have enough energy to directly reduce N_2 to N_2^- which provides it with the ability to reduce most chemical species. There are a multitude of photocatalytic reactions and metal catalyst combinations that can be mapped out to determine the effectiveness of the hot electron. Currently when the carbon source is switched from CO_2 to formic acid there is over two orders of magnitude in the total efficiency of the system for generating CO and H_2 without the presence of a hole scavenger making the system self-contained. This is a promising new result showing that there are a large amount of possibilities for utilizing hot electrons in a photocatalytic application.

The study and observation of the solvated electron in ammonia from II-VI QDs will also be an interesting experiment. Typically, solvated electrons are generated from either alkali metals or flash photolysis and is stabilized in a cavity of solvent molecules. The lifetime of the solvated electron depends on the solvent and can range from 0.5 ms in water to days in liquid ammonia. Since the hot electrons generated in II-VI QDs happen over the lifetime of the Mn emission (5 ms) it would difficult to accumulate a high enough concentration to measure their absorption in water. In ammonia they are stable for days and after long photoexcitation enough could be accumulated to measure the absorption of the solvated electron, which would be the first example of their generation from Mn-doped QDs. This result would be very interesting but has several difficult steps such as working at -30 °C, solubilizing the QD in ammonia and keeping them stable over long periods of photoexcitation.

REFERENCES

1. R. T. Ross and A. J. Nozik, *J. Appl. Phys.*, 1982, **53**, 3813-3818.

2. G. Allan and C. Delerue, *Phys. Rev. B*, 2009, **79**, 195324.

3. V. I. Klimov and D. W. McBranch, *Phys. Rev. Lett.*, 1998, **80**, 4028.

4. A. Pandey and P. Guyot-Sionnest, *Science* 2008, **322**, 929-932.

5. A. Furube, L. Du, K. Hara, R. Katoh and M. Tachiya, *J. Am. Chem. Soc.*, 2007, **129**, 14852-14853.

6. K. Wu, W. E. Rodríguez-Córdoba, Y. Yang and T. Lian, *Nano Lett.*, 2013, **13**, 5255-5263.

7. S. Mukherjee, F. Libisch, N. Large, O. Neumann, L. V. Brown, J. Cheng, J. B. Lassiter, E. A. Carter, P. Nordlander and N. J. Halas, *Nano Lett.*, 2013, **13**, 240-247.

8. A. J. Nozik, *Annu. Rev. Phys. Chem.*, 2001, **52**, 193-231.

9. V. I. Klimov, D. McBranch, C. Leatherdale and M. Bawendi, *Phys. Rev. B*, 1999, **60**, 13740.

10. W. A. Tisdale, K. J. Williams, B. A. Timp, D. J. Norris, E. S. Aydil and X.-Y. Zhu, *Science* 2010, **328**, 1543-1547.

11. H. Zhu, K. Miyata, Y. Fu, J. Wang, P. P. Joshi, D. Niesner, K. W. Williams, S. Jin and X.-Y. Zhu, *Science* 2016, **353**, 1409-1413.

12. M. L. Brongersma, N. J. Halas and P. Nordlander, *Nat. Nanotechnol.*, 2015, **10**, 25.

13. S. Mukherjee, L. Zhou, A. M. Goodman, N. Large, C. Ayala-Orozco, Y. Zhang, P. Nordlander and N. J. Halas, *J. Am. Chem. Soc.*, 2014, **136**, 64-67.

14. L. R. Hirsch, R. J. Stafford, J. A. Bankson, S. R. Sershen, B. Rivera, R. Price, J. D. Hazle, N. J. Halas and J. L. West, *Proc. Natl. Acad. Sci.*, 2003, **100**, 13549-13554.

15. L. Protesescu, S. Yakunin, M. I. Bodnarchuk, F. Krieg, R. Caputo, C. H. Hendon, R. X. Yang, A. Walsh and M. V. Kovalenko, *Nano Lett.*, 2015, **15**, 3692-3696.

16. B. A. Koscher, J. K. Swabeck, N. D. Bronstein and A. P. Alivisatos, *J. Am. Chem. Soc.*, 2017, **139**, 6566-6569.

17. G. Nedelcu, L. Protesescu, S. Yakunin, M. I. Bodnarchuk, M. J. Grotevent and M. V. Kovalenko, *Nano Lett.*, 2015, **15**, 5635-5640.

18. Q. A. Akkerman, V. D'Innocenzo, S. Accornero, A. Scarpellini, A. Petrozza, M. Prato and L. Manna, *J. Am. Chem. Soc.*, 2015, **137**, 10276-10281.

19. W. van der Stam, J. J. Geuchies, T. Altantzis, K. H. W. van den Bos, J. D. Meeldijk, S. Van Aert, S. Bals, D. Vanmaekelbergh and C. de Mello Donega, *J. Am. Chem. Soc.*, 2017, **139**, 4087-4097.

20. D. Zhang, S. W. Eaton, Y. Yu, L. Dou and P. Yang, *J. Am. Chem. Soc.*, 2015, **137**, 9230-9233.

21. Y. Dong, T. Qiao, D. Kim, D. Rossi, S. J. Ahn and D. H. Son, *Chem. Mater.*, 2019, **31**, 5655-5662.

22. Q. A. Akkerman, S. G. Motti, A. R. Srimath Kandada, E. Mosconi, V. D'Innocenzo, G. Bertoni, S. Marras, B. A. Kamino, L. Miranda, F. De Angelis, A. Petrozza, M. Prato and L. Manna, *J. Am. Chem. Soc.*, 2016, **138**, 1010-1016.

23. Y. Dong, T. Qiao, D. Kim, D. Parobek, D. Rossi and D. H. Son, *Nano Lett.*, 2018, DOI: 10.1021/acs.nanolett.8b00861.

24. A. K. Jena, A. Kulkarni and T. Miyasaka, *Chem. Rev.* , 2019, **119**, 3036-3103.
25. B. Saparov and D. B. Mitzi, *Chem. Rev.* , 2016, **116**, 4558-4596.

26. M. M. Lee, J. Teuscher, T. Miyasaka, T. N. Murakami and H. J. Snaith, *Science* 2012, **338**, 643-647.

27. N. J. Jeon, H. Na, E. H. Jung, T.-Y. Yang, Y. G. Lee, G. Kim, H.-W. Shin, S. I. Seok, J. Lee and J. Seo, *Nature Energy*, 2018, **3**, 682-689.

28. J. Kang and L.-W. Wang, *J. Phys. Chem. Lett.*, 2017, **8**, 489-493.

29. F. Liu, Y. Zhang, C. Ding, S. Kobayashi, T. Izuishi, N. Nakazawa, T. Toyoda, T. Ohta, S. Hayase, T. Minemoto, K. Yoshino, S. Dai and Q. Shen, *ACS Nano*, 2017, DOI: 10.1021/acsnano.7b05442.

30. A. Dutta, R. K. Behera, P. Pal, S. Baitalik and N. Pradhan, *Angew. Chem.*, 2019, **131**, 5608-5612.

31. B. A. Koscher, N. D. Bronstein, J. H. Olshansky, Y. Bekenstein and A. P. Alivisatos, *J. Am. Chem. Soc.*, 2016, **138**, 12065-12068.

32. Y. Zhang, D. Lu, M. Gao, M. Lai, J. Lin, T. Lei, Z. Lin, L. N. Quan and P. Yang, *Proc. Natl. Acad. Sci.*, 2019, **116**, 12648-12653.

33. Y. Bekenstein, B. A. Koscher, S. W. Eaton, P. Yang and A. P. Alivisatos, *J. Am. Chem. Soc.*, 2015, **137**, 16008-16011.

34. G. Almeida, L. Goldoni, Q. Akkerman, Z. Dang, A. H. Khan, S. Marras, I. Moreels and L. Manna, *ACS Nano*, 2018, **12**, 1704-1711.

35. A. Dutta, S. K. Dutta, S. Das Adhikari and N. Pradhan, *ACS Energy Lett.*, 2018, **3**, 329-334.

36. D. J. Norris, A. L. Efros and S. C. Erwin, *Science* 2008, **319**, 1776-1779.

37. D. Mocatta, G. Cohen, J. Schattner, O. Millo, E. Rabani and U. Banin, *Science* 2011, **332**, 77-81.

38. G. F. Wang, Q. Peng and Y. D. Li, *Acc. Chem. Res.*, 2011, **44**, 322-332.

39. D. J. Norris, N. Yao, F. T. Charnock and T. A. Kennedy, *Nano Lett.*, 2001, **1**, 3-7.

40. J. M. Luther, P. K. Jain, T. Ewers and A. P. Alivisatos, *Nat. Mater.*, 2011, **10**, 361-366.

41. R. N. Bhargava, D. Gallagher, X. Hong and A. Nurmikko, *Phys. Rev. Lett.*, 1994, **72**, 416-419.

42. K. Sooklal, B. S. Cullum, S. M. Angel and C. J. Murphy, *J. Phys. Chem.*, 1996, **100**, 4551-4555.

43. T. Ji, W.-B. Jian and J. Fang, *J. Am. Chem. Soc.*, 2003, **125**, 8448-8449.

44. F. V. Mikulec, M. Kuno, M. Bennati, D. A. Hall, R. G. Griffin and M. G. Bawendi, *J. Am. Chem. Soc.*, 2000, **122**, 2532-2540.

45. C. A. Stowell, R. J. Wiacek, A. E. Saunders and B. A. Korgel, *Nano Lett.*, 2003, **3**, 1441-1447.

46. Y. Yang, O. Chen, A. Angerhofer and Y. C. Cao, *J. Am. Chem. Soc.*, 2006, **128**, 12428-12429.

47. V. A. Vlaskin, C. J. Barrows, C. S. Erickson and D. R. Gamelin, *J. Am. Chem. Soc.*, 2013, **135**, 14380-14389.

48. H.-Y. Chen, S. Maiti and D. H. Son, *ACS Nano*, 2012, **6**, 583-591.

49. P. I. Archer, S. A. Santangelo and D. R. Gamelin, *Nano Lett.*, 2007, **7**, 1037-1043.

50. W. Liu, Q. Lin, H. Li, K. Wu, I. Robel, J. M. Pietryga and V. I. Klimov, *J. Am. Chem. Soc.*, 2016, **138**, 14954-14961.

51. D. Parobek, B. J. Roman, Y. Dong, H. Jin, E. Lee, M. Sheldon and D. H. Son, *Nano Lett.*, 2016, **16**, 7376-7380.

52. D. Parobek, Y. Dong, T. Qiao and D. H. Son, *Chem. Mater.*, 2018, **30**, 2939-2944.

53. R. Begum, M. R. Parida, A. L. Abdelhady, B. Murali, N. M. Alyami, G. H. Ahmed, M. N. Hedhili, O. M. Bakr and O. F. Mohammed, *J. Am. Chem. Soc.*, 2017, **139**, 731-737.

54. B. J. Roman, J. Otto, C. Galik, R. Downing and M. Sheldon, *Nano Lett.*, 2017, **17**, 5561-5566.

55. S. K. Balakrishnan and P. V. Kamat, *ACS Energy Lett.*, 2017, **2**, 88-93.

56. G. Pan, X. Bai, D. Yang, X. Chen, P. Jing, S. Qu, L. Zhang, D. Zhou, J. Zhu, W. Xu, B. Dong and H. Song, *Nano Lett.*, 2017, **17**, 8005-8011.

57. T. J. Milstein, D. M. Kroupa and D. R. Gamelin, *Nano Letters*, 2018, **18**, 3792-3799.

58. M. Liu, G. Zhong, Y. Yin, J. Miao, K. Li, C. Wang, X. Xu, C. Shen and H. Meng, *Adv. Sci.*, 2017.

59. A. Swarnkar, V. K. Ravi and A. Nag, *ACS Energy Lett.*, 2017, **2**, 1089-1098.

60. A. K. Guria, S. K. Dutta, S. D. Adhikari and N. Pradhan, *ACS Energy Lett.*, 2017, **2**, 1014-1021.

61. Y. Shen, M. Y. Gee, R. Tan, P. J. Pellechia and A. B. Greytak, *Chem. Mater.*, 2013, **25**, 2838-2848.

62. H. Liu, Z. Wu, J. Shao, D. Yao, H. Gao, Y. Liu, W. Yu, H. Zhang and B. Yang, *ACS Nano*, 2017, **11**, 2239-2247.

63. S. Das Adhikari, S. K. Dutta, A. Dutta, A. K. Guria and N. Pradhan, *Angew Chem Int Ed Engl*, 2017, **56**, 8746-8750.

64. C. C. Lin, K. Y. Xu, D. Wang and A. Meijerink, *Sci Rep*, 2017, **7**, 45906.

65. K. Xu, C. C. Lin, X. Xie and A. Meijerink, *Chem. Mater.*, 2017, **29**, 4265-4272.

66. W. J. Mir, M. Jagadeeswararao, S. Das and A. Nag, *ACS Energy Lett.*, 2017, **2**, 537-543.

67. S. Das Adhikari, A. Dutta, S. K. Dutta and N. Pradhan, *ACS Energy Lett.*, 2018, **3**, 1247-1253.

68. F. Li, Z. Xia, C. Pan, Y. Gong, L. Gu, Q. Liu and J. Z. Zhang, *ACS Appl. Mater. Interfaces*, 2018, **10**, 11739-11746.

69. Z. Zhang, L. Ren, H. Yan, S. Guo, S. Wang, M. Wang and K. Jin, *J. Phys. Chem. C*, 2017, **121**, 17436-17441.

70. S. Zou, Y. Liu, J. Li, C. Liu, R. Feng, F. Jiang, Y. Li, J. Song, H. Zeng, M. Hong and X. Chen, *J. Am. Chem. Soc.*, 2017, **139**, 11443-11450.

71. K. Xu and A. Meijerink, *Chem. Mater.*, 2018, DOI: 10.1021/acs.chemmater.8b02157.

72. R. Beaulac, P. I. Archer, J. van Rijssel, A. Meijerink and D. R. Gamelin, *Nano Lett.*, 2008, **8**, 2949-2953.

73. M. C. De Siena, D. E. Sommer, S. E. Creutz, S. T. Dunham and D. R. Gamelin, *Chem. Mater.*, 2019, **31**, 7711-7722.

74. D. Rossi, D. Parobek, Y. Dong and D. H. Son, *J. Phys. Chem. C*, 2017.

75. X. Yuan, S. Ji, M. C. De Siena, L. Fei, Z. Zhao, Y. Wang, H. Li, J. Zhao and D. R. Gamelin, *Chem. Mater.*, 2017, **29**, 8003-8011.

76. C. Zhou, Y. Tian, O. Khabou, M. Worku, Y. Zhou, J. Hurley, H. Lin and B. Ma, *ACS Appl. Mater. Interfaces*, 2017, **9**, 40446-40451.

77. Q. Wang, X. Zhang, Z. Jin, J. Zhang, Z. Gao, Y. Li and S. F. Liu, *ACS Energy Lett.*, 2017, **2**, 1479-1486.

78. F. Wang, M. Yang, S. Ji, L. Yang, J. Zhao, H. Liu, Y. Sui, Y. Sun, J. Yang and X. Zhang, *J. Power Sources*, 2018, **395**, 85-91.

79. S. Ye, J. Y. Sun, Y. H. Han, Y. Y. Zhou and Q. Y. Zhang, *ACS Appl. Mater. Interfaces*, 2018, **10**, 24656-24664.

80. M. He, Y. Cheng, L. Shen, C. Shen, H. Zhang, W. Xiang and X. Liang, *Appl. Surf. Sci.*, 2018, **448**, 400-406.

81. F. Meinardi, Q. A. Akkerman, F. Bruni, S. Park, M. Mauri, Z. Dang, L. Manna and S. Brovelli, *ACS Energy Lett.*, 2017, **2**, 2368-2377.

82. F. Lin, F. Li, Z. Lai, Z. Cai, Y. Wang, O. S. Wolfbeis and X. Chen, *ACS Appl. Mater. Interfaces*, 2018, **10**, 23335-23343.

83. N. Pradhan and X. Peng, *J. Am. Chem. Soc.*, 2007, **129**, 3339-3347.
84. C. Ronda and T. Amrein, *J. Lumin.*, 1996, **69**, 245-248.

85. S. Ithurria, P. Guyot-Sionnest, B. Mahler and B. Dubertret, *Phys. Rev. Lett.*, 2007, **99**, 265501.

86. J. Suyver, S. Wuister, J. Kelly and A. Meijerink, *Phys. Chem. Chem. Phys.*, 2000, **2**, 5445-5448.

87. H. Y. Chen and D. H. Son, *Isr. J. Chem.*, 2012, **52**, 1016-1026.

88. E. M. Olano, C. D. Grant, T. J. Norman, E. W. Castner and J. Z. Zhang, *J. Nanosci. Nanotechnol.*, 2005, **5**, 1492-1497.

89. T. Qiao, D. Parobek and D. H. Son, *J. Mater. Chem. C*, 2019, **7**, 14788-14797.

90. S. Jana, G. Manna, B. B. Srivastava and N. Pradhan, *Small*, 2013, **9**, 3753-3758.

91. H. Xin, J. K. Katahara, I. L. Braly and H. W. Hillhouse, *Adv. Energ. Mater.*, 2014, **4**, 1301823.

92. A. A. Bol, J. Ferwerda, J. A. Bergwerff and A. Meijerink, *J. Lumin.*, 2002, **99**, 325-334.

93. K. E. Knowles, K. H. Hartstein, T. B. Kilburn, A. Marchioro, H. D. Nelson, P. J. Whitham and D. R. Gamelin, *Chem. Rev.* , 2016, **116**, 10820-10851.

94. B. B. Srivastava, S. Jana and N. Pradhan, *J. Am. Chem. Soc.*, 2010, **133**, 1007-1015.

95. C. Corrado, Y. Jiang, F. Oba, M. Kozina, F. Bridges and J. Z. Zhang, *J. Phys. Chem. A*, 2009, **113**, 3830-3839.

96. R. W. Meulenberg, T. van Buuren, K. M. Hanif, T. M. Willey, G. F. Strouse and L. J. Terminello, *Nano Lett.*, 2004, **4**, 2277-2285.

97. K. E. Knowles, H. D. Nelson, T. B. Kilburn and D. R. Gamelin, *J. Am. Chem. Soc.*, 2015, **137**, 13138-13147.

98. J. Suyver, T. Van der Beek, S. Wuister, J. Kelly and A. Meijerink, *Appl. Phys. Lett.*, 2001, **79**, 4222-4224.

99. G. K. Grandhi, R. Tomar and R. Viswanatha, *ACS Nano*, 2012, **6**, 9751-9763.

100. G. K. Grandhi and R. Viswanatha, *J. Phys. Chem. Lett.*, 2013, **4**, 409-415.

101. K. E. Hughes, K. H. Hartstein and D. R. Gamelin, *ACS Nano*, 2018, **12**, 718-728.

102. P. J. Whitham, K. E. Knowles, P. J. Reid and D. R. Gamelin, *Nano Lett.*, 2015, **15**, 4045-4051.

103. S. Gul, J. K. Cooper, C. Corrado, B. Vollbrecht, F. Bridges, J. Guo and J. Z. Zhang, *J. Phys. Chem. C*, 2011, **115**, 20864-20875.

104. S. Gul, J. K. Cooper, P.-A. Glans, J. Guo, V. K. Yachandra, J. Yano and J. Z. Zhang, *ACS Nano*, 2013, **7**, 8680-8692.

105. B. Car, S. Medling, C. Corrado, F. Bridges and J. Z. Zhang, *Nanoscale*, 2011, **3**, 4182-4189.

106. A. M. Jawaid, S. Chattopadhyay, D. J. Wink, L. E. Page and P. T. Snee, *ACS Nano*, 2013, **7**, 3190-3197.

107. H. D. Nelson, X. Li and D. R. Gamelin, *J. Phys. Chem. C*, 2016, **120**, 5714-5723.

108. R. Viswanatha, S. Brovelli, A. Pandey, S. A. Crooker and V. I. Klimov, *Nano Lett.*, 2011, **11**, 4753-4758.

109. D. L. Dexter, *J. Chem. Phys.*, 1953, **21**, 836-850.

110. Y. Dong, D. Rossi, D. Parobek and D. H. Son, *ChemPhysChem*, 2016, **17**, 660-664.

111. C. J. Barrows, J. D. Rinehart, H. Nagaoka, D. W. deQuilettes, M. Salvador, J. I. Chen, D. S. Ginger and D. R. Gamelin, *J. Phys. Chem. Lett.*, 2016, **8**, 126-130.

112. Y. Dong, D. Parobek, D. Rossi and D. H. Son, *Nano Lett.*, 2016, **16**, 7270-7275.

113. S. Lingampalli, M. M. Ayyub and C. Rao, *ACS Omega*, 2017, **2**, 2740-2748.

114. T. Inoue, A. Fujishima, S. Konishi and K. Honda, *Nature* 1979, **277**, 637-638.

115. J. Willkomm, K. L. Orchard, A. Reynal, E. Pastor, J. R. Durrant and E. Reisner, *Chem. Soc. Rev.*, 2016, **45**, 9-23.

116. H. Lu, Z. Huang, M. S. Martinez, J. C. Johnson, J. M. Luther and M. C. Beard, *Energy & Environmental Science*, 2020, DOI: 10.1039/C9EE03930A.

117. T. Mokari, E. Rothenberg, I. Popov, R. Costi and U. Banin, *Science* 2004, **304**, 1787-1790.

118. L. Amirav and A. P. Alivisatos, *J. Phys. Chem. Lett.*, 2010, **1**, 1051-1054.

119. Z. Han, F. Qiu, R. Eisenberg, P. L. Holland and T. D. Krauss, *Science* 2012, **338**, 1321-1324.

120. K. E. Dalle, J. Warnan, J. J. Leung, B. Reuillard, I. S. Karmel and E. Reisner, *Chem Rev*, 2019, **119**, 2752-2875.

121. J. D. Froehlich and C. P. Kubiak, *J. Am. Chem. Soc.*, 2015, **137**, 3565-3573.

122. S. Lian, M. S. Kodaimati, D. S. Dolzhnikov, R. Calzada and E. A. Weiss, *J. Am. Chem. Soc.*, 2017, **139**, 8931-8938.

123. S. Lian, M. S. Kodaimati and E. A. Weiss, *ACS Nano*, 2018, **12**, 568-575.

124. M. F. Kuehnel, K. L. Orchard, K. E. Dalle and E. Reisner, *J. Am. Chem. Soc.*, 2017, **139**, 7217-7223.

125. M. F. Kuehnel, C. D. Sahm, G. Neri, J. R. Lee, K. L. Orchard, A. J. Cowan and E. Reisner, *Chem Sci*, 2018, **9**, 2501-2509.

126. D. Zhu, L. Zhang, R. E. Ruther and R. J. Hamers, *Nat. Mater.*, 2013, **12**, 836-841.

127. J. R. Christianson, D. Zhu, R. J. Hamers and J. R. Schmidt, *J. Phys. Chem. B*, 2014, **118**, 195-203.

128. L. Zhang, D. Zhu, G. M. Nathanson and R. J. Hamers, *Angew. Chem. Int. Ed.*, 2014, **53**, 9746-9750.

129. S. Sun, D. Yuan, Y. Xu, A. Wang and Z. Deng, *ACS Nano*, 2016, **10**, 3648-3657.

130. N. Pradhan, D. Goorskey, J. Thessing and X. Peng, *J. Am. Chem. Soc.*, 2005, **127**, 17586-17587.

131. R. Beaulac, L. Schneider, P. I. Archer, G. Bacher and D. R. Gamelin, *Science* 2009, **325**, 973-976.

132. T. L. Doane, K. L. Ryan, L. Pathade, K. J. Cruz, H. Zang, M. Cotlet and M. M. Maye, *ACS Nano*, 2016, **10**, 5864-5872.

133. R. Beaulac, P. I. Archer, S. T. Ochsenbein and D. R. Gamelin, *Adv. Funct. Mater.*, 2008, **18**, 3873-3891.

134. S. C. Erwin, L. Zu, M. I. Haftel, A. L. Efros, T. A. Kennedy and D. J. Norris, *Nature* 2005, **436**, 91-94.

135. B. B. Srivastava, S. Jana, N. S. Karan, S. Paria, N. R. Jana, D. Sarma and N. Pradhan, *J. Phys. Chem. Lett.*, 2010, **1**, 1454-1458.

136. U. Kambli and H. Gudel, *J. Phys. C: Solid State Phys.*, 1984, **17**, 4041.

137. V. I. Klimov, *Semiconductor and Metal Nanocrystals: Synthesis and Electronic and Optical Properties*, CRC Press, 2003.

138. A. C. Larson and R. B. V. Dreele, *General Structure Analysis System (GSAS)*, Los Alamos National Laboratory Report LAUR, 2000.

139. P. Cottingham and R. L. Brutchey, *Chem. Commun.* , 2016, **52**, 5246-5249.

140. J. A. Cape, *J. Appl. Phys.*, 1969, **40**, 5001.

141. G. L. McPherson, K. Talluto and R. A. Auerbach, *Solid State Commun.*, 1982, **43**, 817-819.

142. A. Vink, M. De Bruin, S. Roke, P. Peijzel and A. Meijerink, *J. Electrochem. Soc.*, 2001, **148**, E313-E320.

143. H.-Y. Chen, T.-Y. Chen and D. H. Son, *J. Phys. Chem. C*, 2010, **114**, 4418-4423.

144. R. E. Beal, D. J. Slotcavage, T. Leijtens, A. R. Bowring, R. A. Belisle, W. H. Nguyen, G. F. Burkhard, E. T. Hoke and M. D. McGehee, *J. Phys. Chem. Lett.*, 2016, **7**, 746-751.

145. J. Song, J. Li, X. Li, L. Xu, Y. Dong and H. Zeng, *Adv. Mater. (Weinheim, Ger.)*, 2015, **27**, 7162-7167.

146. D. Parobek, Y. Dong, T. Qiao, D. Rossi and D. H. Son, *J. Am. Chem. Soc.*, 2017.

147. D. A. Bussian, S. A. Crooker, M. Yin, M. Brynda, A. L. Efros and V. I. Klimov, *Nat. Mater.*, 2009, **8**, 35-40.

148. W. Liu, Q. Lin, H. Li, K. Wu, I. Robel, J. M. Pietryga and V. I. Klimov, *J. Am. Chem. Soc*, 2016, **138**, 14954-14961.

149. J. Zhu, X. Yang, Y. Zhu, Y. Wang, J. Cai, J. Shen, L. Sun and C. Li, *J. Phys. Chem. Lett.*, 2017.

150. P. Arunkumar, K. H. Gil, S. Won, S. Unithrattil, Y. H. Kim, H. J. Kim and W. B. Im, *J. Phys. Chem. Lett.*, 2017, **8**, 4161-4166.

151. F. Li, Z. Xia, Y. Gong, L. Gu and Q. Liu, *J. Mater. Chem. C*, 2017.

152. N. Pradhan, S. Das Adhikari, S. K. Dutta, A. Dutta and A. K. Guria, *Angew. Chem. Int. Ed.*, 2017.

153. M. C. Weidman, M. Seitz, S. D. Stranks and W. A. Tisdale, *ACS Nano*, 2016, **10**, 7830-7839.

154. J. Borges, J. A. Ribeiro, E. M. Pereira, C. A. Carreira, C. M. Pereira and F. Silva, *J. Colloid Interface Sci.*, 2011, **358**, 626-634.

155. X. Yuan, S. Ji, M. C. De Siena, L. Fei, Z. Zhao, Y. Wang, H. Li, J. Zhao and D. R. Gamelin, *Chem. Mater.*, 2017.

156. J. Suyver, S. Wuister, J. Kelly and A. Meijerink, *PCCP*, 2000, **2**, 5445-5448.

157. D. Zhang, Y. Yang, Y. Bekenstein, Y. Yu, N. A. Gibson, A. B. Wong, S. W. Eaton, N. Kornienko, Q. Kong and M. Lai, *J. Am. Chem. Soc.*, 2016, **138**, 7236-7239.

158. C. Eames, J. M. Frost, P. R. Barnes, B. C. O'regan, A. Walsh and M. S. Islam, *Nat. Commun.*, 2015, **6**.

159. J. M. Azpiroz, E. Mosconi, J. Bisquert and F. De Angelis, *Energy Environ. Sci.*, 2015, **8**, 2118-2127.

160. E. T. Hoke, D. J. Slotcavage, E. R. Dohner, A. R. Bowring, H. I. Karunadasa and M. D. McGehee, *Chem. Sci.*, 2015, **6**, 613-617.

161. S. J. Yoon, S. Draguta, J. S. Manser, O. Sharia, W. F. Schneider, M. Kuno and P. V. Kamat, *ACS Energy Lett.*, 2016, **1**, 290-296.

162. F. Palazon, Q. A. Akkerman, M. Prato and L. Manna, *ACS Nano*, 2015, **10**, 1224-1230.

163. C. P. Andrieux, I. Gallardo and J. M. Saveant, *J. Am. Chem. Soc.*, 1989, **111**, 1620-1626.

164. J. M. Saveant, *J. Am. Chem. Soc.*, 1992, **114**, 10595-10602.

165. A. A. Isse, C. Y. Lin, M. L. Coote and A. Gennaro, *J. Phys. Chem. B*, 2010, **115**, 678-684.

166. V. K. Ravi, G. B. Markad and A. Nag, *ACS Energy Lett.*, 2016, **1**, 665-671.

167. J. Endres, D. A. Egger, M. Kulbak, R. A. Kerner, L. Zhao, S. H. Silver, G. Hodes, B. P. Rand, D. Cahen and L. Kronik, *J. Phys. Chem. Lett.*, 2016, **7**, 2722-2729.

168. H. Rao, C.-H. Lim, J. Bonin, G. M. Miyake and M. Robert, *J. Am. Chem. Soc.*, 2018, **140**, 17830-17834.

169. X. Zhang, M. Cibian, A. Call, K. Yamauchi and K. Sakai, *ACS Catalysis*, 2019, **9**, 11263-11273.

170. W.-H. Zhang, S. W. Chien and T. A. Hor, *Coord. Chem. Rev.*, 2011, **255**, 1991-2024.

171. Z. Chai, Q. Li and D. Xu, *RSC Adv.*, 2014, **4**, 44991-44995.

172. G. Neri, M. Forster, J. J. Walsh, C. Robertson, T. Whittles, P. Farràs and A. J. Cowan, *Chem. Commun.* , 2016, **52**, 14200-14203.

173. N. Ikuta, S.-y. Takizawa and S. Murata, *Photochem. Photobiol. Sci.*, 2014, **13**, 691-702.

174. P. L. Cheung, S. C. Kapper, T. Zeng, M. E. Thompson and C. P. Kubiak, *J. Am. Chem. Soc.*, 2019, **141**, 14961-14965.

175. H.-Y. Chen, T.-Y. Chen, E. Berdugo, Y. Park, K. Lovering and D. H. Son, *J. Phys. Chem. C*, 2011, **115**, 11407-11412.

176. M. A. White, A. L. Weaver, R. Beaulac and D. R. Gamelin, *ACS Nano*, 2011, **5**, 4158-4168.

177. D. Parobek, T. Qiao and D. H. Son, 2019, **151**, 120901.

178. J.-P. Collin, A. Jouaiti and J.-P. Sauvage, *Inorg. Chem.*, 1988, **27**, 1986-1990.

179. C.-H. Hsia, A. Wuttig and H. Yang, *ACS Nano*, 2011, **5**, 9511-9522.

180. Y. Yang, O. Chen, A. Angerhofer and Y. C. Cao, *J. Am. Chem. Soc.*, 2008, **130**, 15649-15661.

181. C.-H. Hsia, A. Wuttig and H. Yang, *ACS Nano*, 2011, **5**, 9511-9522.

182. J. D. Froehlich and C. P. Kubiak, *Inorg. Chem.*, 2012, **51**, 3932-3934.

183. J. P. Collin, A. Jouaiti and J. P. Sauvage, *Inorg. Chem.*, 1988, **27**, 1986-1990.

184. C. A. Craig, L. O. Spreer, J. W. Otvos and M. Calvin, *J. Phys. Chem.*, 1990, **94**, 7957-7960.

185. L. Zhang, D. Zhu, G. M. Nathanson and R. J. Hamers, *Angew Chem Int Ed Engl*, 2014, **53**, 9746-9750.